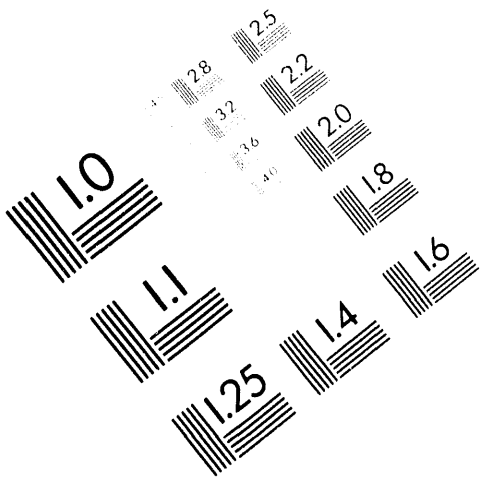

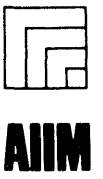

AIIM

Association for Information and Image Management

1100 Wayne Avenue, Suite 1100
Silver Spring, Maryland 20910

301-587-8202

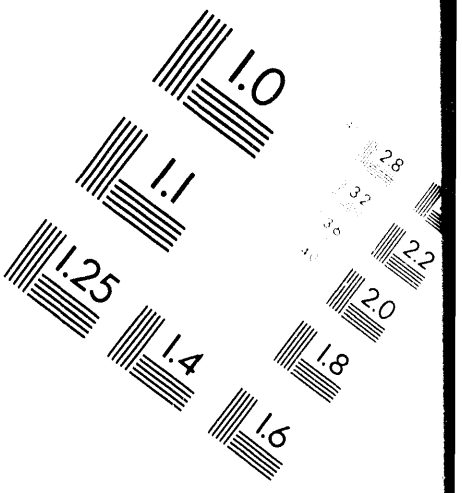

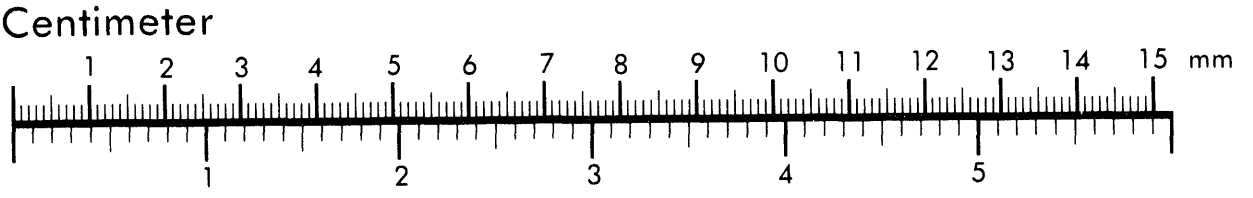

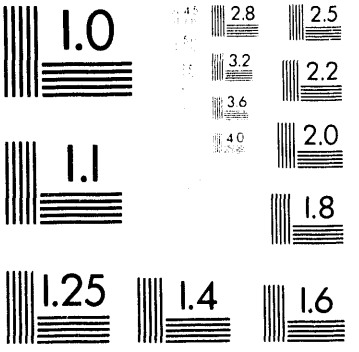

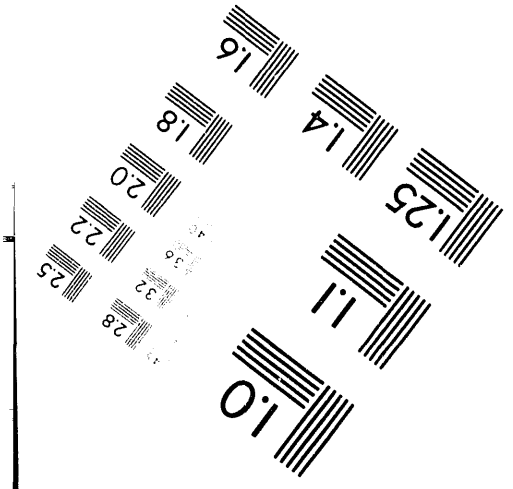

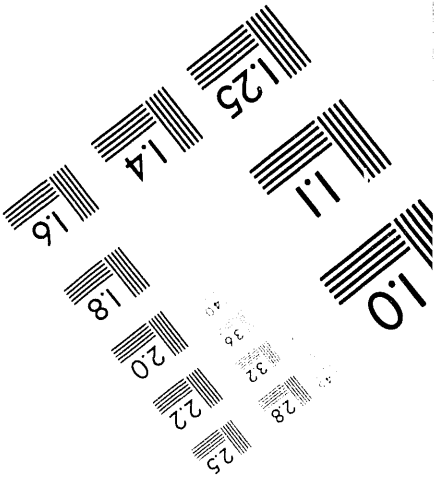

MANUFACTURED TO AIIM STANDARDS
BY APPLIED IMAGE, INC.

1 of 1

UNIVERSITY OF ROCHESTER
LABORATORY FOR LASER ENERGETICS

Volume 58
January–March 1994
DOE/SF/19460-17

LLE Review

Quarterly Report

UR LLE

Contents

In Brief iii

Target Imaging and Backlighting Diagnosis 57

Effect of Electron Collisions on Ion-Acoustic Waves and Heat Flow 68

Particle-in-Cell Code Simulations of the Interaction of Gaussian Ultrashort Laser Pulses with Targets of Varying Initial Scale Lengths 76

Characterization of Thick Cryogenic Fuel Layers: Compensation for the Lens Effect Using Convergent Beam Interferometry 83

Compact, Multijoule-Output, Nd:Glass, Large-Aperture Ring Amplifier 90

Publications and Conference Presentations

Target Imaging and Backlighting Diagnosis

The case of an x-ray backlighting image of a CH-shell target imploded by the OMEGA Upgrade laser system has been calculated and analyzed. The goal is to obtain information on the conditions at peak compression, where the experimental constraints due to target self-emission and required spatial resolution are maximal. Particular attention is devoted to the problem of discriminating against the target self-emission. It is shown that this can be done by obtaining a monochromatic image at a single spectral line emitted by the backlighter. Additionally, the target self-emission image has useful signatures, which can be studied with or without a backlighter. Two experimental configurations for monochromatic imaging are discussed: (a) an x-ray microscope with a flat crystal monochromator, and (b) pinhole imaging in conjunction with a curved crystal monochromator. Useful images are obtained with simple (undoped) CH-shell targets and without the need for a short-pulse backlighter beam.

The method of x-ray backlighting offers some advantages over methods employing target emission for the study of compression and stability of laser-imploded targets. One advantage of backlighting over emission imaging is the potential to delineate the interface between the pusher and the fuel. This capability is more easily realized if the compressed fuel is relatively cold near the interface (i.e., a temperature gradient exists in the fuel). Such information can, in principle, provide a direct measure of compression and evidence of any shell distortion. Emission methods can only delineate the hot core, which may consist of the fuel as well as an indeterminate section of the pusher. An additional advantage is the ability to choose a short-enough backlighting wavelength (say, $\lambda < 3$ Å) to avoid too high an opacity; with emission, the interface region is often not hot enough to emit such short wavelengths.

An important ingredient in the backlighting schemes, as discussed below, is two-dimensional monochromatic imaging; this added feature can be likewise applied to, and enhance, methods based on target emission. Monochromatic imaging can be used to probe a particular layer in the target, which is doped with a suitable material. The imaging then involves a particular atomic transition of that material that gives rise to either monochromatic emission or absorption. However, in the case of backlighting, monochromatic imaging must be used even in the absence of a doped layer to overcome the background due to target emission.

When performing backlighting imaging, the self-emission of the imaged target is normally considered a hindrance and its suppression is considered desirable. In the test case studied here the backlighting and self-emission images happen to be of comparable intensity. This is an advantageous situation because the two image components provide complementary information on the compression and implosion uniformity.

Most backlighting experiments in the past were less challenging. Typically, they used softer backlighter radiation ($\lambda > 8$ Å) than we envisage using here. Softer radiation is heavily absorbed by the shell so it can only delineate the outer surface of the shell. This kind of measurement cannot yield reliable information on the compression or stability. Softer radiation is easier to produce in copious amounts, and the requirements on spatial resolution in imaging the outer surface of the shell are more moderate. Additionally, the problem of target self-emission in those earlier experiments was much less severe because the self-emission of a low-Z polymer target is mostly very weak, except for the emission from a highly compressed core, such as predicted for OMEGA Upgrade targets.

Case Study of Experimental Parameters

We discuss the feasibility of backlighting experiments, using the *LILAC* code for simulating a candidate OMEGA Upgrade target. The target is a polymer shell of 940-μm diam and 30-μm thickness, filled with 80 atm DT gas, and imploded by a trapezoidal pulse. The pulse rises linearly over a 0.1-ns period to 13.5 TW, then remains constant for 2.2 ns, before dropping linearly over a 0.1-ns period. *LILAC* results were used for simulating the expected backlight image for this test shot. Figure 58.1 shows the density and electron-temperature

profiles predicted for this target at peak compression. The shell material has been compressed to a mean radius of ~50 μm and thickness of ~30 μm, with a density in the range of ~10–50 g/cm^3, corresponding to a $\rho\Delta r$ value of ~90 mg/cm^2. The electron temperature in the shell ranges from ~80 to ~1000 eV. Most of the backlight radiation absorption will occur within the colder, outer part of this compressed shell.

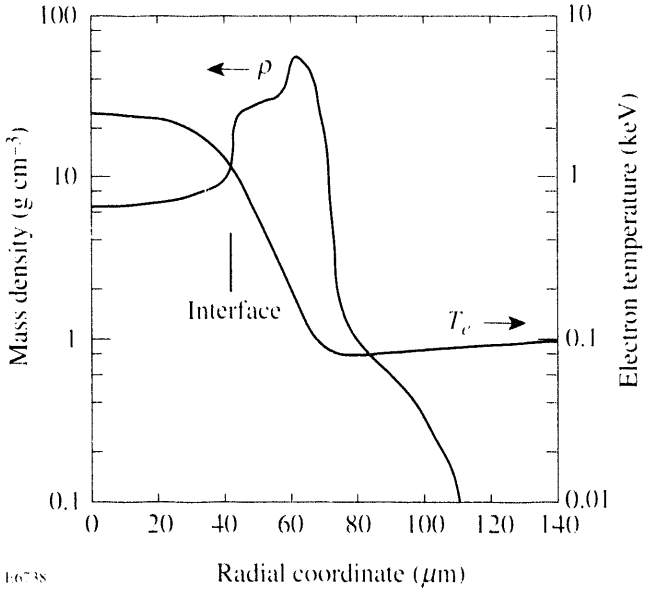

Figure 58.I
The density and electron-temperature profiles predicted by the *LILAC* code at peak compression for the case studied in this article.

Absorption Modeling

A simplified post-processor code was developed to calculate the transport of backlight radiation through the polymer target. The absorption at a wavelength λ in the CH material consists of two contributions: free-free (bremsstrahlung) and bound-free (photoionization); other absorption mechanisms (such as Compton scattering) are negligible for radiation of a few-keV photon energy. The free-free absorption coefficient at a frequency ν (in cm^{-1}) is given by

$$k_{ff} = \left(4\pi z^2 e^6 g_{ff} / 3^{3/2} hcm^2 \nu^3\right)\left(2m/\pi\kappa T\right)^{1/2} N_e N_i \,, \quad (1)$$

where g_{ff} is the free-free Gaunt factor (quantum correction). For a multispecies target, $z^2 N_e N_i$ is replaced by $N_e^2\langle z^2\rangle/\langle z\rangle$ in terms of species averages. The bound-free absorption coefficient for K-shell electrons (in cm^{-1}) in hydrogen-like ions is given by

$$k_{bf} = \left(64\pi^4 z^4 me^{10} g_{bf} / 3^{3/2} h^6 cn^5 \nu^3\right)\left(2m/\pi\kappa T\right)^{1/2} N_i \,, \quad (2)$$

where g_{bf} is the bound-free Gaunt factor, n is the principal quantum number of the absorbing level, and k_{bf} has to be calculated separately for each ionic species. For helium-like and higher ionic species, z^4 is replaced by $(z-\sigma)^4$, where σ is the Slater screening constant that equals[1] 0.3 for K-shell electrons. Neglecting the contribution to the opacity from L-shell and higher-shell electrons, the total opacity along various rays traversing the target can be now calculated, using the *LILAC*-predicted profiles of electron density and temperature through the target. To know the various N_i that go into the calculation of k_{bf} as well as into the z averages, we need first to calculate the distribution among the charge states (degrees of ionization). To calculate the charge-state distribution of carbon ions we make use of the LTE (local thermodynamic equilibrium) model. The LTE model becomes more valid as the plasma density increases and the temperature and the atomic charge Z decrease. These conditions indeed prevail within the cold, compressed part of the shell, made of low-Z polymer material. To verify the applicability of LTE we use the condition[2] given by Griem:

$$N_e > 7\times 10^{18}\left(z^7/n^{17/2}\right)\left(\kappa T/z^2 E_H\right)^{1/2} \text{cm}^{-3}, \quad (3)$$

where E_H is the ionization energy of hydrogen (13.59 eV) and n is the lowest principal quantum number for which the level population is still in LTE with the continuum (i.e., whose population is related to that of free electrons by the Saha equation). For a typical temperature of 150 eV within the compressed shell, which is the principal absorber of backlighting radiation, and with $Z = 6$ and $n = 1$, Eq. (3) becomes $N_e > 3.2 \times 10^{24}$ cm^{-3}. This is well below the predicted values of $N_e \geq 1 \times 10^{25}$ cm^{-3}.

We use the Saha equation to calculate the distribution of carbon ions in the C^{+4}, C^{+5}, and C^{+6} charge states, while ignoring lower ionizations (which are negligible even at the lowest existing temperature, ~80 eV). The charge-state densities are then given by the set of equations:

$$\left(N_e N^{+6}/N^{+5}\right) = \left[2Z^{+6}(T)/Z^{+5}(T)\right]\left(2\pi m\kappa T/h^2\right)^{3/2}$$

$$\exp\left[-\left(E^{+5} - \Delta E^{+5}\right)/\kappa T\right], \quad (4)$$

$$\left(N_e N^{+5}/N^{+4}\right) = \left[2Z^{+5}(T)/Z^{+4}(T)\right]\left(2\pi m\kappa T/h^2\right)^{3/2} \exp\left[-\left(E^{+4} - \Delta E^{+4}\right)/\kappa T\right], \quad (5)$$

$$N^{+4} + N^{+5} + N^{+6} = N_C, \quad (6)$$

where $Z(T)$ is the partition function, E^{+5} is the ionization energy of hydrogen-like carbon, E^{+4} that of helium-like carbon, and N_C is the total carbon ion density. The reduction in ionization energy ΔE is calculated by an approximation[3] to the theory of Stewart and Pyatt:[4]

$$\Delta E(eV) = 2.16\times10^{-7}\left(z/r_i\right)\left[\left(1+x^3\right)^{2/3} - x^2\right], \quad (7)$$

$x = r_D/r_i$, in terms of the Debye radius r_D and the interionic distance r_i:

$$r_D = \left[\kappa T/N_e\left(1+\langle z\rangle\right)\right]^{1/2}, \quad r_i = \left(3\langle z\rangle/4\pi N_e\right)^{1/3}. \quad (8)$$

It should be noted that to calculate the charge distribution, we need to know $\langle z\rangle$ in Eq. (8), which calls for an iterative solution. To simplify the calculation we adopt the *LILAC* value of $\langle z\rangle$ for Eq. (8), since the reduction in ionization energy is needed only as a correction in the calculation of the charge distribution. Using the resulting densities, we can readily calculate the z averages, as well as the total bound-free opacity

$$k_{bf} = N^{+4}k_{bf,4} + N^{+5}k_{bf,5}, \quad (9)$$

where $k_{bf,4}$ is the bound-free opacity due to the helium-like carbon ion, and $k_{bf,5}$ due to the hydrogen-like carbon ion.

For the simulation we choose a backlight wavelength of 2.62 A, corresponding to the $1s2p$–$1s^2$ line of Ti^{+20}. When irradiating a titanium backlighter target, this will be the strongest line, with a relatively low level of underlying continuum radiation.[5] We assume that the backlighter is irradiated by a single beam, identical to an OMEGA Upgrade beam with an energy of 500 J and the same pulse duration and shape as described above. We further assume a backlighter focal spot of 150-μm diam, giving rise to an irradiance of $\sim1.4\times10^{15}$ W/cm^2. This diameter is sufficiently large for imaging the core at peak compression at which time the outer shell diameter is only ~120 μm. The optimal choice of wavelength for a particular target implosion is one giving an opacity of ~1 in going through the target center at the desired time of probing. In this way the image will show the higher opacity going through the limb than through the center, thus delineating the outer as well as the inner surface of the cold pusher.

Monochromatic Absorption Images

In Fig. 58.2 we show examples of the predicted instantaneous backlighting images of the 2.62-A line at various times during target compression. The abscissa is the lateral coordinate in the image plane, assuming unit magnification. The backlighting incident intensity is assumed to be unity. Target self-emission was not included in this calculation. The images assume that a monochromator was used for the detection; methods of monochromatization are described below. We see that titanium was a suitable choice for this target implosion; indeed, the opacity through the target center at peak compression [Fig. 58.2(e)] is ~0.9. As a result, the absorption through the target center is visibly lower than that through the limb. [The opacity through the limb in Fig. 58.2(e) is ~2.3.] The position of the minimum in the curve (maximum absorption) corresponds approximately to the fuel-shell interface; however, it is slightly larger than the interface radius. Thus, the minimum of the 2.87-ns frame [Fig. 58.2(e)] is at a radius of ~58 μm, while the interface (Fig. 58.1) is at a radius of ~45 μm. For homogeneous shells, the dip in the backlight image would correspond to a line of sight that is tangent to the fuel-shell interface; this direction corresponds to the longest chord through the target, therefore to the highest opacity. The main reason for this difference is the fact that the inner part of the shell is hot and has lower absorption (additionally, the density at this time peaks outside the interface radius). This difference yields an underestimate by a factor of ~2 in the derived compressed density. In cases where the electron-temperature profile is more centrally peaked, the absorption-profile minimum will yield a value closer to the correct density.

To minimize the smearing effect due to time integration, a framing camera can be employed behind the imaging device. In this case, only one frame can be easily accommodated because the various frames in a framing camera are recorded at various spatial directions, whereas here only one direction will yield the desired image: that given by the line connecting the main and backlighter targets. Figure 58.2 indicates that during a period of ~100 ps around peak compression (from ~2.8 to ~2.9 ns) the backlight image changes very little. Therefore, the method used to obtain time resolution need not achieve better than ~50-ps resolution (for probing peak compression).

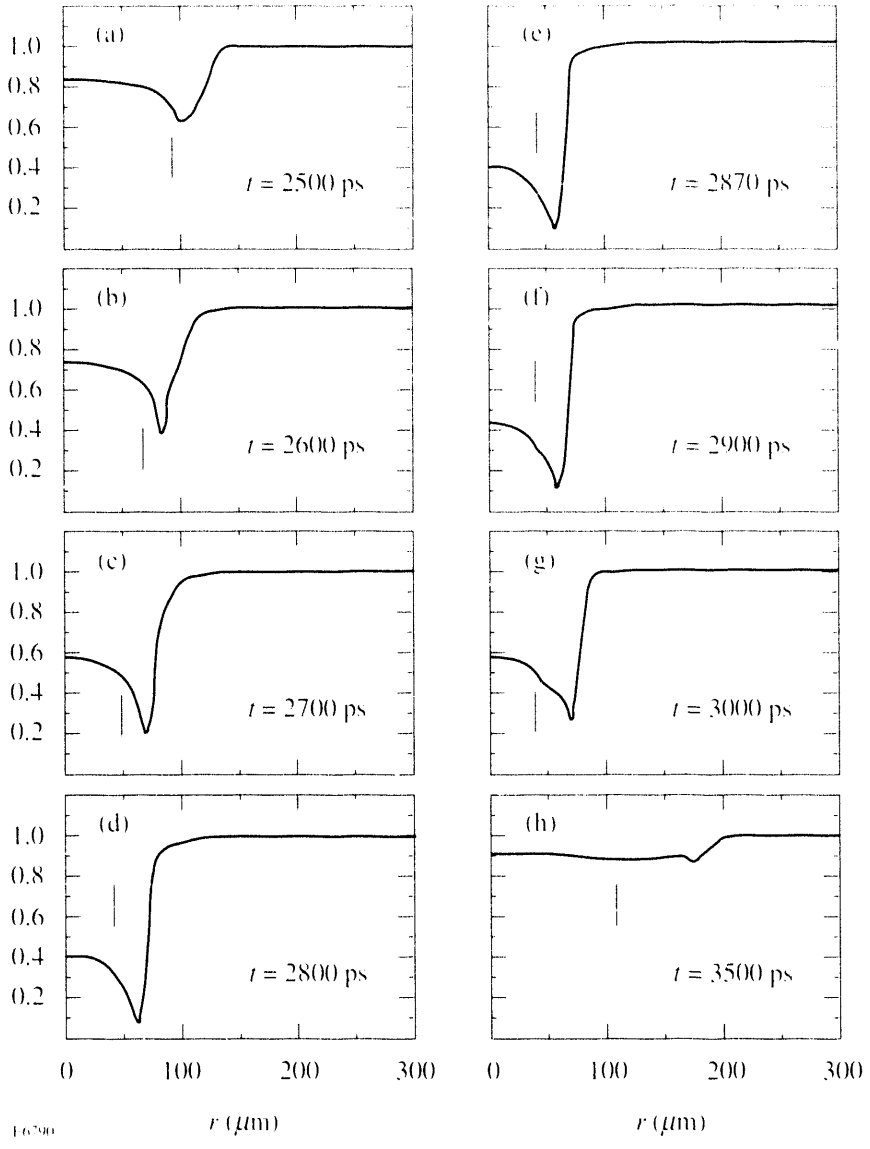

Figure 58.2
Examples of the predicted backlighting images at various times during the compression. The backlighting incident intensity was normalized to unity. Monochromatic backlighter was assumed at 2.62 Å (titanium). Target self-emission was not included. The vertical bars mark the fuel-shell interface.

Alternatively, the backlighter x-ray pulse can be shortened by using a polymer-coated Ti target, so that the Ti emission is delayed. To test this possibility we simulated the emission from a titanium target coated with varying thicknesses of polymer (CH) and irradiated with a single OMEGA Upgrade beam. The pulse shape was typical of those projected to be used in high-performance implosions: its total duration is 9 ns, it rises slowly first and then faster, until reaching a plateau of 0.3 TW from 8 to 9 ns, then dropping to zero. The total pulse energy is 0.5 kJ. This pulse shape is different than that described above, and used everywhere else in this work, and was chosen to verify x-ray pulse shortening even for this longer pulse. To simulate a backlighter disk of 150-μm diameter, irradiated at 1.4×10^{15} W/cm^2, we assumed in the simulations a spherical target of 300-μm radius, irradiated at that irradiance. We summarize the results in Fig. 58.3, showing the x-ray emission from an uncoated titanium target, as well as from a titanium target coated with an 18-μm-thick CH layer. The x-ray emission is integrated over the 4.5- to 5-keV energy band, comprising mostly the Ti^{+20} resonance line at 4.73 keV. Even with no CH coating, the x-ray pulse is considerably shorter than the incident laser pulse because the early ("foot") part of the laser pulse is too weak to yield significant x-ray radiation within this energy band. A coating of 18 μm CH further

shortens the x-ray pulse to a width of ~160 ps, while reducing the x-ray power by only a factor of ~2. Thicker coatings cause precipitous reduction in x-ray power and are thus not useful.

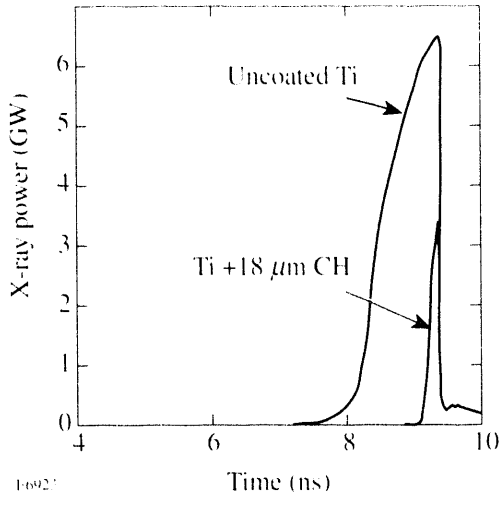

Figure 58.3
Simulated x-ray emission from an uncoated titanium target, as well as from a titanium target coated with an 18-μm-thick CH layer. The x-ray emission is integrated over the 4.5- to 5-keV energy band, comprising mostly the Ti^{+20} resonance line at 4.73 keV.

Emission Profiles

The backlighting images (such as in Fig. 58.2) should now be combined with the target self-emission profiles. We note that in LTE the local emission $\varepsilon(\nu)$ and the absorption coefficient $k(\nu)$ are related through Kirchhoff's law,[6] in terms of the blackbody function B_ν:

$$\varepsilon(\nu) = k(\nu) B_\nu = \left(2h\nu^3 / c^2\right) k(\nu) \Big/ \left[\exp(h\nu / \kappa T) - 1\right], \quad (10)$$

where κ is the Boltzmann's constant. Expressing Eq. (10) in explicit units,

$$\varepsilon\left(\frac{\text{keV}}{\text{keV ns cm}^3\,\Omega}\right) = 3.13\times 10^{22}\,\frac{k\left(\text{cm}^{-1}\right)\left[E(\text{keV})\right]^3}{\exp(E/T) - 1}, \quad (11)$$

where Ω designates solid angle. The total spectral intensity emerging along a line of sight (in the x direction) at a distance y from the axial direction, due to both the backlighter as well as the target self-emission, is obtained by solving the radiation transport equation

$$I(\nu_0, y) = I_{BL}(\nu_0)\exp\left[-\int_{x_1}^{x_2} k(\nu_0, r)\,dx\right] + \int_{x_1}^{x_2} \varepsilon(\nu_0, r)\exp\left[-\int_{x}^{x_2} k(\nu_0, r')\,dx'\right] dx, \quad (12)$$

where $x_1 = -\left(R^2 - y^2\right)^{1/2}$, $x_2 = -x_1$, $r = \left(x^2 + y^2\right)^{1/2}$, $r' = \left(x'^2 + y^2\right)^{1/2}$, R is the target radius, $I_{BL}(\nu_0)$ is the spectral intensity emitted by the backlighter at the line-center frequency ν_0 (i.e., at 2.62 Å), and the local emission $\varepsilon(\nu)$ is given by Eq. (11). The resulting one-dimensional profile $I(\nu_0, y)$ is in reality, of course, circularly symmetric. Since we chose $I_{BL}(\nu_0)$ to correspond to the peak of the backlighting line, the profile calculated by Eq. (12) gives the highest possible contrast between the backlighting and the self-emission images. It will be realized only if the monochromator bandwidth is not larger than the spectral width of the backlighter line. For a wider bandwidth we sample a larger fraction of the continuous self-emission, but the intensity from the backlighter (assumed to be mostly in a single spectral line) will remain about the same, thus lowering the contrast.

We next estimate the backlighting irradiance $I_{BL}(\nu_0)$ at the 2.62-Å wavelength, the $1s2p$-$1s^2$ transition of Ti^{+20}. The assumed laser irradiance on the backlighter is 1.4×10^{15} W/cm^2, or 9.4×10^{21} keV/(ns cm^2). At this irradiance, the x-ray yield for producing the Ti^{+20} line at 2.62 Å can be conservatively taken[5] to be 0.03% into unit solid angle perpendicular to the target, giving an x-ray flux of 2.8×10^{18} keV/(ns cm^2 Ω). To calculate the flux per unit photon energy, as explained above, this number has to be divided by the larger of the spectral line width and the instrumental width. The former is ~1.2 eV (see below), whereas a typical instrumental width would be ~4 eV. We finally obtain for the backlighting spectral flux at the frequency ν_0 of line center

$$I_{BL}(\nu_0) = 7.0 \times 10^{20}\,\frac{\text{keV}}{\text{keV}\left(\text{ns cm}^2\,\Omega\right)}. \quad (13)$$

Using this value and the plasma profiles calculated by the *LILAC* code (Fig. 58.1) we solve Eq. (12) numerically to obtain the combined image of backlighting and self-emission. The imaging device is assumed to have unit magnification and throughput.

We show in Fig. 58.4 the combined monochromatic image (at 2.62 Å) due to backlighting and self-emission at peak compression, intercepted by a monochromator crystal of 4-eV bandwidth. The curves are normalized to the spectral intensity of the backlighter, 7.0×10^{20} keV/(keV ns cm^2 Ω). We note that the two contributions (backlighting and self-emission) are of comparable intensity in this particular case. This indicates that without the use of a monochromator crystal the self-emission will dominate the image and render the method impractical. Thus, if instead of using a monochromator we were to use a filter, the intensity of the monochromatic backlighting radiation (consisting of mostly a single spectral line) will remain about the same, but that of the continuous self-emission will greatly increase. For example, an appropriate filter for the 2.62-Å titanium line would be a 25-μm-thick titanium filter. Such a filter will produce a bandpass of an ~1-keV width (spanning the range ~4 to ~5 keV) as compared with the ~4-eV bandpass of the monochromator crystal.

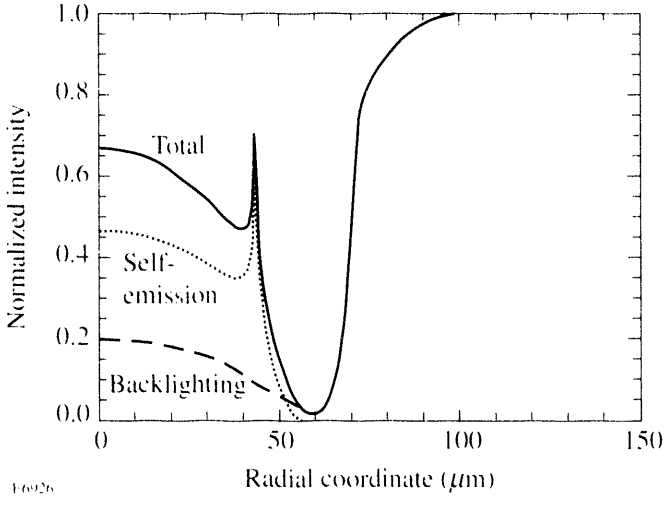

Figure 58.4
The combined image due to backlighting and self-emission at peak compression of an imploded CH shell. The image is calculated assuming a monochromatic detection at the $1s2p$–$1s^2$ line of a titanium backlighter ($\lambda = 2.62$ Å). The curves are normalized to a spectral intensity of 7.0×10^{20} keV/(keV ns cm^2 Ω).

The fact that both image components have comparable intensities makes the imaging method more powerful because information on both the cold shell as well as the interface can be simultaneously obtained. An underperforming target can be expected to show an absorption dip that is both shallower (because of a lower areal density $\rho\Delta r$ along the corresponding chord) as well as displaced to a larger radius (because of a lower compression). If the target performance greatly deviates from predictions (leading normally to a colder core), we may have to employ softer radiation to see a comparable image. Also, the two-dimensional image can show long-wavelength perturbations of the spherical symmetry.

Of particular interest is the spike seen in the self-emission image at a radial distance of ~40 μm. This spike is emitted by the innermost surface of the CH shell and is due to the so-called "limb darkening," or the fact that the depth of a line-of-sight through the rim of a shell is longer than that through its center. In the complete two-dimensional image this spike will appear as a circular ring and will closely correspond to the fuel-shell interface. It provides therefore a direct measure of the achieved compression. Because of the potential usefulness of this spike we study its characteristics in some detail. The spike, if observable, can be used also in experiments with no backlighting. The image will not be then purely monochromatic, as in Fig. 58.4, but will instead be averaged over the transmitted spectrum of the filter. Our calculations also showed that averaging the image over the transmitted spectrum of a 25-μm-thick titanium filter hardly changed the self-emission image in Fig. 58.4.

The spike in Fig. 58.4 is spatially very narrow (~3 μm wide) because only the innermost surface of the CH shell is hot enough to emit the 4.73-keV radiation contributing to the image. As Fig. 58.1 shows, that temperature is in the range ~0.6–1.0 keV. If the core in an actual experiment is colder, the spike will be too weak to be seen, unless we choose softer radiation ($E < 4.7$ keV) for the imaging. Furthermore, an excellent spatial resolution is required. In Fig. 58.5 we show the result of a convolution of the emission image of Fig. 58.4 with an imaging device of 6-μm spatial resolution (and unit magnification). The spike is still seen, but poorer resolution renders it indistinct.

Figure 58.6 shows the self-emission of the test-case target at various photon energies. The motivation is to maximize the spike visibility; therefore, the backlighting part of the image was eliminated. The contrast of the spike with respect to the central peak maximizes in the 4- to 5-keV spectral range. To understand this we turn to Eqs. (11) and (12). The factor $k(E)$ E^3 appearing in Eq. (11) is essentially independent of E. By writing the derivative dE/dT from Eq. (11) we see that at higher photon energies the contrast between the spike and the central emission falls due to the $\exp(E/T)$ factor. This is because the central core is hotter than the shell interface region, and, when E/T is smaller, the exponential term increases more slowly with increasing E. At low photon energies, ab-

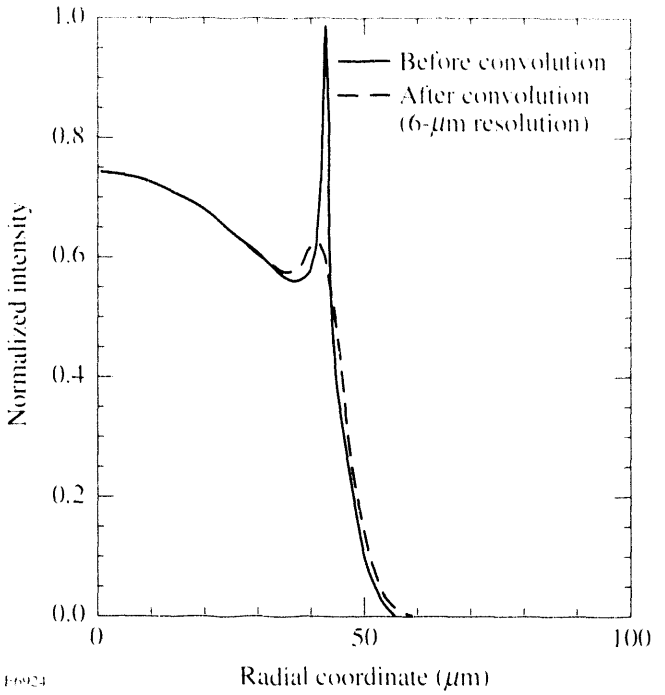

Figure 58.5
Convolution of the emission image of Fig. 58.4 with an imaging device of 6-μm spatial resolution (and unit magnification).

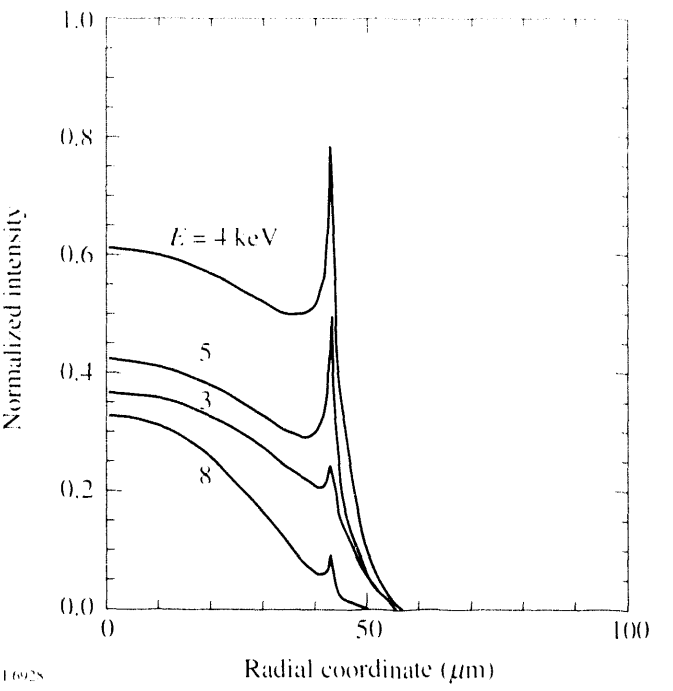

Figure 58.6
Self-emission profiles of the test-case target at various photon energies. The curves are normalized to a spectral intensity of 7.0×10^{20} keV/(keV ns cm^2 Ω).

sorption sets in and the limb-darkening effect disappears. The observed radiation from the hot part of the shell comes from the outer surface of that region and does not depend on its depth.

To maximize the spike emission it is instructive to know the relative contribution of the hydrogenic fuel and the CH shell to the emission profile. Figure 58.7 shows the emission profile of Fig. 58.4 with and without the hydrogenic fuel contribution. Even though the fuel has a lower nuclear charge than the carbon in the CH, a significant fraction of the central emission comes from the fuel because the fuel temperature is considerably higher than that in the shell. To increase the shell emission we may dope the CH shell with a higher-Z element. Irrespective of the detailed atomic physics of a high-Z dopant, its final effect is to increase the absorption coefficient and, through it, the local emission [see Eq. (11)]. To simulate doping we therefore multiply the absorption coefficient (and thereby also the emission coefficient) by a number m, which in Fig. 58.8 assumes the values 1, 2, 4, and 10. The only indeterminate information here is the quantity of a given type of dopant corresponding to each m. Figure 58.8 (calculated for a photon energy of 5 keV) shows that doping the shell cannot increase the contrast of spike to fuel emission because the opacity through the region emitting the spike is not negligible (it is of order 1). For negligible opacities, the strong Z dependence of the absorption coefficient [Eqs. (1) and (2)] when substituted into Eq. (11) will result in much higher emission. However, when opacity is not negligible, the increase in the absorption coefficient, which also appears in the exponent of the attenuation [see Eq. (12)], will dominate and limit the spike intensity to that of a blackbody emitter. Additionally, the doped cold shell will further absorb the radiation emitted at the interface region. The length corresponding to this absorption is longer than through the center; this turns a flat-topped profile, characteristic of a high-opacity emitter, into the bell-shaped profiles for the high-m cases in Fig. 58.8.

Finally, we note that if the spike is still observed in the presence of mixing (which will be the case if the mixing is modest), it would permit an estimate of the degree of mixing. Mixing will raise the fuel emission (hence, the central peak in the image) relative to the spike emission. To simulate this effect, we show in Fig. 58.9 the emission profile when the fuel absorption coefficient is multiplied by $m = 1$, 2, and 4. Since the absorption coefficient of hydrogen is purely due to inverse bremsstrahlung, which depends on Z like Z^2 [see

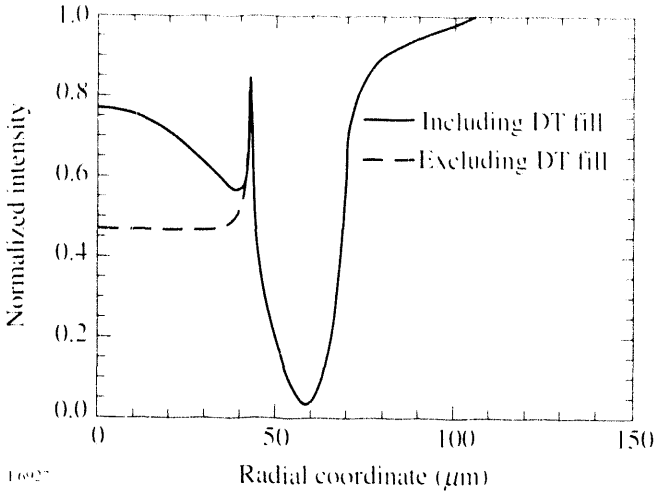

Figure 58.7
Emission profile of Fig. 58.4 with and without the hydrogenic fuel contribution.

Eq. (1)], we can estimate the amount of CH mixed into the fuel for the $m = 4$ case as 8% by atom number. Much higher levels of mixing and shell distortion will make the spike disappear and render this method inapplicable.

Image Monochromatization

To improve the absorption-image visibility we assumed above that the backlighter emission is intercepted by a monochromator crystal that is angle adjusted for peak diffraction at 2.62 Å, the backlighting wavelength. The narrow reflection window of the crystal will greatly reduce the reflected broadband self-emission but will only slightly attenuate the single backlighting line. Roughly, the energy band diffracted by the crystal will be ~1 eV, as compared with a filter transmission window of ~1 keV. Thus, without a monochromator, the peak self-emission flux will be several orders of magnitude higher than the backlighter flux.

We now discuss in more detail the effect of introducing an x-ray reflecting crystal into the detection system. A problem we need to consider is the limitation on the field of view caused by the fact that the wavelength selection by a crystal is related to directional selection. In the dispersion direction, each wavelength can only be diffracted within a narrow angular diffraction range (of the order of $\sim 10^{-4}$ rad) around the Bragg angle. However, the image generated by either a pinhole camera or a microscope can have a larger divergence than the acceptance angle of the crystal, in which case the monochromatic backlighter image may be clipped. For example, a 150-μm image size that is recorded by a pinhole at a distance

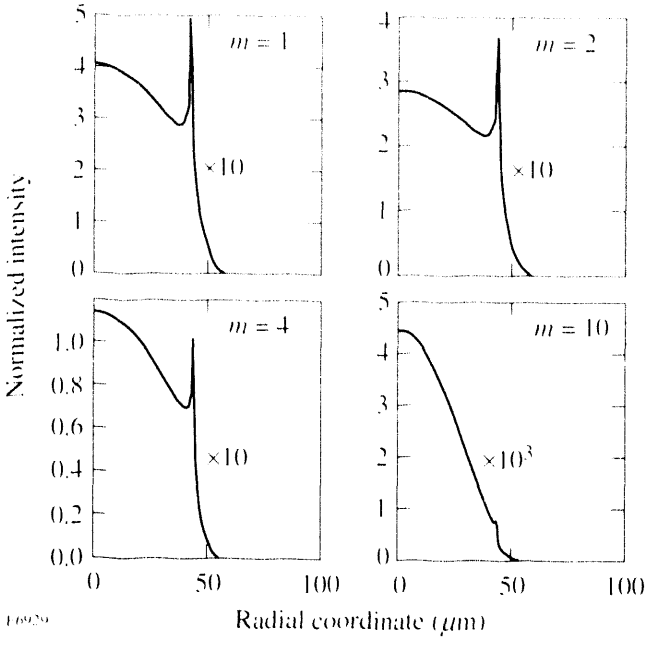

Figure 58.8
Simulation of shell doping with a high-Z additive. The absorption coefficient in the shell is multiplied by m. Detection is at 5-keV photon energy.

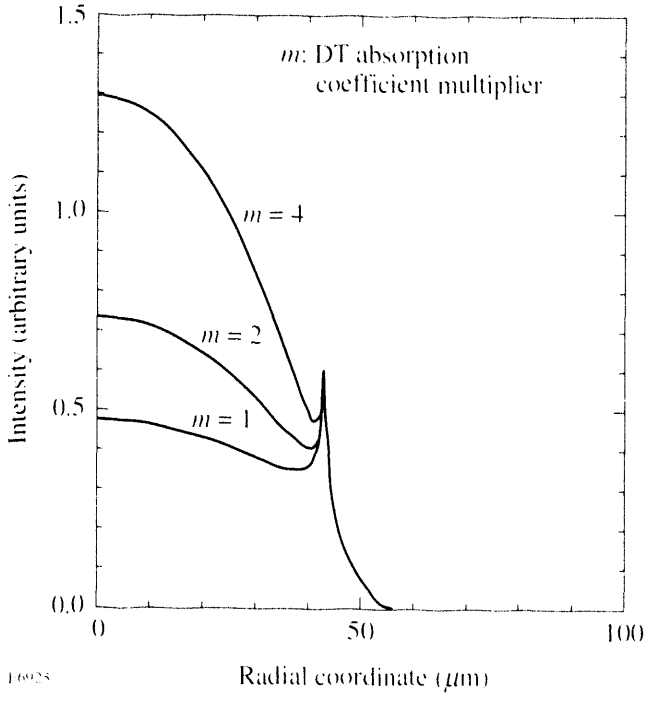

Figure 58.9
Emission profiles when the fuel absorption coefficient is multiplied by m, to simulate shell-fuel mixing. Detection is at 4.73-keV photon energy.

of 50 mm from the target corresponds to a divergence angle of 3×10^{-3} rad. Since an x-ray microscope is placed at longer distances (~200 mm), the divergence is smaller (~7×10^{-4} rad). To minimize the clipping problem we need to maximize the crystal acceptance angle $\Delta\theta_B$ for a given linewidth $\Delta\lambda$. To see the relationship between the two, we differentiate the Bragg condition $2d\sin\theta_B = \lambda$ and obtain

$$E/\Delta E = \lambda/\Delta\lambda = \tan\theta_B/\Delta\theta_B . \qquad (14)$$

The resolving power $\lambda/\Delta\lambda$ is a slowly varying function of the Bragg angle θ_B, so to maximize $\Delta\theta_B$ we should maximize θ_B. This requires selecting a crystal whose 2d spacing is only slightly larger than the relevant wavelength, so that the diffraction angle will be close to 90°. One appropriate choice for the 2.62-Å wavelength is topaz (303), of 2d spacing 2.712 Å, giving a Bragg angle of 74.5°. However, topaz has a high resolution (~6000), which makes $\Delta\theta_B$ narrow. If we choose Ge (111) of 2d = 6.545 Å and resolution ~3000, the Bragg angle for the 2.62-Å line will be only 23.5°. Using Eq. (10) we see that the gain of a factor of ~2 in $\Delta\theta_B$, with respect to topaz (because the resolution is lower), is outweighed by a decrease of a factor of 8 in $\tan\theta_B$.

The resolving power $\lambda/\Delta\lambda$ of topaz (303) was measured[7] to be ~10^4 in the range θ_B = 10°–40°. Extrapolation to θ_B = 74° yields a resolving power of ~6×10^3, which from Eq. (14) corresponds to $\Delta\theta_B = 6 \times 10^{-4}$ rad. This divergence is smaller than that of the image of either the pinhole camera (4×10^{-3}) or the microscope (1×10^{-3}). However, the clipping problem is actually less severe due to the spectral linewidth $\Delta\lambda$. For example, the Doppler width of the 2.62-Å line in a titanium plasma of ion temperature T_i = 500 eV is ΔE_l = 1.2 eV, which corresponds to $\Delta\theta_B = 9 \times 10^{-4}$ rad, about equal to the microscope image divergence. The finite spectral linewidth causes the crystal to reflect in each direction a slightly different wavelength within the linewidth. This eases the clipping problem but results in an intensity reduction of the order of 6/9 = 0.67. The field of view is still a problem for the pinhole-camera imaging, but not for microscope imaging.

The problem of limited field of view can be overcome by using a curved crystal (the Rowland circle geometry[8]), so that all rays forming the image have the same angle of incidence on the crystal. This is strictly true only for a Johansson-bent crystal. The resulting geometry is as follows: A pinhole is placed on the Rowland circle at a location corresponding to the backlighter wavelength (say, 2.62 Å). The target and the backlighter are placed outside the circle. Because of the limitation on the solid angle occupied in the target vacuum tank, only small Bragg angles are feasible. The advantage of large Bragg angles described above disappears, but the focusing geometry compensates for this. A film is placed close to the crystal because farther from the crystal the focusing due to the curvature of the crystal eliminates the imaging. We have then two options for monochromatic imaging, both shown schematically in Fig. 58.10: (a) using an x-ray microscope with a flat crystal (topaz) interposed just in front of the recording medium, and (b) pinhole imaging coupled to a curved-crystal, Rowland-circle spectrometer. In (a) the Bragg angle is large (e.g., 74.5° for topaz), whereas in (b) the Bragg angle is small (12°–18° in our present design).

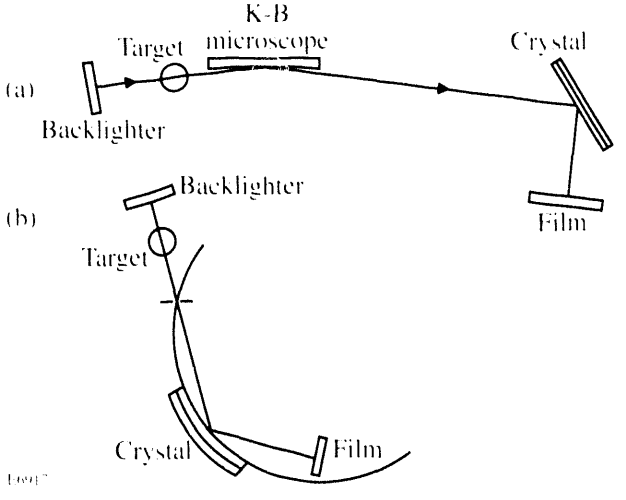

Figure 58.10
Schematic representation of two geometries for monochromatic backlighting: (a) Kirkpatrick-Baez x-ray microscope and a flat diffracting crystal; (b) pinhole imaging with a curved crystal on a Rowland circle.

The basis for imaging with a curved crystal, as stated above, is that all rays diverging from a single point on the Rowland circle and diffracted by a Johansson-type curved crystal fall on the crystal at the same Bragg angle. This assertion needs to be examined since the pinhole located on the Rowland circle [Fig. 58.10(b)] has a finite aperture. To find the divergence due to this finite size, we make use of the dispersion relation[8] of the Rowland spectrometer: $\Delta l = R\,\Delta\theta_B$, where R is the radius of curvature of the crystal (i.e., twice the radius of the Rowland circle) and $\Delta\theta_B$ is the change in the incidence angle on the crystal, corresponding to a travel Δl along the Rowland circle. A choice of R = 60 cm (corresponding to an actual spectrometer under construction at LLE) and Δl = 10 μm (corresponding to a pinhole of that diameter) yields $\Delta\theta_B = 1.67 \times 10^{-5}$ rad. This is smaller than the crystal accep-

tance angle $\Delta\theta_B = 3.5 \times 10^{-5}$ quoted above, meaning that a 10-μm-diam pinhole will not constitute the limiting factor in achieving monochromatic imaging. Instead, that limitation will be given by the imperfection of the crystal manufacturing and bending, as well as of the alignment.

We turn now to a comparison of sensitivity using both methods of imaging. A K-B microscope implemented at LLE[9] has a solid-angular aperture of 3×10^{-7}. For measuring the 4.73-keV titanium line, a gold coating is appropriate, having a reflection efficiency of ~0.3 over the range ~3.0–5.5 keV. The effective throughput (product of the angular aperture and the efficiency) is 9×10^{-8}. For the case of the pinhole-crystal method, a 10-μm-diam pinhole at 50 mm from the target, as assumed above, yields a solid-angular aperture of 4×10^{-8}, smaller than the aperture for the case of a K-B microscope. This is an additional advantage (in addition to the ease of aligning) in using a microscope-crystal combination, as opposed to using a pinhole with a curved crystal. It should be noted that there is no sensitivity gain due to the curvature of the crystal in the latter case because the film is placed very close to the crystal [Fig. 58.10(b)], before any significant focusing occurs. As explained above, such focusing would eliminate the imaging.

The effect of the monochromator bandwidth in reducing the continuum radiation participating in the image was already included (assuming a bandpass of 4 eV). We now calculate the crystal attenuation of the backlighting image for the experimental arrangement shown in Fig. 58.10(a). As it turns out, the results for the arrangement in Fig. 58.10(b) for a particular configuration are very similar.[10] The attenuation of the backlight image due to diffraction off a crystal monochromator is only by a factor of 2–5 because the beam forming the image is quasi-collimated when falling on the crystal.

We estimated above a resolving power of $\sim 6 \times 10^3$ for the topaz crystal at 2.62 Å; this corresponds to an energy window of $\Delta E_c = 0.79$ eV. This happens to be smaller than the generic 4-eV bandwidth assumed in the calculations above. We first note that the divergence of the beam focused by the microscope and incident on the crystal is smaller than the angular reflection curve. If the crystal angle is properly tuned, all rays are approximately incident at the angle of the peak in the reflectivity curve. However, the actual reflectivity is not simply given by the peak reflectivity because of the finite spectral width of the 2.62-Å line. The reflection as a function of wavelength is simply related to the angular reflection curve through the Bragg relation. This curve is approximately a Gaussian with peak reflectivity R_{max} and width ΔE_c. The spectral line shape can also be taken as a Gaussian of width ΔE_l. The effective crystal reflectivity will be lower than R_{max} because only rays of wavelength close to line center fulfill exactly the Bragg diffraction condition; the effective reflectivity is then given by the integral (assuming that the angle of incidence is the Bragg angle of peak reflectivity for the line-center wavelength):

$$R = \left(R_{max}/\Delta E_l \sqrt{\pi}\right) \int_{-\infty}^{\infty} \exp\left[-(\Delta E/\Delta E_l)^2\right] \exp\left[-(\Delta E/\Delta E_c)^2\right] dE = R_{max}\,\Delta E_t/\Delta E_l , \qquad (15)$$

where $\Delta E_t^{-2} = \Delta E_l^{-2} + \Delta E_c^{-2}$. For increasing ΔE, both the incident intensity (first Gaussian) is decreasing as well as the reflectivity (second Gaussian) because the detuning from line center is then larger. ΔE_t should not be construed as a total width; in fact ΔE_t is smaller than either ΔE_l or ΔE_c. As expected, when $\Delta E_l << \Delta E_c$, $R \approx R_{max}$. In the opposite case, when $\Delta E_l >> \Delta E_c$, $R \approx R_{max}\,\Delta E_c/\Delta E_l$. In either case, the reflected intensity drops as we go to larger Bragg angles because (1) the peak reflectivity R_{max} drops for increasing θ_B and (2) ΔE_c also drops for increasing θ_B. Since the resolving power $E/\Delta E$ is usually almost constant as θ_B changes, it means that ΔE_c changes like $\sim 1/\sin\theta_B$. In the case of flat-crystal diffraction we are compelled to pay the price of reduced intensity to ensure a large enough field of view (by going to large Bragg angles, where $\Delta\theta_B$ is larger, even though ΔE_c is smaller). When using a curved crystal (Rowland spectrometer), the field-of-view problem is overcome because of the property of Rowland circle focusing, namely, that all rays diverging from a point on the circle fall on a Johansson-bent crystal at the same angle, enabling us to take advantage of the higher reflectivity at small Bragg angles. On the other hand, small Bragg angles are also mandated by the geometric constraints of the target vacuum chamber.

For the case of the topaz crystal, it was estimated earlier that $\Delta E_c = 0.79$ eV and $\Delta E_l = 1.2$ eV, yielding $R = (0.66/1.2)\,R_{max} = 0.55\,R_{max}$. To estimate R_{max}, we extrapolate the data for the integrated reflectivity of topaz to 7.4 and find $R_{int} \sim 2 \times 10^{-4}$. Using the relationship $R_{int} = \Delta\theta_B \times R_{max}$ and the value of $\Delta\theta_B$ estimated above, we find $R_{max} = 0.33$ and,

finally, the effective reflectivity $R = 0.18$. This attenuation is the price we have to pay for using a monochromator crystal for reducing the contribution of target self-emission.

Conclusions

The expected backlighting and self-emission images of a particular CH target to be imploded on the OMEGA Upgrade are calculated for a variety of experimental parameters. The goal is to image the shell at peak compression with opacity of the order of 1. In this case, the image should delineate the inner surface of the imploded shell (or at least its colder portion), thus providing useful information on the compression and the symmetry. It is shown that to overcome the problem of target self-emission, the image has to be monochromatized with a diffracting crystal, and that the resulting attenuation of the backlighting image is not severe (by a factor of ~5). For the target studied, the two image components are then comparable in intensity, and both provide useful information on target behavior. Two experimental configurations for monochromatic imaging are described: (a) using a microscope and a flat crystal, and (b) using pinhole imaging and a curved crystal in the Rowland geometry. Useful images are obtained with simple (undoped) CH-shell targets and without the need for a short-pulse backlighter beam.

A particularly interesting feature is the appearance in the self-emission of a circular spike that closely delineates the fuel-shell interface but requires high spatial resolution to be observed. The optimization of its appearance is studied. Finally, it is shown that mixing of shell material into the fuel at up to ~10% by atom number might be diagnosable by the spike.

ACKNOWLEDGMENT

This work was supported by the U.S. Department of Energy Office of Inertial Confinement Fusion under Cooperative Agreement No. DE-FC03-92SF19460, the University of Rochester, and the New York State Energy Research and Development Authority. The support of DOE does not constitute an endorsement by DOE of the views expressed in this article.

REFERENCES

1. H. A. Bethe and E. E. Salpeter, in *Quantum Mechanics of One- and Two-Electron Atoms* (Academic Press, New York, 1957), p. 295.
2. H. R. Griem, in *Plasma Spectroscopy* (McGraw Hill, New York, 1964), p. 148, Eq. [6-55].
3. R. W. Lee, B. L. Whitten, and R. E. Stout II, J. Quant. Spectrosc. Radiat. Transfer **32**, 91 (1984).
4. J. C. Stewart and K. D. Pyatt, Jr., Astrophys. J. **144**, 1203 (1966).
5. B. Yaakobi, P. Bourke, Y. Conturie, J. Delettrez, J. M. Forsyth, R. D. Frankel, L. M. Goldman, R. L. McCrory, W. Seka, J. M. Soures, A. J. Burek, and R. E. Deslattes, Opt. Commun. **38**, 196 (1981); D. L. Matthews *et al.*, J. Appl. Phys. **54**, 4260 (1983).
6. H. R. Griem, *Plasma Spectroscopy* (McGraw Hill, New York, 1964), Eq. (7-6).
7. K. Gisselberg, Ark. Fys. **30**, 359 (1965).
8. B. Yaakobi, T. Boehly, and P. Audebert, Rev. Sci. Instrum. **61**, 1915 (1990).
9. Laboratory for Laser Energetics LLE Review **46**, NTIS document No. DOE/DP/40200-156, 1991 (unpublished), p. 91.
10. B. Yaakobi, F. J. Marshall, R. Epstein, and Q.Su, "Monochromatic Backlighting as a Laser-Fusion Diagnostic," to appear in the Journal of X-Ray Science and Technology.

Effect of Electron Collisions on Ion-Acoustic Waves and Heat Flow

Introduction

The damping rate of ion-acoustic waves in plasma plays an important role in establishing the threshold for the onset of stimulated Brillouin scattering, ion-temperature-gradient instability, current-driven ion-acoustic instability, and other drift-wave microinstabilities. The effect of electron-ion (e-i) collisions on the ion-acoustic damping rate has been recently investigated by analytically solving the electron Fokker-Planck (FP) equation for a Lorentz plasma (i.e., neglecting e-e collisions) with cold ions and arbitrary $k\lambda_{ei}$ (where k is the wave number and λ_{ei} is the e-i mean free path).[1] It was shown that, as e-i collisions are introduced, the damping rate γ rises monotonically above the collisionless Landau limit γ_L, reaches a peak at $k\lambda_{ei} \sim (Zm_e/m_i)^{1/2}$ (where Z is the charge number and m is the mass), and then decreases to zero as $k\lambda_{ei} \rightarrow 0$ with the damping rate γ_{fluid} predicted by fluid theory.

The main purpose of this article is to assess the contributions from both e-e and e-i collisions on the damping of the ion-acoustic waves. Results are based on numerical simulations using a code (*SPRING*) that solves the linearized electron FP and cold-ion fluid equations. We are able to explore a wide range of values of $k\lambda_{ei}$ and Z by expanding the electron-distribution function in an arbitrary number of Legendre modes, and by using the *exact* form of the Rosenbluth[2] potentials (neglecting terms of the order of m_e/m_i). In the high-Z limit, where e-e collisions can be ignored, the analytic Lorentz-plasma results of Epperlein *et al.*[1] are recovered. For low-Z plasmas, e-e collisions become significant and promote a reduction in the damping near $k\lambda_{ei} = 1$, though γ still remains larger than γ_L and γ_{fluid}. The approximation of isotropic Rosenbluth potentials is also investigated and found to yield sufficiently accurate values of γ (error <10%). A further useful approximation that involves adjusting the e-i collision frequency to simulate the strength of e-e collisions is shown to be similarly accurate. Although finite ion-temperature effects have been neglected in the current analysis, their contribution to γ has been investigated by Randall[3] and more recently by Tracy *et al.*,[4] who calculated the ion-acoustic eigenfrequency ω for arbitrary $k\lambda_{ii}$ (where λ_{ii} is the i-i mean free path) and isothermal electrons.

It is also of interest to calculate the effective (or generalized) thermal conductivity κ based on the perturbed distribution function and compare it to the classical Spitzer-Härm (SH)[5] conductivity κ_{SH}. Not only does this give insight into electron kinetic effects, but it can also provide a way of incorporating kinetic effects into fluid equations. This idea has been successfully used in the context of electron heat transport in laser-produced plasmas[6] and more recently in the context of drift-wave microinstabilities in tokamak plasmas.[7,8] In particular, generalized thermal conductivities have been calculated by Hammett and Perkins[7] (κ_{HP}) for collisionless plasmas, and by Chang and Callen[8] for arbitrary $k\lambda_{ei}$, ω, and Z.

The results for κ calculated here are shown to reproduce the analytic results of Epperlein *et al.*[1] obtained in the Lorentz plasma approximation. In the collisional limit ($k\lambda_{ei} << 1$) κ approaches κ_{SH}, and in the collisionless limit ($k\lambda_{ei} >> 1$) it approaches κ_{HP}. We find, however, significant discrepancies with the results of Chang and Callen. They underestimate κ by factors ranging from 2.4 (at $Z = 1$) to 7.1 (as $Z \rightarrow \infty$) in the collisional limit.

The introduction of a spatially modulated inverse-bremsstrahlung heating source has also been recently shown to significantly reduce the effectiveness of heat conduction when $k\lambda_{ei} >> 1$.[9] A simple analytic formula for $\kappa_{\text{IB}}/\kappa_{\text{SH}}$ as a function of $k\lambda_{ei}$ has been proposed, based on simulations with an approximate form of the FP equation. Here we are able to assess the accuracy of the κ_{IB} formula and show that the reduction in conductivity (relative κ_{SH}) for $k\lambda_{ei} >> 1$ is indeed larger than for the undriven case, with freely propagating sound waves.

In the following sections, we describe the electron FP and cold-ion fluid equations and the numerical scheme (*SPRING* code) adopted for their solution; finally, our results are presented and summarized.

Electron Fokker-Planck and Cold-Ion Fluid Equations

Our model consists of a quasi-neutral homogeneous background plasma with fully ionized ions. The full electron FP operator is used, with the exception of e-i energy-exchange terms (which provide contributions of the order of $m_e/m_i << 1$). Adopting a perturbation of the electron distribution function of the form

$$f(x, \mathbf{v}, t) = F_0(v) + \sum_{l=0}^{L} f_l(v, t) P_l(\mu) \exp(ikx), \tag{1}$$

where $\mu = v_x/v$ and $P_l(\mu)$ is the lth Legendre mode, the linearized electron FP equation (defined in the rest frame of the ions) becomes[10]

$$\frac{\partial f_0}{\partial t} + \frac{ikv}{3} f_1 - \frac{iku_i}{3} v \frac{\partial F_0}{\partial v} = C_{ee}^i(F_0, f_0) + C_{ee}^i(f_0, F_0), \tag{2}$$

$$\frac{\partial f_1}{\partial t} + ikvf_0 + ikv\frac{2}{5} f_2 - \left(\frac{|e|E}{m_e} + \frac{\partial u_i}{\partial t}\right)\frac{\partial F_0}{\partial v}$$

$$= -\nu_{ei} f_1 + C_{ee}^i(F_0, f_1) + C_{ee}^a(F_0, f_1), \tag{3}$$

$$\frac{\partial f_2}{\partial t} + \frac{2}{3} ikvf_1 + \frac{3}{7} ikvf_3 - \frac{2}{3} iku_i v \frac{\partial F_0}{\partial v}$$

$$= -3\nu_{ei} f_2 + C_{ee}^i(F_0, f_2) + C_{ee}^a(F_0, f_2), \tag{4}$$

and

$$\frac{\partial f_l}{\partial t} + \frac{l}{2l-1} ikvf_{l-1} + \frac{l+1}{2l+3} ikvf_{l+1}$$

$$= -\frac{l(l+1)}{2} \nu_{ei} f_l + C_{ee}^i(F_0, f_l) + C_{ee}^a(F_0, f_l) \tag{5}$$

for $l > 2$. The ion velocity u_i and electric field E are first order in the perturbation, and

$$F_0(v) = N_e\left(2\pi v_t^2\right)^{-3/2} \exp\left(-v^2/2v_t^2\right)$$

is an equilibrium Maxwellian, where N_e is the background electron number density, $v_t = (T_e/m_e)^{1/2}$ is the electron thermal velocity, and T_e is the electron temperature (in energy units). The velocity-dependent e-i collision frequency is given by

$$\nu_{ei}(v) = 4\pi N_e Z\left(e^2/m_e\right)^2 \ln\Lambda/v^3,$$

where e is the electron charge and $\ln\Lambda$ is the Coulomb logarithm (assumed the same for both electrons and ions). The terms C_{ee}^i and C_{ee}^a (defined in the Appendix) represent the isotropic and anisotropic parts of the e-e collision operator, respectively. Since the latter involves integration over the perturbed distribution function, it is usually neglected in FP calculations.[11] The validity of such approximation is the subject of "Approximations to the Fokker-Planck Equation" on p. 72.

The linearized cold-ion continuity and momentum equations are

$$\frac{\partial n_i}{\partial t} + ikN_i u_i = 0, \tag{6}$$

and

$$N_i m_i \frac{\partial u_i}{\partial t} = ZN_i |e| E + R_{ie}, \tag{7}$$

where $R_{ie} = (4\pi m_e/3)\int dv v^3 \nu_{ei} f_1$ is the i-e momentum exchange rate, n_i is the perturbed ion number density, and N_i is its background value. The perturbed electric field is calculated via Poisson's equation,

$$ikE = 4\pi |e|\left(Zn_i - n_e\right), \tag{8}$$

where the perturbed electron number density is $n_e = 4\pi\int_0^\infty v^2 f_0 dv$.

Numerical Scheme (*SPRING* code)

A computer code (*SPRING*) has been written to solve Eqs. (2)–(8). It uses a "time-splitting" scheme with the following stages:

$$\frac{\partial f_1}{\partial t} = \left(\frac{|e|E}{m_e} + \frac{\partial u_i}{\partial t} \right) \frac{\partial F_0}{\partial v} \qquad \text{(acceleration)},$$

$$\frac{\partial f_0}{\partial t} = \frac{iku_i}{3} v \frac{\partial F_0}{\partial v} \qquad \text{(compression)},$$

$$\frac{\partial f_2}{\partial t} = \frac{2}{3} iku_i v \frac{\partial F_0}{\partial v} \qquad \text{(viscosity)},$$

$$\frac{\partial f_0}{\partial t} = C_{ee}^{i}(F_0, f_0) + C_{ee}^{i}(f_0, F_0)$$

$$\frac{\partial f_l}{\partial t} = C_{ee}^{i}(F_0, f_l) + C_{ee}^{a}(F_0, f_l) \qquad \text{(e-e collision)},$$

and

$$\frac{\partial f_l}{\partial t} = -\frac{l}{2l-1} ikv f_{l-1} - \frac{l+1}{2l+3} ikv f_{l+1} - \frac{l(l+1)}{2} \nu_{ei} f_l$$

(advection and e-i angular scattering),

where $l > 0$. The acceleration, compression, and viscosity stages are advanced explicitly in time. In the e-e collision stage, the isotropic collision operators (which are differential operators) are evaluated implicitly using the Chang-Cooper[12] scheme, whereas the anisotropic operators (which are integral operators) are evaluated explicitly. In the advection-scattering stage, f_l is solved implicitly at each velocity group, using the boundary condition that $f_{-1} = f_{L+1} = 0$. The distribution function is defined on a velocity mesh with constant spacing of typically $\Delta v = 0.125 v_t$ between $v = 0$ and $6v_t$.

After advancing the distribution function in time, with a fixed time step Δt, the ion-fluid equations are solved explicitly. However, solving Poisson's equation explicitly to calculate E can lead to numerical instabilities when $\Delta t\, \omega_p > 1$ [where $\omega_p = \left(4\pi N_e e^2 / m_e\right)^{1/2}$ is the plasma frequency]. To avoid this problem we use an implicit-moment method,[13] which involves taking density and momentum moments of the FP equation and substituting back into the ion continuity and Poisson's equations. An approximation to the electric field at a time $(t + \Delta t)$ can then be obtained from

$$ikE(t + \Delta t) = \frac{4\pi|e|}{\left(1 + \omega_p^2 \Delta t^2\right)} \left\{ Zn_i(t) - n_e(t) + ik\Delta t N_e \left[v_e(t) + ik\Delta t p(t)/N_e m_e - \Delta t R_{ie}(t)/N_e m_e \right] \right\}, \quad (9)$$

where $p = (4\pi m_e/3) \int dv v^4 f_0$ and $v_e = (4\pi/3N_e) \int dv v^3 f_1$. Since we are interested in low-frequency phenomena, such as sound waves, Eq. (9) allows us to use time steps larger than ω_p^{-1}.

The sound-wave eigenfrequencies are determined by appropriately initializing the dependent variables and monitoring their temporal evolution over several wave periods. In the past, simulations of this kind (involving the ion FP equation) have suffered from the occurrence of spurious transients that required complicated procedures to filter out the correct eigenfrequencies.[3] This problem appears to be associated with the fact that the "exact" perturbed eigenfunctions f_l are not known *a priori*. Rather than trying to guess f_l, a more satisfactory approach is to start with $f_l = n_i = 0$ and $u_i = 1$. The variables then typically converge to the appropriate eigenmodes within a few sound-wave periods. (An alternative approach based on eigenvalue analysis has also been proposed by Tracy *et al.*[4])

SPRING Simulation Results

The code *SPRING* provides ion-acoustic damping rates γ/kc_s for different values of $k\lambda_{ei}$, $k\lambda_D$, Z, and A, where

$$\lambda_{ei} = 3T_e^2 \Big/ \left[4(2\pi)^{1/2} N_e Z e^4 \ln \Lambda \right],$$

$\lambda_D = v_t/\omega_p$ is the Debye length, A is the atomic mass, and $c_s = \left(ZT_e/m_i\right)^{1/2}$ is the isothermal sound speed. The code also calculates an effective thermal conductivity defined by $\kappa \equiv -q_{FP}/ikT_{FP}$, where

$$q_{FP} = (2\pi m_e/3) \int dv\, v^5 f_1$$

is the electron heat flow and

$$T_{\mathrm{EP}} = (4\pi m_e / N_e)\int dv\left(v^4/3 - v^2 v_t^2\right) f_0$$

is the temperature. Since we are primarily concerned with collisional effects, we choose $\lambda_{ei} << k^{-1}$; also, for simplicity, we take $A = 2Z$.

1. Damping rate γ

The first test of *SPRING* involves neglecting e-e collisions altogether. This is equivalent to using the Lorentz plasma approximation, or high-Z limit, since $\nu_{ei}/\nu_{ee} \sim Z$. In this instance Eqs. (2)–(8) can be solved analytically by the method of continued fractions (see Ref. 1), and the results are plotted as curve d in Fig. 58.11. The code is found to reproduce these damping rates very accurately throughout the whole range of $k\lambda_{ei}$. (In practice, this requires using $Z >> 10^4$.)

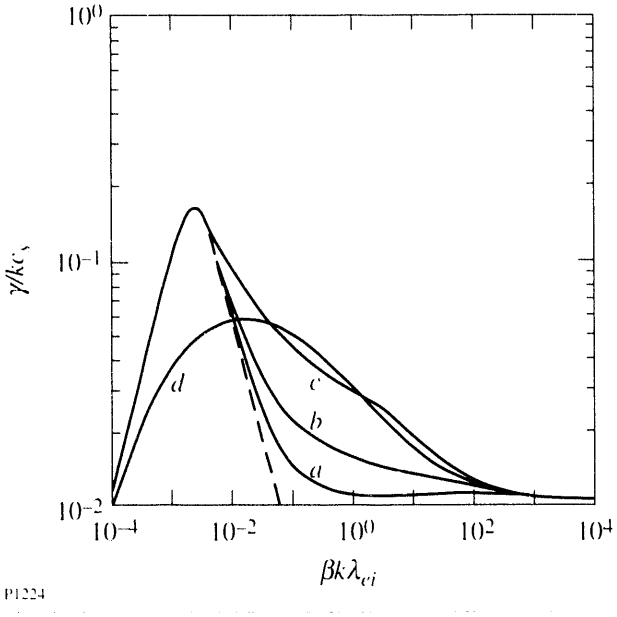

Figure 58.11

Plots of the damping rate of ion-acoustic waves γ/kc_s as functions of $\beta k\lambda_{ei}$, where c_s is the isothermal sound speed, k is the perturbation wave number, λ_{ei} is the electron-ion mean free path, and β is a scaling factor ($\beta = 0.24$, 0.68, 0.92, and 1 for $Z = 1$, 8, 64, and ∞, respectively). Solid curves represent *SPRING* simulations with (a) $Z = 1$, (b) $Z = 8$, (c) $Z = 64$, and (d) $Z = \infty$. The dashed curve refers to the fluid result.

To test the accuracy of the numerical implementation of the e-e operators we first consider the collisional case ($k\lambda_{ei} << 1$) with $Z = 1$. In this limit the Legendre expansion [Eq. (1)] can be truncated at $l = 1$, and f_0 approaches a perturbed Maxwellian. Since this is also the fluid limit, a sound-wave dispersion relation can be derived using the standard fluid equations (neglecting viscosity effects) with the Spitzer-Härm thermal conductivity $\kappa_{\mathrm{SH}} = \gamma_0(Z) N_e v_t \lambda_{ei}$, where the Z-dependent, thermal-conductivity coefficient is approximately given by $\gamma_0(Z) \approx 3.20(0.24 + Z)/(1 + 0.24Z)$ and $\gamma_0(\infty) = 128/3\pi$. The resultant dispersion relation (using $\partial/\partial t = -i\omega$) is found to be

$$\left(\frac{\omega}{kc_s}\right)^2 = \frac{2}{3 + i\left(\frac{\omega}{kc_s}\right)3r} + 1 , \qquad (10)$$

where r is the ratio of the thermal diffusion rate $\left(2k^2\kappa_{\mathrm{SH}}/3N_e\right)$ to the sound transit rate (kc_s) across k^{-1}. Since $r = 2\gamma_0 k\lambda_{ei}\left(m_i / Zm_e\right)^{1/2}/3$, it has been found convenient to plot γ/kc_s as a function of $\beta k\lambda_{ei}$, where

$$\beta = (A/2Z)^{1/2}\,\gamma_0(Z)/\gamma_0(\infty)$$

is a scaling factor of order unity. The damping rates based on Eq. (10) are plotted in Fig. 58.11 (dashed curve). *SPRING* simulation results are found to be in good agreement with these as $k\lambda_{ei} \to 0$.

Let us now consider the more interesting case of finite Z and $k\lambda_{ei}$. The results are shown in Fig. 58.11 (solid curves a–c) for $Z = 1$, 8, and 64. Starting from the large $k\lambda_{ei}$ limit, we note that the dominant collisional contribution comes from e-i collisions. [Here, a large number of Legendre modes are necessary to accurately model the damping (e.g., typically $L = 20$ for $\beta k\lambda_{ei} = 10^{-2}$).] In the intermediate regime of $\beta k\lambda_{ei} \sim 1$ we find the peculiar result that e-e collisions actually reduce the damping rate. The reason for this becomes apparent if we consider the nature of the electron collisional process. As shown by Epperlein *et al.*[1] elastic scattering between electrons and ions gives rise to both sound-wave damping, through thermal diffusion, and sound-wave "undamping," through disruption of the Landau wave-particle interaction. However, the main collisional contribution between electrons is energy exchange, which acts to drive f_0 toward a perturbed Maxwellian. Hence, introducing e-e collisions can actually reduce the damping rate by bringing it closer to the fluid limit. Since $\nu_{ei}/\nu_{ee} \sim Z$, this effect is strongest for low-Z plasmas. (Although γ does not fall below γ_L for $\beta k\lambda_{ei} > 0.01$, if we artificially reduce the value of Z, we can effectively extend the "fluid limit" to larger values of $k\lambda_{ei}$ and thereby allow γ to be less than γ_L.)

To a lesser extent, e-e collisions also affect the anisotropic parts of the electron distribution function (i.e., f_1, f_2, ...). For example, the e-e collision terms on the RHS of Eq. (3) are responsible for reducing the thermal conductivity, thus giving rise to the Z-dependent thermal coefficient χ_0 in the fluid limit.

2. Approximations to the Fokker-Planck equation

The e-e collision operator for $l > 0$ (see Appendix) can be separated into an isotropic part $C_{ee}^{a}(f_0, f_l)$, which involves derivative operations on f_l, and an anisotropic part $C_{ee}^{a}(f_0, f_l)$, which involves integral operations on f_l. Since the latter is more difficult to implement numerically, it is usually neglected in electron FP calculations. Here we investigate the implications of neglecting both $C_{ee}^{a}(f_0, f_l)$ and $C_{ee}^{a}(f_0, f_l)$ for $l > 0$ and how we can simulate their effects by appropriately adjusting the value of ν_{ei}. We also briefly explore the possibility of using a generalized collision frequency to simulate the contribution from an infinite Legendre-mode expansion.

The effect of neglecting e-e collisions altogether (the so-called Lorentz approximation) has already been demonstrated in Fig. 58.11. There we see that apart from the weakly collisional regime $\beta k \lambda_{ei} >> 1$, where electron collisions play a relatively minor role in the sound-wave damping, or the strongly collisional regime $(\beta k \lambda_{ei} << 10^{-4})$, where the thermal diffusion rate is much less than sound transit rate, it is not reasonable to neglect e-e collisions for $Z < 64$. This is especially true near the maximum value of γ/kc_s at $\beta k \lambda_{ei} = 0.002$, where even for $Z = 64$ the Lorentz approximation leads to large errors.

The first approximation we consider uses isotropic Rosenbluth potentials only (i.e., setting $C_{ee}^{a} = 0$). Figure 58.12 shows a comparison of the damping rate (open circles) with the more accurate calculation discussed in the previous section. We note that the largest errors occur over the range $10^{-1} < \beta k \lambda_{ei} < 10^{1}$ with an overall maximum of about 10%. Since the relative contribution from e-e collisions is most significant for low Z, the worst possible case occurs with $Z = 1$.

The second approximation neglects e-e collisions altogether for $l > 0$ (i.e., setting $C_{ee}^{l} = C_{ee}^{a} = 0$ for $l > 0$). To offset this more drastic approximation we introduce a modified collision frequency $\nu_{ei}^{*} = [\gamma_0(\infty)/\gamma_0(Z)]\nu_{ei}$. The new factor $[\gamma_0(\infty)/\gamma_0(Z)] = (Z + 4.2)/(Z + 0.24)$ has the effect of giving the correct (SH) thermal conductivity in the collisional limit. A plot of the corresponding damping rate for $Z = 1$ (the crosses in Fig. 58.12) shows that, once again, the errors are larger at intermediate values of $\beta k \lambda_{ei}$ with a maximum of about 10%. As in the previous case, this low Z example provides the worst possible case.

The advantage of neglecting e-e collisions for $l > 0$ (through the introduction of ν_{ei}^{*}) is that Eqs. (3)–(5) become algebraic in v, allowing for much faster numerical solution of the coupled equations.

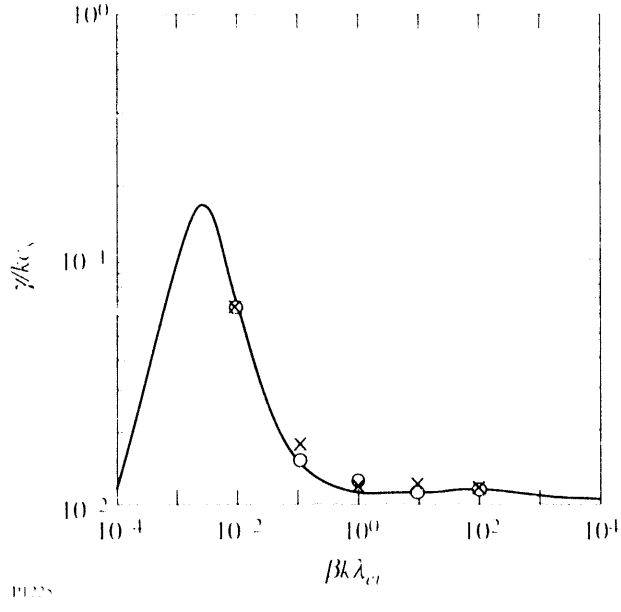

Figure 58.12
Plots of the damping rate of ion acoustic waves γ/kc_s as functions of $\beta k \lambda_{ei}$ for $Z = 1$ (as in Fig. 58.11). Results using isotropic Rosenbluth potentials are displayed as open circles, whereas those using ν_{ei}^{*} are displayed as crosses.

Provided we are only interested in low-frequency waves [such that $\omega << \nu_{ei}(v_t)$], we can now go a step further and use the techniques of Ref. 1 to reduce Eqs. (3)–(5) to a single equation,

$$ikvf_0 = \left[\frac{|e|E}{m_e} + \frac{\partial u_l}{\partial t} + \left(\nu^{*} - \nu_{ei}^{*}\right)u_l\right]\frac{\partial f_0}{\partial v} - \nu^{*} f_1 . \quad (11)$$

Here, $\nu^{*}(k) = \nu_{ei}^{*}\left[1 + \left(\pi k v/6\nu_{ei}^{*}\right)^2\right]^{1/2}$ is the low-frequency generalized collision frequency proposed by Epperlein *et al.*,[1] which incorporates the contribution from all Legendre modes with $l > 1$. By substituting Eq. (11) into Eq. (2), we are left with a single differential equation for f_0, which is easier to solve than the original set of coupled equations. However, a discussion of the numerical methods involved is outside the scope of this article.

3. Effective thermal conductivity κ

Figure 58.13 plots (a) $|\kappa/\kappa_{SH}|$ and (b) $\arg(\kappa)$ as functions of $\beta k\lambda_{ei}$ for $Z = 1$, 8, 64, and ∞ (solid curves). The dashed curve shows the results of Hammett and Perkins (for a collisionless plasma).

When neglecting e-e collisions (Lorentz plasma approximation), our results agree with the analytic solutions of Ref. 1. In the collisional limit ($k\lambda_{ei} << 1$), we have $\kappa = \kappa_{SH}$, whereas in the collisionless limit ($k\lambda_{ei} >> 1$), we have $\kappa = \kappa_{HP} = 3(2/\pi)^{1/2} N_e v_t/|k|$ [see dashed curve HP in Fig. 58.13(a)]. (The formula for κ_{HP} is 1.5 times larger than the one used by Hammett and Perkins since ours is defined in terms of the isotropic temperature T_{FP}.) Comparing our results with those of Chang and Callen,[8] however, we find considerable discrepancy in the $k\lambda_{ei} << 1$ limit. Although the authors point out in their paper that they underestimate the thermal conductivity by a factor of 2.4 for $Z = 1$, this factor actually rises up to 7.1 for $Z >> 1$.

Two mechanisms can be identified that reduce the heat flow below the SH limit, q_{SH}. The first one is caused by a departure of f_0 from the perturbed Maxwellian.[14] When the mean free path of heat-carrying electrons (with velocities close to $3.6\, v_t$) becomes greater than k^{-1}, their spatial gradient in configuration space is reduced. Since these relatively collisionless electrons cannot thermalize instantaneously with thermal electron population (as required by fluid theory), the heat flow is reduced below q_{SH}. The reduction in heat flow is therefore governed by the balance between the thermal-diffusion rate and the e-e thermalization rate [as given by the collision term in Eq. (2)]. In the Lorentz plasma approximation, where e-e collisions are neglected altogether, there is no effective coupling between different electron-energy groups, as illustrated by the large phase shift between q_{FP} and T_{FP} in Fig. 58.13(b). As seen in Figs. 58.13(a) and 58.13(b), the departure from fluid theory then becomes significant when $r \sim k\lambda_{ei}(m_i/Zm_e)^{1/2} > 1$, i.e., when the thermal-diffusion time becomes less than the hydrodynamic time. As e-e collisions are introduced (identified by the finite-Z curves), f_0 is driven closer to a perturbed Maxwellian and the onset of kinetic effects is shifted to larger values of $k\lambda_{ei}$. The phase difference between q_{FP} and T_{FP} is also considerably reduced by the introduction of e-e collisions and becomes negligible for $Z = 1$ [see Fig. 58.13(b)].

Regardless of the e-e thermalization strength, the electron heat flow cannot exceed the "free-streaming," or collision-

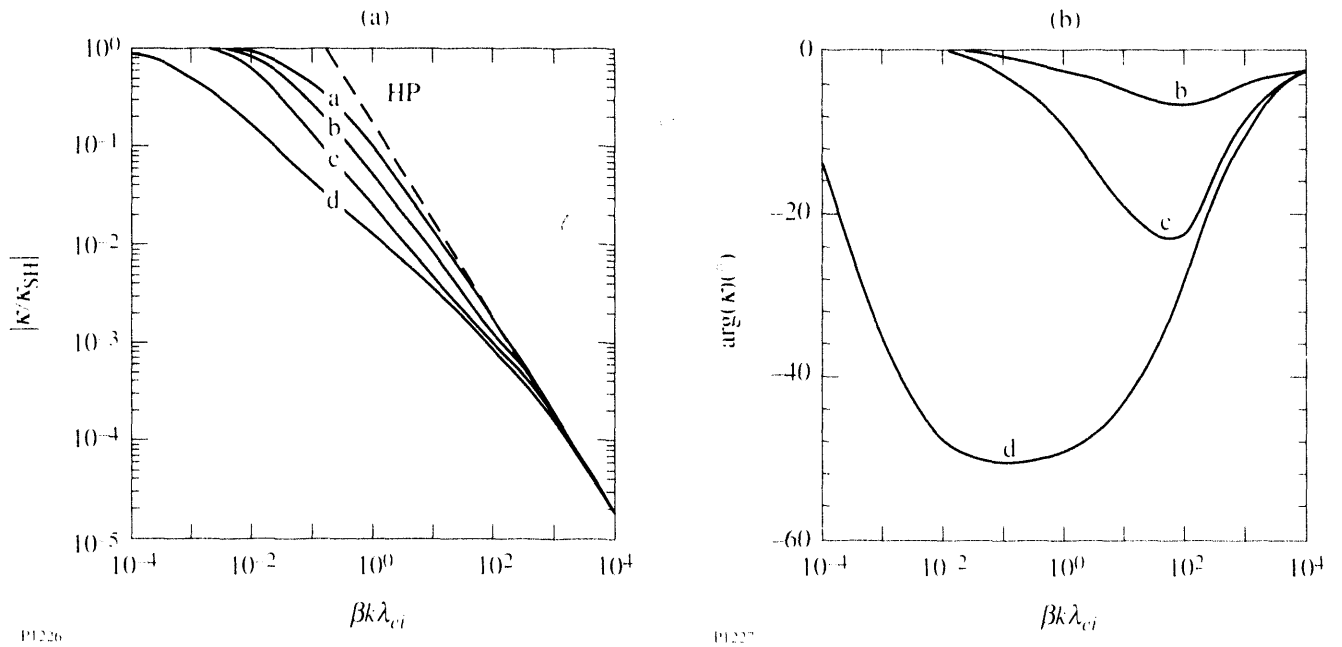

Figure 58.13
Plots of (a) $|\kappa/\kappa_{SH}|$ and (b) $\arg(\kappa)$ as functions of $\beta k\lambda_{ei}$, where κ and κ_{SH} are the effective and Spitzer-Härm thermal conductivities, respectively. As in Fig. 58.11, the solid curves refer to *SPRING* simulation results with (a) $Z = 1$, (b) $Z = 8$, (c) $Z = 64$, and (d) $Z = \infty$ [for $Z = 1$, $\arg(\kappa) << 1$]. Here the dashed curve refers to the model of Hammett and Perkins.

less, limit as calculated by Hammett and Perkins,[7] i.e., $q_{HP} = (ik/|k|)3(2/\pi)^{1/2} N_e T_e v_t$. This gives us the second mechanism for the reduction of κ with the upper limit shown by the plot of $\kappa_{HP}/\kappa_{SH} = 9(2\pi)^{1/2}(A/Z)^{1/2}/(128/\beta k\lambda_{ei})$ (dashed curve) in Fig. 58.13(a).

Other processes can also affect the electron thermal conductivity. Inverse-bremsstrahlung heating, for example, preferentially heats low-velocity electrons, which in turn modifies f_0 and leads to even further reduction of κ.[9] Such a phenomenon has been recently investigated and shown to have a significant impact on both filamentation[9] and stimulated Brillouin scattering[15] in laser-produced plasmas. The corresponding values of κ have been calculated using the nonlinear FP code *SPARK*; the following analytical fit to the simulation results has been proposed:[9]

$$\frac{\kappa_{IB}}{\kappa_{SH}} = \frac{1}{1 + (30k\lambda_e)^{4/3}}, \qquad (12)$$

where $\lambda_e = \eta T^2 / \left[4\pi N_e e^4 Z^{1/2} \ln \Lambda\right]$ is the electron delocalization length and $\eta = \left[\gamma_0(Z)/\gamma_0(\infty)\right]^{1/2}$. (As observed in Ref. 9, certain care is needed in defining Z for multispecies ions.) The resulting dashed curve (IB) for $Z = 1$ is plotted in Fig. 58.14 as a function of $\beta k\lambda_{ei}$. Although the original simulation results were based on a two-Legendre-mode expansion for the distribution function (i.e., $L = 1$), the contribution from higher-order modes have been investigated by Epperlein and Short[6] [using a generalized collision frequency ν' of the type discussed in "Approximations to the Fokker-Planck equation"] and found to be negligible.

Here, we are able to check on the accuracy of Eq. (12) by using *SPRING* with an inverse-bremsstrahlung heating source of the type[16]

$$\frac{1}{v^2}\frac{\partial}{\partial v}\left(\frac{g}{v}\frac{\partial f_0}{\partial v}\right)$$

inserted on the right-hand side of Eq. (2), where

$$g = \left[1 + (\nu_{ei}/\omega_0)^2\right]^{-1}$$

and ω_0 is the light-wave frequency. The code is then run until the distribution function reaches a steady state. In this case, ion motion does not play a significant role. The corresponding values of κ/κ_{SH} (also for $Z = 1$) have been calculated for range of $k\lambda_{ei}$ and displayed as circles in Fig. 58.14. As shown, the simple analytic fit [Eq. (12)] can accurately reproduce the more accurate *SPRING* simulation results. For comparison, the values of κ for an undriven plasma [curve $Z = 1$ in Fig. 58.13(a)] has also been plotted in Fig. 58.14.

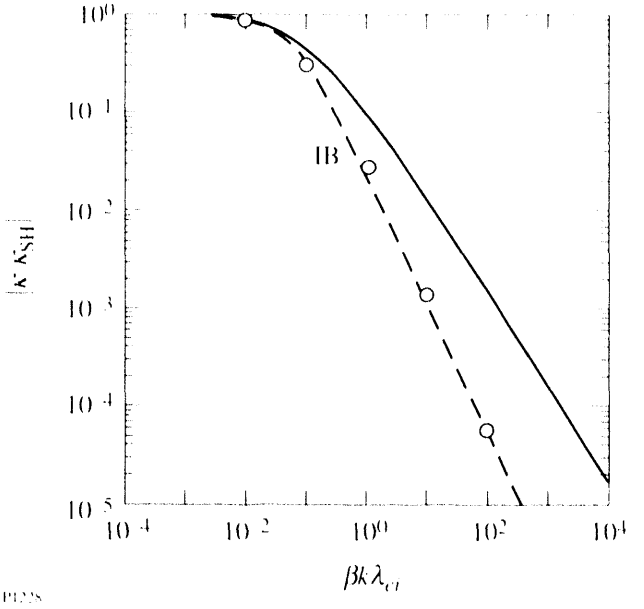

Figure 58.14
Plot of κ/κ_{SH} as a function of $\beta k\lambda_{ei}$ for $Z = 1$ (as in Fig. 58.13). Here the dashed curve refers to the analytic formula for κ_{IB} (from Ref. 9), and circles represent *SPRING* simulation results with an inverse-bremsstrahlung heating source.

Summary

The effect of electron collisionality on the damping of ion-acoustic waves has been investigated by numerically solving the electron FP and cold-ion-fluid equations. The code (*SPRING*) developed for this purpose reproduces the analytic results previously obtained for a Lorentz plasma (i.e., without e-e collisions).

The introduction of e-e collisions shows that the Lorentz approximation is inadequate near the peak of the damping rate at $k\lambda_{ei} \sim (Zm_e/m_i)^{1/2}$. For $k\lambda_{ei} \gg (Zm_e/m_i)^{1/2}$ and $Z < 64$, e-e collisions reduce the damping rate below the Lorentz value, though it still remains higher than the γ_{fluid} and γ_1.

A convenient approximation that involves adjusting the e-i collision frequency to model the contribution from e-e collisions for $Z > 1$ has been found to yield errors of up to 10% in the damping rate. A further generalization of the e-i collision

frequency that simulates the contribution from all Legendre modes with $l > 1$ has also been discussed.

Calculations of the effective thermal conductivity κ for a Lorentz plasma have shown significant reduction from the Spitzer-Härm value κ_{SH} for $k\lambda_{ei} > 10^{-4}$. However, even for Z as high as 64, e-e collisions extend the validity of the fluid approximation for up to $k\lambda_{ei} \sim 10^{-2}$. In the limit as $k\lambda_{ei} \to \infty$, κ approaches the value $3(2/\pi)^{1/2} N_e v_t / k$ predicted by Hammett and Perkins.

Heating the plasma with a spatially modulated inverse-bremsstrahlung heating source, and solving for the steady-state distribution function, has been shown to further reduce κ. The accuracy of a simple analytic formula previously derived for κ_{IB} has been verified for up to $k\lambda_{ei} \sim 10^{-2}$.

ACKNOWLEDGMENT

The author acknowledges many useful discussions with Robert W. Short, Albert Simon, and Mark D. Tracy. This work was supported by the U.S. Department of Energy Office of Inertial Confinement Fusion under Cooperative Agreement No. DE-FC03-92SF19460, the University of Rochester, and the New York State Energy Research and Development Authority. The support of DOE does not constitute an endorsement by DOE of the views expressed in this article.

APPENDIX: THE ELECTRON-ELECTRON COLLISION OPERATOR

The isotropic and anisotropic parts of the collision operator are given by[2,10]

$$C_{ee}^{l}(f_0, f_l) = \nu_{ee} v \frac{\partial}{\partial v}\left[f_l I_0^0 + \frac{v}{3}\frac{\partial f_l}{\partial v}\left(I_2^0 + J_{-1}^0\right)\right]$$

and

$$C_{ee}^{a}(f_0, f_l)$$

$$= \nu_{ee}\left\{ 4\pi v^3 f_l f_0 + \frac{l(l+1)}{6} f_l\left(-3I_0^0 + I_2^0 - 2J_{-1}^0\right)\right.$$

$$+ \frac{v^2}{2(2l+1)}\frac{\partial^2 f_0}{\partial v^2}\left[\frac{(l+2)(l+1)}{2l+3}\left(I_{l+2}^l + J_{-1-l}^l\right)\right.$$

$$\left. - \frac{l(l-1)}{2l-1}\left(I_l^l + J_{1-l}^l\right)\right]$$

$$\left. + \frac{v}{2(2l+1)}\frac{\partial f_0}{\partial v}\left[\frac{(l+1)(l+2)}{(2l+3)} I_{l+2}^l - \frac{\left(l^2-l-4\right)}{(2l+3)} J_{1-l}^l \right.\right.$$

$$\left.\left. + \frac{\left(l^2+3l-2\right)}{(2l-1)} + \frac{l(l-1)}{(2l-1)} J_{1-l}^l\right]\right\},$$

where

$$I_m^n = \frac{4\pi}{v^m}\int_0^v f_n w^{2+m} dw, \quad J_m^n = \frac{4\pi}{v^m}\int_v^\infty f_n w^{2+m} dw$$

and $\nu_{ee}(v) = 4\pi N_e \left(e^2/m_e\right)^2 \ln\Lambda / v^3$ is the velocity-dependent e-e collision frequency. Here we note that $C_{ee}^{a}(f_0, f_0) = C_{ee}^{a}(f_0, f_0)$.

REFERENCES

1. E. M. Epperlein, R. W. Short, and A. Simon, Phys. Rev. Lett. **69**, 1765 (1992).
2. M. N. Rosenbluth, W. M. MacDonald, and D. L. Judd, Phys. Rev. **107**, 1 (1957).
3. C. J. Randall, Phys. Fluids **25**, 2231 (1982).
4. M. D. Tracy, E. A. Williams, K. G. Estabrook, J. S. DeGroot, and S. M. Cameron, Phys. Fluids B **5**, 1430 (1993).
5. L. Spitzer, Jr. and R. Härm, Phys. Rev. **89**, 977 (1953).
6. E. M. Epperlein and R. W. Short, Phys. Fluids B **3**, 3092 (1991).
7. G. W. Hammett and F. W. Perkins, Phys. Rev. Lett. **64**, 3019 (1990).
8. Z. Chang and J. D. Callen, Phys. Fluids B **4**, 1167 (1992); Phys. Fluids B **4**, 1182 (1992).
9. E. M. Epperlein, Phys. Rev. Lett. **65**, 2145 (1990); E. M. Epperlein and R. W. Short, Phys. Fluids B **4**, 2211 (1992).
10. I. P. Shkarofsky, T. W. Johnston, and M. A. Bachynski, *The Particle Kinetics of Plasmas* (Addison-Wesley, Reading, MA, 1966); T. W. Johnston, J. Math. Phys. **7**, 1453 (1966).
11. E. M. Epperlein, *Laser and Particle Beams* **12**, 257 (1994).
12. J. S. Chang and G. Cooper, J. Comput. Phys. **6**, 1 (1970).
13. R. J. Mason, J. Comput. Phys. **41**, 233 (1981).
14. A. R. Bell, Phys. Fluids **26**, 279 (1983).
15. R. W. Short and E. M. Epperlein, Phys. Rev. Lett. **68**, 3307 (1992); H. A. Rose and D. F. DuBois, Phys. Fluids B **4**, 1394 (1992); E. M. Epperlein and R. W. Short, Phys. Fluids B **4**, 4190 (1992); H. A. Rose and D. F. DuBois, Phys. Fluids B **4**, 4192 (1992).
16. A. B. Langdon, Phys. Rev. Lett. **44**, 575 (1980).

Particle-in-Cell Code Simulations of the Interaction of Gaussian Ultrashort Laser Pulses with Targets of Varying Initial Scale Lengths

Introduction

Since the advent of ultrashort laser pulses[1] there has been interest in the interaction of such pulses with solid targets. Several new modes of laser-plasma interaction at high intensities ($I\lambda^2 > 10^{16}$ W/cm^2 μm^2) have been identified, the most important being "vacuum heating,"[2] which dominates over resonance absorption when scale lengths are very short. These new absorption mechanisms, as well as nonlinear resonance absorption (wave breaking), are usually studied with a PIC (particle-in-cell) code. In one series of published results from PIC simulations, the interaction of p-polarized light with a plasma over a wide range of irradiances and scale lengths is described.[3] The range covered in these simulations included the transition from resonance absorption to vacuum heating. The simulations were carried out for a constant pulse, and few details were provided on the behavior of the fields and of the plasma. Other published results of PIC simulations[4] have concentrated on the effect of the radiation pressure on the motion of the ions at intensities in excess of 10^{18} W/cm^2 μm^2. Above this intensity the interaction enters another regime in which relativistic effects become important. We will not deal with the relativistic regime in this article. Incidentally, Vlasov codes have also recently been developed to study these nonlinear absorption mechanisms.[5]

Here, we present simulations in which a 100-fs Gaussian pulse interacts with preformed plasmas of varying scale lengths. These calculations simulate many of the actual experimental conditions in which laser pulses are preceded by either a long ASE pulse or a pedestal due to imperfect pulse expansion and recompression in chirp-pulsed amplification schemes. These simulations, carried out at an irradiance of 10^{16} W/cm^2 μm^2, near the irradiances reached in many experiments, include ion motion. A set of simulations was carried out with electron-ion collisions included. We find that observables like the absorption fraction, the fast-electron and fast-ion energy, and the production of harmonics depend strongly on the scale length of the initial profile.

The calculations were carried out with the 1 1/2-D relativistic PIC code *EUTERPE*.[6] Electron scattering due to collisions with the ions is included using a Monte Carlo rotator at the end of each time step.[7] To treat p-polarized oblique incidence, simulations are done by transforming to a reference frame moving in the transverse direction with velocity $v_d = c \sin\theta$, where θ is the angle of incidence.[3] This method suffers from two limitations: First, it does not model rippling of the critical surface, which becomes significant above 10^{18} W/cm^2 μm^2 and leads to a more complex angular distribution of the incident laser light. Second, at large angles, the maximum density, which transforms as $n_c/n_c = \gamma^{-3}(n_c/n_c)$, where

$$\gamma = \left[1 - \left(\frac{v_d}{c}\right)^2\right]^{-1/2} = \sec\theta,$$

becomes very large, which forces the time step to be very small and the number of particles to be large in order to obtain reasonable results. Most of the runs were done with 50,000 particles and with a mesh size of 500–1000 grid points. The absorption fraction, defined as the internal energy in the plasma divided by the cumulative input energy, is calculated in two ways: In the first way, the internal energy in the plasma is obtained as the sum of the kinetic energy over all the particles minus the initial internal energy of the plasma. In the second way, the internal energy is calculated by subtracting the electromagnetic energy in the box from the time-integrated Poynting vector at the left (input) boundary. Ideally, these two methods should yield the same absorption fraction.

Transition from Resonance Absorption to Vacuum Heating

In vacuum heating,[2] the longitudinal electric field does not penetrate into the plasma because of the steep density gradient but reaches its maximum value in the vacuum near the plasma

boundary. When electrons penetrate into the vacuum with the right timing, they are accelerated outward by the large longitudinal electric field. They are then turned around by the oscillating field and the electrostatic potential and penetrate into the solid with velocity $v = v_{osc}$ where they deposit their energy. Vacuum heating becomes the dominant absorption mechanism when the oscillatory orbit of the electrons in the laser field becomes large compared to the scale length. This can occur for either very steep density gradient or very large laser intensity.

We will discuss the transition from resonance absorption to vacuum heating for the nonrelativistic intensity regime, $I\lambda^2 < 10^{18}$ W/cm^2 μm^2. We are especially interested in finding "observables," experimental and numerical, that lead to the definition of the regime. Experimental observables include the absorption fraction, the fast electron spectrum (deduced from hard x rays, K_α emission, and electron spectrometry), and the harmonic emission. Numerical observables include the experimental observables, the electron phase space, the electron trajectories, and the longitudinal electric field profile. Velocities are normalized to the velocity of light, positions to c/ω_0, and time to ω_0^{-1}, where ω_0 is the laser frequency.

The difference between resonance absorption and vacuum heating can be readily seen by plotting the electron trajectories (orbits) for two extreme scale lengths: $L/\lambda = 1$ and $L/\lambda = 0.001$, where λ is the laser wavelength. In Fig. 58.15(a), in which are plotted the trajectories of selected electrons (every 1000th) near the critical surface for a constant irradiance of 5×10^{16} W/cm^2 μm^2, an incident angle of 30°, and $L/\lambda = 1$, we observe the growth of the electron plasma wave until wave breaking starts at about 60 ω_0^{-1}. Wave breaking tends to occur in a random fashion in the resonance region when electron orbits cross. The electron trajectories for vacuum heating, shown in Fig. 58.15(b), show a very different behavior. In this case the conditions are a constant irradiance of 10^{18} W/cm^2 μm^2, an incident angle of 30°, and $L/\lambda = 0.001$. Starting with the first period of the laser, and for each successive period ($T = 2\pi$), electrons are pulled out into the vacuum and returned to the solid with velocities near v_{osc}. Interesting structures can also be observed: the successive long and short orbits into the vacuum every two laser periods and the smaller orbits with a "period" of one-half a laser period.

The difference in the longitudinal electric field profile for the two cases is shown in Fig. 58.16 along with the electron density profile. The electric field shown here, and in all subsequent graphs, is the oscillating field averaged over a period of the laser field normalized to the incident longitudinal electric field. In the resonance absorption case [Fig. 58.16(a)] the resonant field at the critical surface is large compared to the incident field and creates a "hole" in the density profile due to the ponderomotive force. In the vacuum heating case,

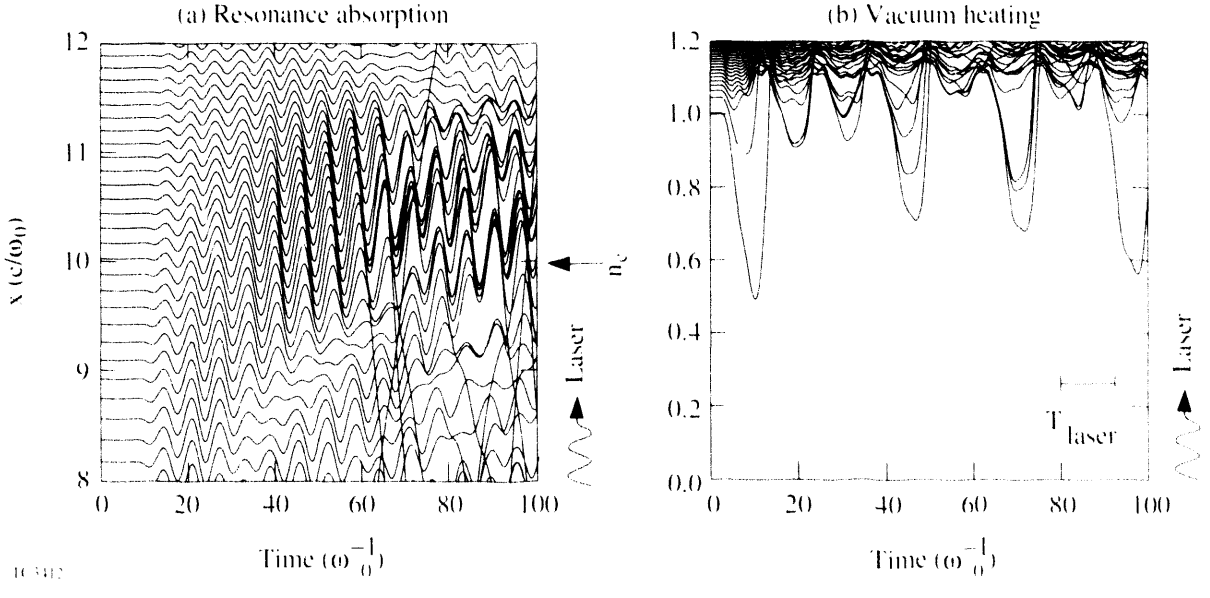

Figure 58.15
Electron trajectories for the two regimes: (a) resonance absorption; (b) vacuum heating. In both cases the laser is incident from the bottom. Only a sample of all the electrons is shown. Conditions are (a) $I\lambda^2 = 10^{16}$ W/cm^2 μm^2 and p-polarized light incident at 30°, $L/\lambda = 1.0$ linear, cold plasma without collisions, and stationary ions; (b) $I\lambda^2 = 10^{18}$ W/cm^2 μm^2 and p polarized light incident at 30°, $L/\lambda = 0.001$ linear, cold plasma without collisions, and stationary ions.

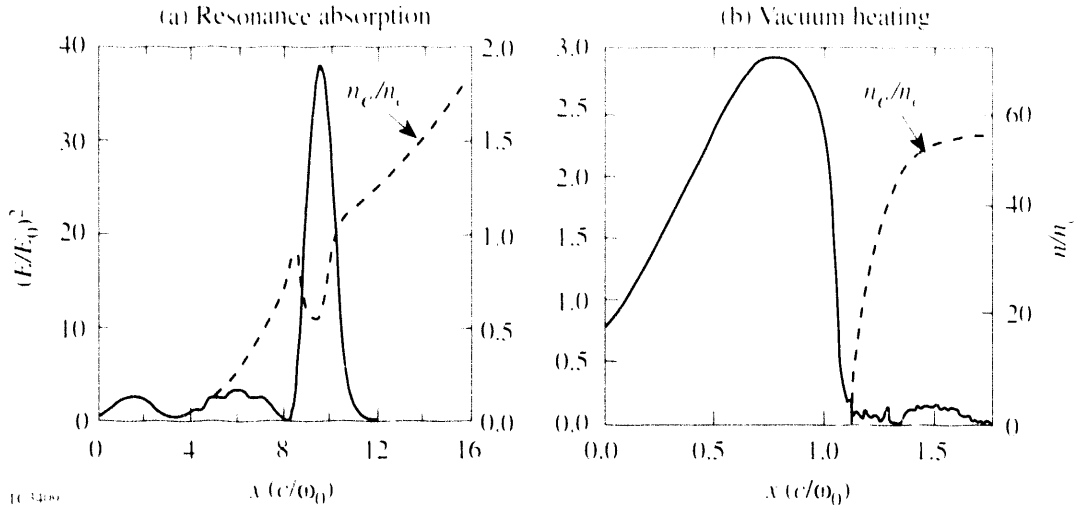

Figure 58.16
Period-averaged oscillating longitudinal electric field and electron density profile for the two cases in Fig. 58.15. The electric field is normalized to the incident longitudinal field.

the field does not penetrate into the plasma and displays the swelling expected near the surface of a conductor. The peak value of the field in the vacuum heating case is much lower than that in the resonance absorption case. As will be discussed below, this leads to much lower hot-electron energies for the same irradiance.

The transition from one regime to the other is complex, yet it is necessary to understand the changes that are occurring during this transition because many experiments are carried out under these conditions. The most straightforward way to study this transition is to vary the ion density profile, holding the irradiance fixed. In this way we avoid the added complexity that would arise from changes in such quantities as the absorption fraction and the electron maximum energy due to changes in the irradiance.

Interaction with Gaussian Pulses

Most, if not all, PIC simulations are carried out with a temporal irradiance characterized by a rising portion followed by a constant intensity up to some time limited by either computer time, by "numerical heating" due to the statistical nature of the problem, or by numerical instabilities in the code. These irradiation conditions approximate reasonably well those at the peak of pulses with pulse duration larger than tens of picoseconds; this may not be the case in ultrashort pulse laser interactions. With the advent of lasers with pulse duration of about 100 fs, it is now possible with present day computing power to simulate the interaction of an entire pulse with a plasma. Of course, PIC codes cannot simulate realistically high-density plasma in which electrons are described by Thomas-Fermi statistics and ions by short-range interaction. Atomic physics processes such as ionization and radiation are not included in PIC codes, although some effort is being made to include ionization.[7]

In this section we present the results of the study of the interaction of a 100-fs Gaussian pulse (full-width at half-maximum) with plasmas of varying initial electron and ion density scale lengths. The initial scale length is varied in order to simulate many present day experiments in which a prepulse creates a plasma in front of the solid surface before the arrival of the main pulse. Simulations with a Gaussian pulse can model more realistically than constant pulses the production of fast ions and the effect of the temporal variation of the irradiance on the absorption fraction, on the production of fast electrons and ions and of harmonics, and on the distortion of the density profiles due to the ponderomotive force. The simulations include ion motion and, in some cases, electron-ion collisions. In the collisionless case the ions have a charge of unity and a mass of $3600\,m_e$. In the collisional case, the simulations are specialized to fully ionized aluminum ($Z = 13$) and a laser wavelength of 620 nm [the wavelength of a CPM (chirped pulse modulated) dye laser]. The irradiance is started and stopped at 1% of the peak power, taken to be 10^{16} W/cm^2 μm^2. The simulations were carried out at a 30° angle of incidence and included 50,000 particles.

Four linear density profiles were used: $L/\lambda = 0.001$, 0.01, 0.1, 1.0. The following experimental diagnostics are displayed

for these four cases: the energy spectrum of the electrons that entered the solid (those reaching the high-density boundary), the energy spectrum of all the ions at the end of the pulse, and the cumulative absorption fraction as a function of time. The effect of the initial density profile on the electric field near or in the plasma and on the ion density profile at the end of the pulse will also be discussed.

We first discuss changes in the longitudinal electric field profile due to variations in the initial scale length, as displayed in Fig. 58.17. At the two extremes, $L/\lambda = 0.001$ and $L/\lambda = 1.0$, the electric field shows the behavior expected from vacuum heating and resonant absorption respectively. As the scale length is decreased from $L/\lambda = 1.0$, we observe the gradual change from the the single resonant peak to the wave swelling outside the steep plasma profile. Conditions at $L/\lambda = 0.1$ are complex: the resonant field is split and a resonance at $2\,n_c$ can be observed. At that scale length the resonant peak occurs near the edge of the plasma: the width of the resonant region is equal to or larger than the scale length and the orbits of the thermal electrons in that region can extend into the vacuum. As the gradient steepens to $L/\lambda = 0.01$, some field swelling in the vacuum interfaces can now be observed along with a resonance peak at the edge of the plasma and small multi-resonances in the overdense plasma. At the steepest gradient the field is confined to the vacuum and all resonances have disappeared.

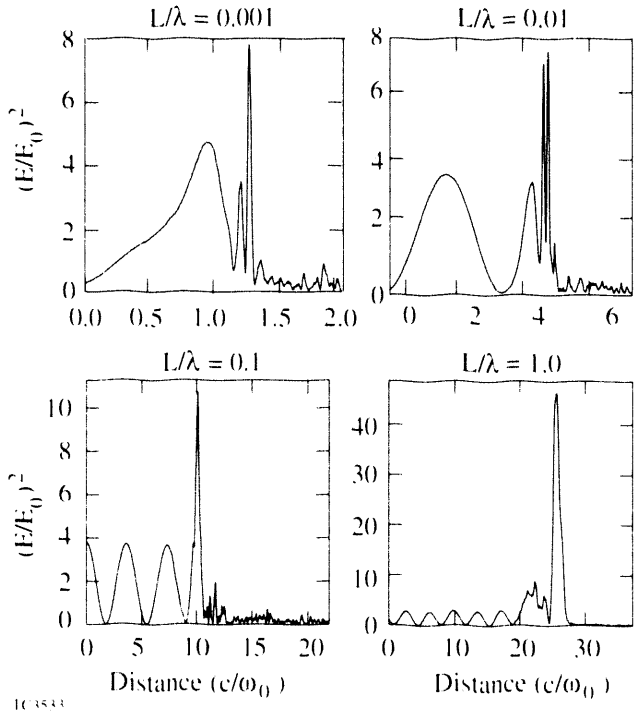

Figure 58.17
Period-averaged oscillating longitudinal electric field in the transition from resonance absorption to vacuum heating at the peak of the Gaussian pulse ($400\ \omega_0^{-1}$). Laser conditions are $I\lambda^2 = 10^{16}$ W/cm^2 μm^2 and p-polarized light incident at 30°; the initial density profiles are linear, and collisions are not included.

The effect of the ponderomotive force due to the electromagnetic field on the ion density profile is shown in Fig. 58.18 at a time near the end of the pulse. The dashed line indicates the initial density profile. In the shortest scale length case, $L/\lambda = 0.001$, the pressure from the reflected laser beam is not large enough to move back the density profile during the pulse duration. Ions below the critical surface have expanded into the vacuum due to two effects: the pressure of the heated thermal electrons that have expanded into the vacuum and the electrostatic potential from electrons pulled into the vacuum by the vacuum heating absorption process. At such a short scale length the density gradient at the critical surface is not steepened, but lengthened due to the expansion. The medium-scale-length cases, $L/\lambda = 0.01$ and 0.1, show a slight deformation of the ion density profile. This effect is caused by the ponderomotive pressure of the resonant field situated at the edge of the plasma, not by the pressure of the reflected

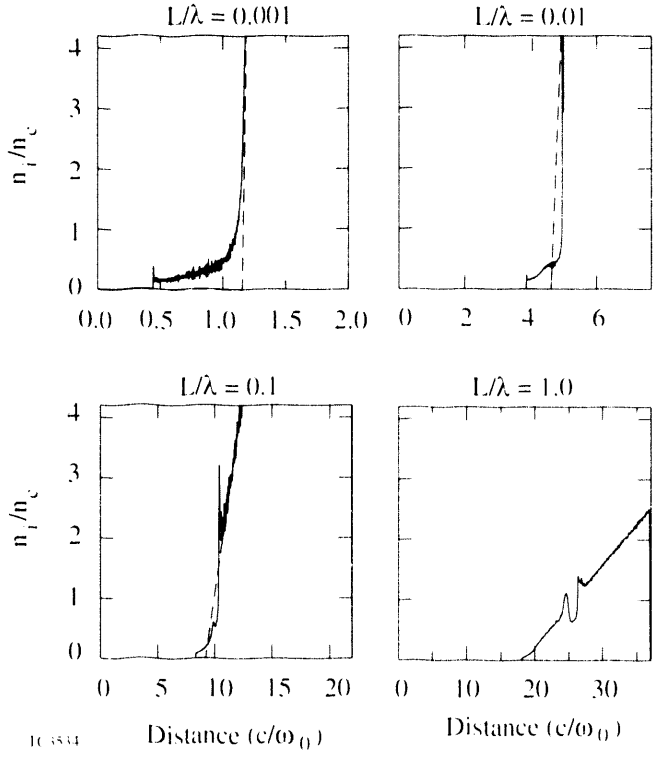

Figure 58.18
Ion density profile at the end of the pulse for the conditions in Fig. 58.17. The dashed curve is the initial density profile.

light. At the peak of the pulse the profile steepening is slight and should not affect the resonant absorption process. At the end of the pulse the profile for the case $L/\lambda = 0.1$ was steepened to $L/\lambda = 0.025$. Profile modification is more evident in the long-scale-length case because the resonant field is larger than at shorter scale lengths. At the peak of the pulse a small plateau is created, and the local scale length at the critical surface is about 0.5 λ. By the end of the pulse a hole about 0.5 n_c deep has been dug into the ion density profile by the resonant electric field.

One of observables strongly affected by variations in the scale length is the harmonic emission, plotted in Fig. 58.19. For the case $L/\lambda = 1$ we observe the harmonic emission expected from resonance absorption: an exponentially decreasing series of harmonics. For $L/\lambda = 0.1$, the harmonic series is very noisy and is cut off above $n = 2$. The case $L/\lambda = 0.01$ is very interesting in that the emission occurs at half-harmonics: 3/2 and 5/2; we have found no explanation for this behavior. At the steepest gradient, very weak harmonics are observed at $n = 3$ and 4, but none at $n = 2$. The low harmonic level is probably due to the low absorption efficiency of the vacuum heating mechanism at this intensity. At higher intensities the entire range of harmonics can be observed.

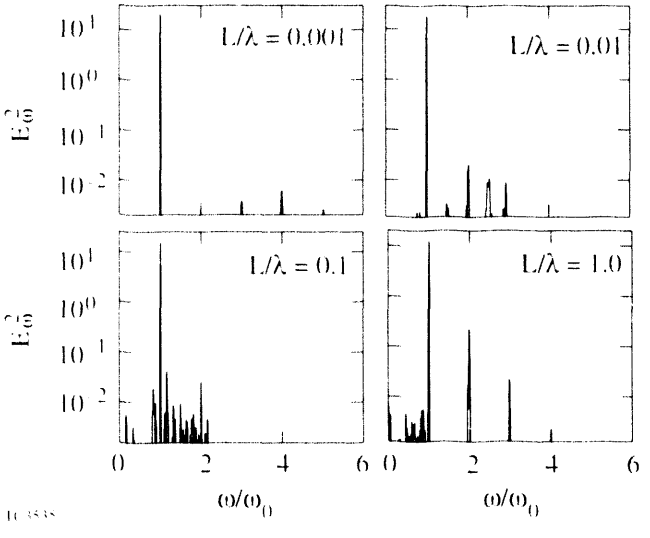

Figure 58.19
Power spectrum of the reflected light for the conditions in Fig. 58.17. Note the half-harmonics produced in the case $L/\lambda = 0.01$.

The spectra of the electrons that have left the computational box at the high-density end for the four cases are shown in Fig. 58.20. These are electrons that create observable bremsstrahlung hard x rays and K_α emission from the solid target. The maximum energy of the electrons decreases with scale length, in agreement with the decreasing peak values of the electric field observed in Fig. 58.17. It is not straightforward to obtain a temperature from the spectra because the electron distribution is not Maxwellian, especially for the short-scale-length cases. One reason is that vacuum heating tends to produce beams of electrons rather than a distribution; the other reason is that the spectra are cumulative over a range of intensity, therefore over a range of temperatures. For $L/\lambda = 0.1$ and $L/\lambda = 1.0$, the distributions are nearly Maxwellian with temperatures of 22 keV and 35 keV respectively. For $L/\lambda = 0.001$ and $L/\lambda = 0.01$ the slopes of the main body of the distribution yield 6 keV and 10 keV, respectively.

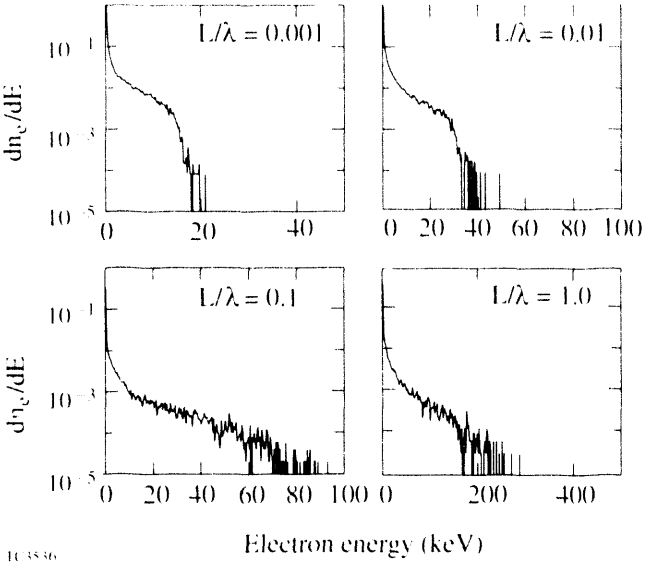

Figure 58.20
Cumulative distribution of the electrons entering the solid (leaving at the right-hand-side boundary) for the conditions in Fig. 58.17.

The ions spectra for the four cases, another experimental diagnostic, are shown in Fig. 58.21. The spectra contain the main body of the ion distribution at low energy and the distribution of the fast ions accelerated by the hot electrons. From $L/\lambda = 0.001$ to $L/\lambda = 0.01$, as expected the peak ion energy increases with scale length as did the hot-electron distribution. The increase is small between $L/\lambda = 0.01$ and $L/\lambda = 0.1$, and the peak energy is actually lower for $L/\lambda = 1$ than for $L/\lambda = 0.1$, despite the fact that the fast-electron energy increases sharply in that range of scale length. Two effects may be responsible for the scaling of the fastest ion energy: not enough time to accelerate the ions to their maximum velocity because of the short pulse duration; the

accelerating electrostatic potential, given roughly by T_h/L, where T_h is the hot-electron temperature, is lower in the long-scale-length cases.

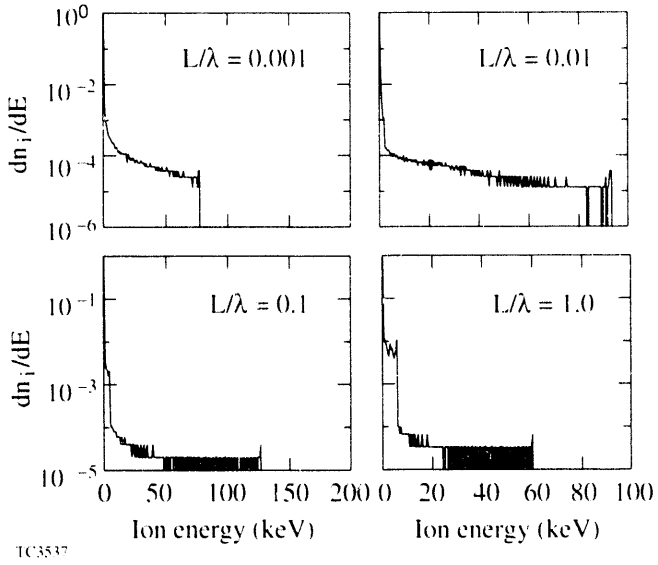

Figure 58.21
Total ion spectrum at the end of the pulse for the cases in Fig. 58.17. The energetic ions are the fast ions accelerated into the vacuum.

The cumulative absorption fraction as a function of time is plotted in Fig. 58.22 for the four cases. The peak of the pulse is at 400 ω_0^{-1}. In these graphs, the absorption fraction is defined as the time-integrated Poynting vector at the vacuum boundary minus the electromagnetic energy in the computing box, divided by the time-integrated input laser energy at the vacuum boundary. The "hash" in the line is due to the time-varying value of the electromagnetic energy in the box. The final absorption fraction is low at the short scale lengths (about 10%) and increases with scale length as the resonance absorption regime becomes dominant. Adding collisions ($Z = 13$) has little effect on these results: the absorption fraction is slightly larger early in the pulse but is slightly lower near the peak of the pulse because collisions decrease slightly the resonant field. At this intensity vacuum heating is a very inefficient absorption process.

The results of the simulations are summarized in Fig. 58.23 where the absorption fraction and the maximum electron and ion energy are plotted as a function of the scale length. The absorption remains very low for $L/\lambda < 0.01$ and increases for increasing scale length to the large values associated with resonance absorption. The electron peak energy scales roughly as $(L/\lambda)^{0.4}$, except through the vacuum heating range where it would be expected to depend only on the laser intensity through v_{osc}. These results, and the behavior of the longitudinal electric field, point to the existence of three regions as discussed in Ref. 3: the vacuum heating region below $L/\lambda = 0.01$; a region in which the oscillatory orbit of the electrons is about the distance between the critical surface and the vacuum/plasma interface; and a resonance absorption region above $L/\lambda = 0.03$, where the resonance occurs inside the plasma and the oscillating electrons never reach the vacuum. The second region is very complex. The resonance structure of the electric field splits for some values of L/λ, while harmonic resonances appear in the overdense plasma. A detailed study of the electron orbits shows that the electrons near the plasma/vacuum interface can be accelerated into the vacuum without undergoing wave breaking, while electrons slightly deeper in the plasma, but still in the resonance region, are accelerated by wave breaking. The different regimes can be seen as plateaus in the absorption fraction separated by transition regions. Similar results, but slightly shifted to higher scale lengths, were obtained for an irradiance of 10^{17} W/cm^2 μm^2: The transition to vacuum heating occurs now for $L/\lambda \approx 0.03$ as compared to $L/\lambda \approx 0.01$ for the lower irradiance case.

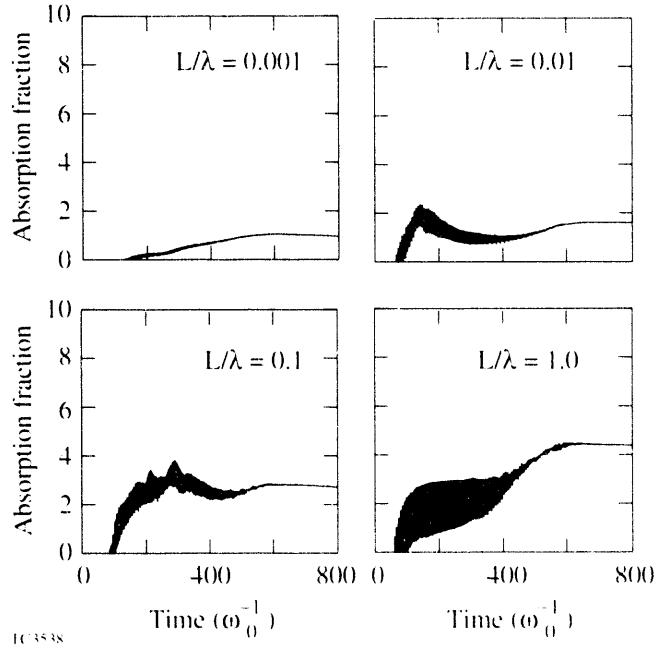

Figure 58.22
Cumulative absorption fractions for the conditions in Fig. 58.17. The "hash" in the line is due to the time-varying value of the electromagnetic energy in the box.

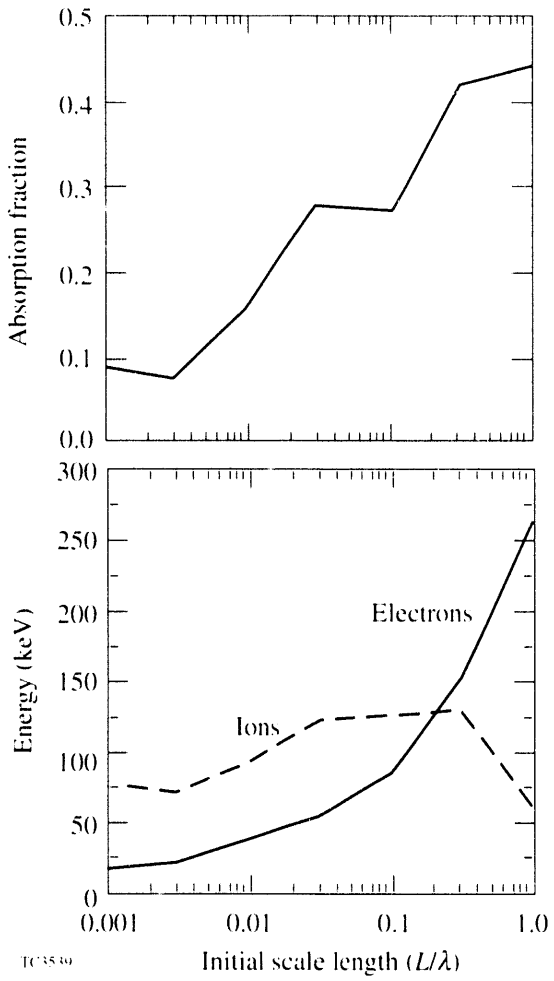

Figure 58.23
Summary of the results from the simulations of the transition from vacuum heating to resonant absorption for conditions in Fig. 58.17.

Conclusions

The transition from the resonance absorption regime to the vacuum heating regime in short-pulse laser-plasma interaction has been studied using the 1 1/2-D PIC code *EUTERPE*. Laser conditions were a 100-fs Gaussian pulse with $I\lambda^2 = 10^{16}$ W/cm^2 μm^2 and p-polarized light incident at 30°. The transition was observed by varying the density scale length over the range $L/\lambda = 0.001$ to 1.0.

We observed that vacuum heating occurred for $L/\lambda < 0.01$. This is a very steep scale length that can be obtained only with very short pulses (about 100 fs) in the absence of any prepulse energy on the target. For $0.3 > L/\lambda > 0.01$ the resonant region remains at the edge of the plasma. In this transition regime the behavior of the resonant field becomes complex as the orbits of the resonant electron extend into the vacuum. For $L/\lambda > 0.3$, the resonance region moves into the plasma, and the "classic" resonance absorption regime is recovered. The peak resonant longitudinal electric field, the peak electron energy, and the absorption fraction increase with increasing scale length. Harmonic production above the second harmonic disappears in the transition regime. Adding collisions with $Z = 13$ has little effect on these results.

ACKNOWLEDGMENT

This work was supported by the Laboratoire pour l'Utilisation des Lasers Intenses and the Laboratoire de Physique des Milieux Ionisés, Ecole Polytechnique, Palaiseau, France and by the Centre d'Etude de Limeil-Valenton du Commissariat à l'Energie Atomique, Villeneuve-St-Georges, France. This work was also supported by the U.S. Department of Energy Office of Inertial Confinement Fusion under Cooperative Agreement No. DE-FC03-92SF19460, the University of Rochester, and the New York State Energy Research and Development Authority. The support of DOE does not constitute an endorsement by DOE of the views expressed in this article.

REFERENCES

1. P. Main and G. Mourou, Opt. Lett. **13**, 467 (1988).
2. F. Brunel, Phys. Rev. Lett. **59**, 52 (1987).
3. P. Gibbon and A. R. Bell, Phys. Rev. Lett. **68**, 1535 (1992).
4. For example, J. Denavit, Phys. Rev. Lett. **69**, 3052 (1992).
5. H. Rhul and P. Mulser, presented at the *23rd Annual Anomalous Absorption Conference*, Wintergreen, VA, 21–25 June 1993, paper 2O3.
6. G. Bonnaud and G. Reisse, Nucl. Fusion **26**, 633 (1986).
7. J. M. Wallace *et al.*, Phys. Fluids **3**, 2337 (1991).

Characterization of Thick Cryogenic Fuel Layers: Compensation for the Lens Effect Using Convergent Beam Interferometry

Historically, the fuel content and fuel-layer uniformity of cryogenic targets have been characterized interferometrically using plane-wave illumination.[1–6] This technique has the sensitivity necessary to detect a deviation from sphericity of the fuel layer's inside surface as small as a few percent of its total thickness. In the past at LLE, the targets examined were typically 250-μm-diam glass capsules with wall thicknesses of a few micrometers that were filled with enough fuel to produce a condensed fuel layer less than 10 μm in thickness. Future OMEGA Upgrade cryogenic targets will consist of polymer capsules several tens of micrometers thick with diameters ranging from 700–1100 μm. These will be filled with condensed D_2 or DT fuel with a thickness of up to 100 μm.

A capsule with a thick cryogenic layer condensed on its interior behaves as a strong negative lens, which has several adverse effects on its interferogram when created with plane-wave illumination. Computer simulations of typical interferograms are shown in Fig. 58.24. The highly divergent and spherically aberrated wavefront created by the target cannot be effectively collected and imaged using optics with convenient numerical apertures, resulting in loss of information near the perimeter of the target's image. In addition, when this highly curved wavefront interferes with a planar reference wavefront, an interferogram with a fringe spatial frequency that increases radially to very high values near the perimeter of the target's image is produced. Since the phase, and therefore

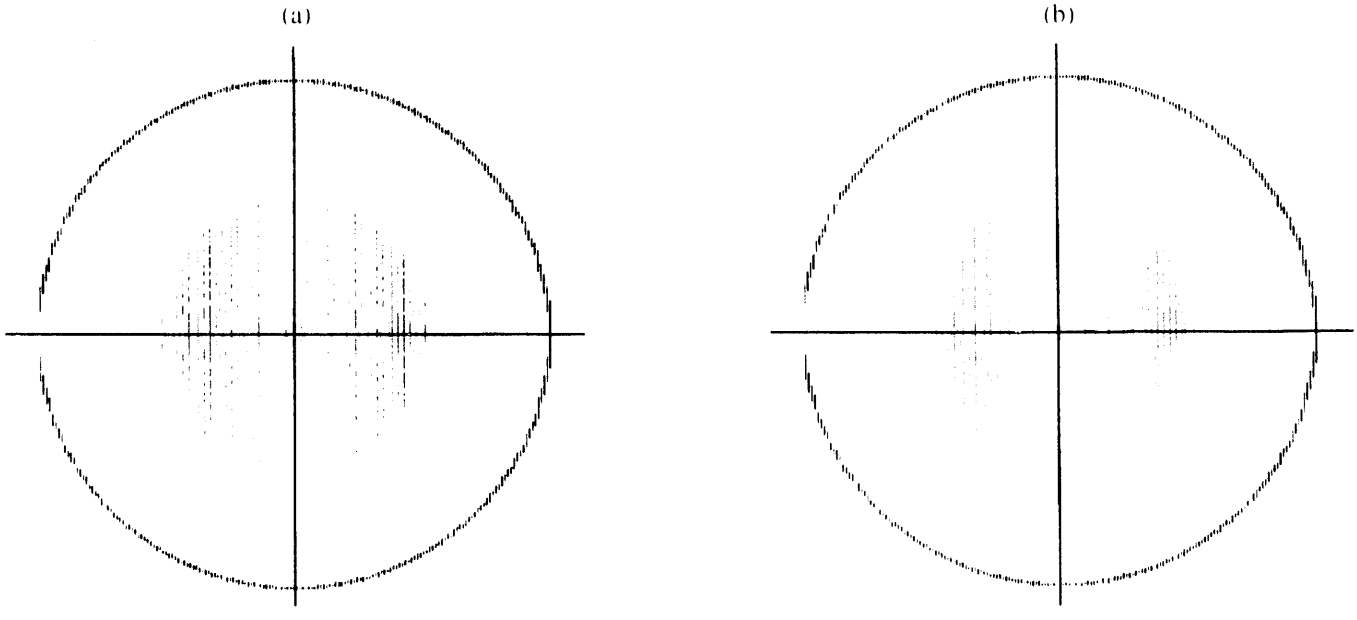

Figure 58.24

Computer-generated interferograms of a 10-μm-thick polystyrene capsule with a diameter of 1120 μm that contains 100 μm of condensed fuel. These were created with the assumptions that both the object and reference beams consisted of planar wavefronts with a 514-nm wavelength, and f/6 optics were used to image the target. All of the surfaces in (a) are perfectly concentric with one another, whereas (b) displays a 5% fuel nonconcentricity, i.e., the center of the spherical inner surface of the condensed fuel layer has been displaced to the right in the figure by 5% of its total thickness. Obviously, a 5% nonconcentricity can be easily detected, but higher-order nonuniformities are much more difficult to detect due to the very high fringe frequency. In addition, information regarding the state of the fuel near the perimeter of the target's image has been lost due to refraction of the object beam outside of the imaging optics' finite collection aperture.

thickness, resolution resulting from the analysis of an interferogram is inversely proportional to the number of detector elements per fringe, the phase sensitivity is reduced dramatically when the fringe frequency approaches the Nyquist limit of the detector. As the fringe frequency nears the frequency of pixels in the CCD array, aliasing occurs and the fringes become unresolved. Evidence of this is the Moiré patterns exhibited in the theoretical interferograms of Fig. 58.24, where the fringes are beating with their array locations instead of CCD detector elements.

There are several requirements of a cryogenic-target interferometer that are applicable to OMEGA Upgrade target experiments. First, it should be sensitive to high-order fuel nonuniformities, not only nonconcentricity of the inner and outer fuel-layer surfaces. It should also be suitable for a wide range of capsule/fuel-layer dimensions. It should be simple to implement, optically stable, and amenable to computerized wavefront-measuring techniques (i.e., phase-shifting interferometry) to obtain the most accurate quantitative information possible. Finally, it should be compact and versatile enough to be adapted to *in-situ* fuel-layer characterization both in laboratory and target chamber experiments.

To realize these requirements, an interferometer has been developed that illuminates the target with a wavefront that is convergent to a point near the target's rear focal point, thus causing a nearly planar wavefront to emerge from it. A comparison between the emergent wavefront with plane-wave and convergent-beam illumination is shown in Fig. 58.25. With convergent-beam illumination, when the transmitted wavefront interferes with a planar reference wavefront, a low-fringe-frequency interferogram of the target is produced that can be analyzed with a better phase resolution.

When imaged on axis, the wavefront emerging from the target with plane-wave illumination departs from a plane with two major components: a diverging spherical element designated as x_1 in Fig. 58.26 and a spherical aberration contribution designated as x_2. In Fig. 58.26, f_{tgt} is the effective focal length of the target as measured from the capsule's equatorial plane (i.e., the y-axis), examples of which are given as a function of fuel-layer thickness for a 10-μm-thick polystyrene capsule in Fig. 58.27. For $(r/f_{tgt})^2 << 1$, where r is the inner radius of the condensed fuel layer, x_1 can be approximated as parabolic: $x_1 = \left(r^2/2f_{tgt}\right)y^2$, while x_2 depends on y to the fourth power as $x_2 = W_{040}y^4$. The optical system collects and images this transmitted wavefront and the capsule. Since the perimeter of the target's image is normally in focus in an interferogram, the emergent wavefront is imaged as if projected back into the equatorial plane of the target; hence y is the normalized pupil function and is given by the ratio of the distance from the center of the target's image to the inner radius of the fuel layer r. Therefore, if x_1 is eliminated by illuminating the target with a wavefront converging to a point behind it, a distance f_{tgt} away from its center, only the spherically aberrant component of the transmitted wavefront remains. This flattens the wavefront emerging from the target, with only the curvature due to the spherical aberration term left. By using convergent-beam illumination, not only is more light collected from regions near the perimeter of the target, but the interferogram consists of fewer rings that are concentrated near the perimeter of the target's image, decreasing the maximum fringe frequency to a value well below the Nyquist limit of the detector array.

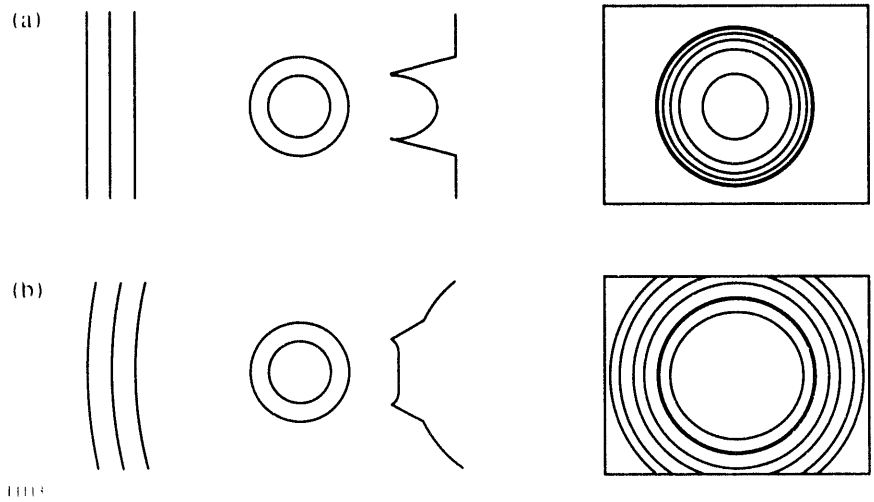

Figure 58.25
An illustration of the wavefront that emerges from a capsule filled with a thick condensed fuel layer when both plane-wave and convergent-beam illumination are used, along with hypothetical interferograms that are produced when the transmitted wavefront interferes with a planar reference wavefront. It is apparent in (a) that a relatively small portion of the highly divergent wavefront can be effectively collected and imaged. However, in (b), not only is the transmitted wavefront flattened, but the light surrounding the capsule can also be readily collected and imaged.

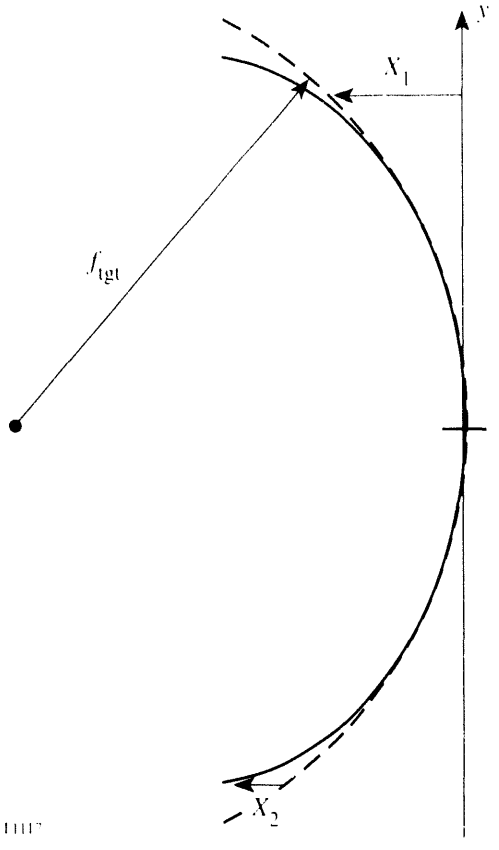

Figure 58.26
An illustration of the wavefront emerging from a cryogenic target when it is illuminated with a planar wavefront. The emergent wavefront is normally imaged as if projected back into the equatorial plane of the target, making the y-axis lie along a major diameter of the spherical inner surface of the condensed fuel layer. The transmitted wavefront contains two major components: a diverging spherical constituent designated as x_1 and a spherical aberration term designated as x_2, and f_{tgt} is the effective focal length of the target.

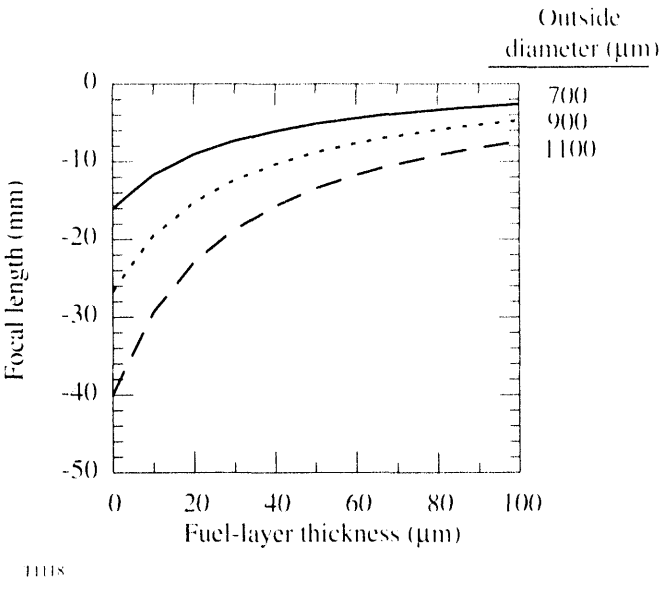

Figure 58.27
The effective focal length f_{tgt} of cryogenic targets as a function of condensed fuel-layer thickness. A 10-μm-thick polystyrene capsule was assumed for the various outside diameters shown. Paraxial rays were traced through hypothetical targets to find their focal lengths, which are measured from their equatorial plane.

The values for $r^2/2f_{tgt}$ and W_{040} in Fig. 58.28 were calculated by tracing paraxial rays through a hypothetical cryogenic target to find its focal length and applying third-order aberration theory to determine the spherical aberration component. The values shown are for the emerging wavefront projected back into the equatorial plane of the target and denote the maximum values these quantities take, i.e., for $y = 1$. The number of fringes present in an interferogram between the center of a target's image and a point along its radius can readily be determined from Fig. 58.28 by summing x_1 and x_2 for a given y and dividing by the wavelength of the light used to create it. For example, a 10-μm-thick polystyrene capsule with a diameter of 1100 μm containing 100 μm of condensed fuel would have 39 fringes between its center and the inside of the fuel layer when planar wavefronts with a 0.5-μm wavelength are utilized to create its interferogram. Eliminating the spherical component of the emerging wavefront by illuminating the same target with a beam of light converging to its focal point 6.8 μm behind it produces only 13 fringes, which are mainly concentrated toward the perimeter of the image. Hence, a greater sensitivity to nonconcentricities and higher-order nonuniformities in the fuel layer can be achieved.

The optical system used to create an interferogram of a cryogenic target with convergent-beam illumination is shown in Fig. 58.29. (The properties of the light sources and components of the initial beamsplitting system shown in Fig. 58.30 will be discussed in detail later since their use will become more apparent following a description of the imaging system.) The light is delivered to the interferometer using two single-mode optical fibers, one for the object arm and another for the reference arm. The optical fibers serve several purposes. They vibrationally and optically isolate the laser source from the structural and optical components of the interferometer. In addition, the optical fiber's flexibility makes relative placement of the light source and the interferometer unrestrictive. Transmitting only the lowest-order mode, the optical fibers also serve to spatially filter the light emitted by the laser source.

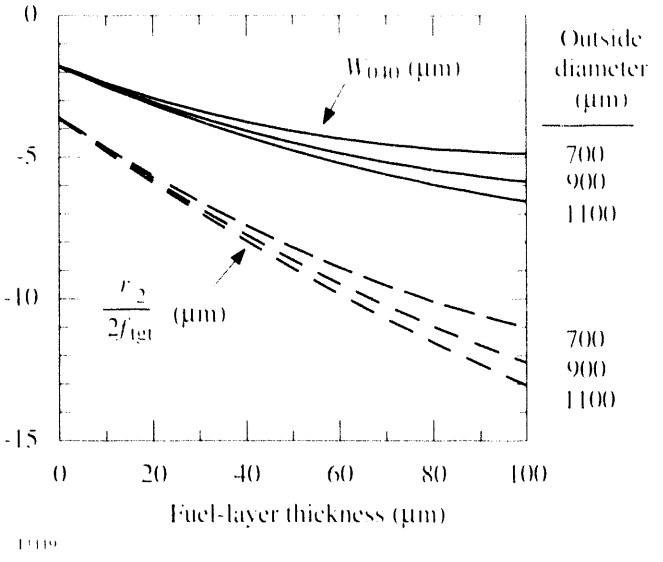

Figure 58.28
The values for $r^2/2f_{tgt}$ and W_{010} for cryogenic targets as a function of condensed fuel-layer thickness. Again a 10 μm-thick polystyrene capsule was assumed for the outside diameters shown. Third-order aberration theory was used to determine W_{010}. The values shown are for the emerging wavefront projected back into the equatorial plane of the target and denote the maximum values these quantities take, i.e., for $r = 1$.

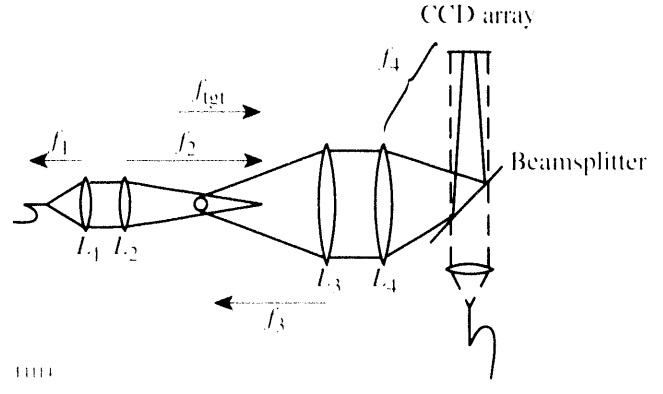

Figure 58.29
A schematic of the optical system used to create an interferogram of a cryogenic target with convergent-beam illumination. The optics that control the point of focus of the convergent beam and those that image the target are shown. The dotted line denotes the collimated reference beam.

The light emerging from the optical fiber in the object arm is first collimated with lens L_1 and is focused to a point with L_2. All lenses in the interferometer are achromatic doublets corrected for infinite conjugates. All imaging takes place close to the optical axis of the interferometer, so the use of these lenses minimizes spherical aberration. Since the light between L_1 and L_2 is collimated, only the position of L_2 is adjusted to locate the focus of the convergent beam at the rear focal point of the cryogenic target.

The target is imaged onto a CCD array by the optical relay system composed of lenses L_3 and L_4. The ratio of the focal lengths of these lenses, f_4/f_3, determines the magnification of the imaging system. In some instances, the working distance between the target and L_3 (i.e., f_3) is required to be large, such as the case of imaging in the OMEGA Upgrade target chamber. For large magnifications, the required value of f_4 may then exceed the physical dimensions of the space allotted to this target diagnostic. In this case, f_4 can be made equal to f_3, and a microscope objective lens can be used to further image the intermediate unity-magnification image of the target onto the CCD array.

The light emerging from the optical fiber in the reference arm of the interferometer is collimated, and the reference beam is combined with the object beam using a 50/50 beamsplitter. The partially reflective coating on the parallel-plate beamsplitter faces L_4 so that no aberration is introduced into the object beam by passage through a thick plate. Since the reference beam is collimated, its passage through the plate does not affect the planar reference wavefronts except to displace them laterally with respect to the optical axis of the collimating lens. The direction of propagation between the object and reference beams (i.e., the tilt) is controlled by rotating the reference beam's collimating lens about an axis perpendicular to its optical axis. Both the object and reference beams have a Gaussian, and therefore nonuniform, intensity profile upon emerging from the single-mode optical fiber. The centroid of the intensity distribution of the interferogram produced on the CCD array can also be positioned by translating the collimating lens in a direction perpendicular to its optical axis.

As the position of the focal point of L_2 is translated longitudinally with respect to the target's position, the irradiance of the object beam at the target (and its image) varies dramatically. The individual irradiances of the object and reference beams at the CCD array must be equal to produce interference fringes with the maximum possible contrast. Hence, to obtain high-contrast interferograms for a wide range of cryogenic target dimensions, the ratio of the power launched into the two fibers must be continuously variable. Referring to Fig. 58.30, this is accomplished using a polarizing beamsplitter in conjunction with linearly polarized laser light and a half-wave plate that can be rotated about its cylindrical axis. As the half-wave plate is rotated, the power ratio of the object beam to the reference beam varies continuously between 0 and 1.

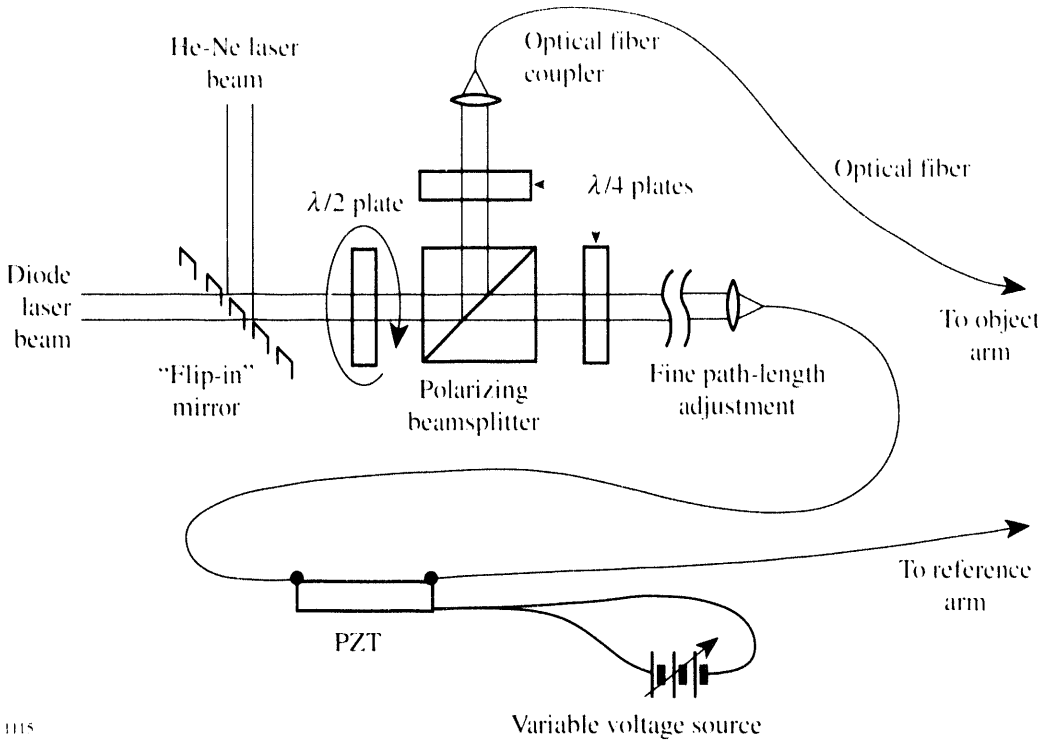

Figure 58.30
A schematic of the optical system that divides the source of radiation into the object and reference beams. Variable wavefront division is possible using the half-wave plate and the polarizing beamsplitter. Polarization-preserving fiber is unnecessary if quarter-wave plates are used to circularly polarize the light launched into the single-mode optical fibers, thereby reducing the detrimental effects that the variable bending conditions of the fiber have on the interferogram.

When linearly polarized light propagates through an optical fiber that is not polarization preserving, the polarization direction of the light emerging from the fiber depends on the bending conditions of the fiber between the source and its termination. The contrast of an interference pattern also depends on the relative angle between the polarization directions of the two beams that produce it. To stabilize the interferogram's contrast, quarter-wave plates are used to launch circularly polarized light (with the same handedness) into each fiber. Although some ellipticity is introduced into the light's polarization during propagation through the fiber, the contrast remains relatively constant as the fibers' bending conditions change.

An interferogram created with long-coherence-length light generally contains a significant amount of low-contrast noise due to interference between reflections from the various optical surfaces. To reduce this noise, a source of short-coherence-length light can be utilized. However, this makes the alignment and optical-path balance between the object and reference beams more critical. GaAlAs gain-guided laser diodes operate with numerous longitudinal modes resonating simultaneously, producing radiation with a bandwidth of several nanometers. This translates to a coherence length of only a few millimeters. To aid in alignment, the optical system is first aligned using a long-coherence-length source such as a He-Ne laser. When the maximum contrast of the interference fringes has been obtained by trimming the length of the optical fibers and adjusting the spacing between the polarizing beamsplitter and the optical-fiber coupler in the reference arm, the "flip-in" mirror in Fig. 58.30 can be removed and the laser diode becomes the light source. Fine path-length adjustment is accomplished by careful positioning of the optical-fiber coupler in the reference arm, which is mounted on a precision slide. A broadband polarizing beamsplitter and liquid-crystal wave plates that have an equal retardance for two wavelengths[7] are used so the contrast of the interferogram is not altered when the light sources are interchanged.

Phase sensitivities of the order of a few hundredths of a fringe can be achieved using phase-shifting techniques.[8–10] This involves sequentially acquiring multiple interferograms, each with a known phase offset between them caused by introducing a slight path-length change in one of the interferometer's arms. The phase of each point in the interferogram, modulo 2π, is then obtained by performing simple

mathematical operations on the set of interferograms. One advantage of phase-shifting methods is that the phase resolution depends primarily on the dynamic range of the CCD array (and the contrast of the interferogram) and, to a lesser degree, on the dimensions of individual pixels, as is the case with fringe-finding techniques.

An elegant method of introducing a controlled phase step into one of the interferometer's arms is to slightly elongate the optical fiber in that arm. This method introduces a path-length change alone and does not affect the tilt between the object and reference wavefronts, which can often be disturbed when an optical element such as a mirror or lens is displaced to introduce the same phase shift. A piezoelectric element to stretch the fiber and its associated electronics is commercially available in a single, compact unit.[11] The device is driven with a 0- to 10-V signal, which is compatible with typical digital-to-analog converters. The total phase shift introduced with respect to the maximum applied voltage can be selected by varying the total length of the fiber cemented to the piezoelectric element.

Typical interferograms produced with both plane-wave and convergent-beam illumination are shown in Fig. 58.31. To date, a laser diode has not been purchased, although suitable candidates have been identified. Therefore, both images in Fig. 58.31 were produced with a He-Ne laser. At this time, both large-diameter capsules and the methods to produce uniform, thick condensed fuel layers in them remain to be fully developed. Hence, tests were performed on room-temperature capsules with effective focal lengths comparable to those calculated for OMEGA Upgrade–sized capsules containing thick cryogenic fuel layers. Figure 58.31(a) was obtained by removing L_2 and adjusting the half-wave plate to produce maximum fringe contrast. In Fig. 58.31(b), L_2 was replaced and its position was adjusted until the center of the target's image was nearly uniform in intensity. Note that the *f*-number of L_2 must be chosen to sufficiently overfill the target's image so that the curvature of the object wavefront passing around the capsule can be accurately determined, as described below.

The interferogram shown in Fig. 58.31(b) is analyzed in the following manner to obtain information about the thickness and uniformity of the condensed fuel layer. First the center of the target's image is located while blocking the reference beam. The reference beam is restored, and phase-shifting techniques are utilized to map the phase of the wavefront as a function of position within the image, modulo 2π. The phase of the wavefront is "unwrapped" so that continuous surfaces representing the wavefront inside and outside the target's image are obtained. The discontinuity between the wavefront transmitted through the capsule and that passing around it occurs near the circumference of the capsule, where there is a substantial step in the object wavefront's phase and there may be a dark area due to light being refracted outside the aperture of L_3.

The wavefront within the interior of the capsule is then fitted to a set of polynomials that are orthonormal over a unit circle, such as Zernike polynomials.[12,13] The center and radius of curvature of the wavefront surrounding the target's image is then determined. Although the background rings should be made concentric with the center of the target's image, the lateral displacement between the centroid of the target's circumference and the center of curvature of the wavefront surrounding the target's image determines the magnitude and direction of the residual tilt between the object and reference wavefronts. The difference in curvature of the wavefronts transmitted through and passing around the target is used to determine the thickness of the fuel layer, accounting for the contribution due to the empty capsule. The coefficients of the higher-order polynomials reveal the thickness and lateral dimensions of the nonuniformities present in the condensed fuel layer.

Although the analysis of the interferogram produced is significantly more complicated, the interferometer described above has several advantages over optical systems that illuminate the target with planar wavefronts. By illuminating the target with a beam converging to its rear focal point, the wavefront emerging from the target is flattened, with only the curvature due to the spherical aberration term remaining. More light is collected from regions near the perimeter of the target, and the interferogram consists of a set of rings that are concentrated near the perimeter of the target's image. This enhances the phase sensitivity, and therefore the sensitivity to thickness variations, that can be achieved with a specific CCD array.

In addition, this interferometer incorporates several unique features. The location of the convergent beam's focal point can be continuously adjusted to compensate for a wide range of capsule/fuel-layer dimensions. Stretching the optical fiber in the reference arm provides phase-shifting capabilities without translating optical components. The use of relatively short-coherence-length light suppresses interference from spurious reflections within the optical system, thereby reducing noise in the interferogram.

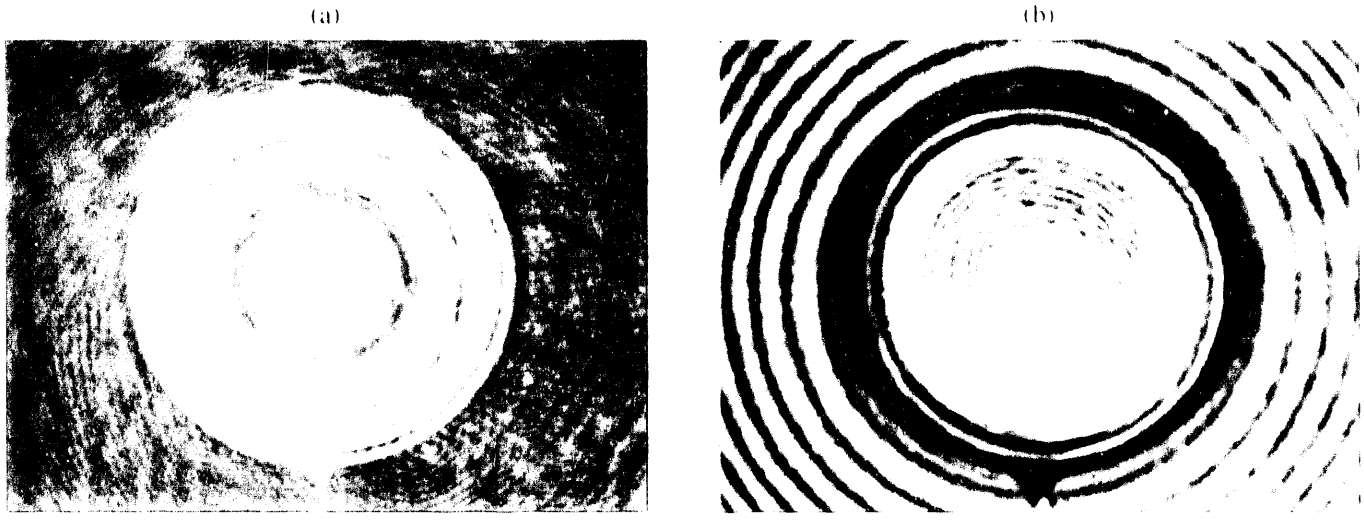

Figure 58.31
Actual interferograms of a 3.3-μm-thick glass capsule with a diameter of 270 μm. This capsule has the same focal length (~8.0 mm) as the target used to generate the interferograms in Fig. 58.24; however, $W_{0.10}$ for the capsule in these images is only ~0.55 μm instead of ~6.5 μm for the comparable cryogenic target. The capsule was illuminated by a He-Ne beam and imaged by $f/3.5$ optics. In (a), L_2 was removed and the half-wave plate adjusted to produce maximum fringe contrast. L_2 was replaced in (b) and its position was adjusted until the center of the capsule's image was nearly uniform in intensity. Note the low-contrast noise in each due to interference between the reflections from the various optical surfaces and the relatively long coherence length of the light used.

ACKNOWLEDGMENT

This work was supported by the U.S. Department of Energy Office of Inertial Confinement Fusion under Cooperative Agreement No. DE-FC03-92SF19460, the University of Rochester, and the New York State Energy Research and Development Authority. The support of DOE does not constitute an endorsement by DOE of the views expressed in this article.

REFERENCES

1. J. A. Tarvin *et al.*, in *Interferometry* (SPIE, San Diego, CA, 1979), Vol. 192, pp. 239–243.
2. T. P. Bernat, D. H. Darling, and J. J. Sanchez, J. Vac. Sci. Technol. **20**, 1362 (1982).
3. K. Kim, L. Mok, and M. J. Erlenborn, J. Vac. Sci. Technol. A **3**, 1196 (1985).
4. K. Kim and D. L. Krahn, J. Appl. Phys. **61**, 2729 (1987).
5. T. R. Pattinson and W. J. Felmlee, J. Vac. Sci. Technol. A **6**, 1882 (1988).
6. H. J. Kong, M. D. Wittman, and H. Kim, Appl. Phys. Lett. **55**, 2274 (1989).
7. Meadowlark Optics, 7460 Weld County Road 1, Longmont, CO 80504-9470.
8. K. Creath, in *Surface Characterization and Testing*, edited by K. Creath (SPIE, Bellingham, WA, 1986), Vol. 680, pp. 19–28.
9. K. Kinnstaetter, A. W. Lohmann, J. Schwider, and N. Streibl, Appl. Opt. **27**, 5082 (1988).
10. K. Creath, in *Progress in Optics XXVI*, edited by E. Wolf (Elsevier Science Publishers, 1988), pp. 349–393.
11. Canadian Instrumentation and Research Limited, 5035 North Service Road, Unit B7/8, Burlington, Ontario, Canada L7L 5V2.
12. M. Born and E. Wolf, *Principles of Optics*, 6th ed. (Pergamon, Oxford, 1980), pp. 464–468.
13. D. Malacara, ed., *Optical Shop Testing* (John Wiley & Sons, New York, 1978), pp. 489–505.

Compact, Multijoule-Output, Nd:Glass, Large-Aperture Ring Amplifier

A high-gain, large-aperture ring amplifier (LARA) has been developed with a 37-mm clear aperture that delivers output energies of >15 J in a 1-ns pulse at a wavelength of 1.053 μm. The compact ring amplifier fits entirely on a 4' × 10' table and is the main component of the OMEGA Upgrade driver line. The key elements of the ring cavity are a flash-lamp-pumped, 40-mm-diam Nd:glass amplifier rod, a telephoto lens vacuum spatial filter, and a Pockels cell that optically switches the pulse to be amplified in and out of the ring cavity.

System Optical Configuration

The standard optical configuration for the LARA amplifier is shown in Fig. 58.32. A pulse originating from a regenerative amplifier passes through an apodizer before entering LARA. The apodizer modifies the beam profile in order to produce a prescribed near-field intensity distribution after amplification. A typical apodizer and its corresponding annular beam are shown in Fig. 58.33. The apodizer pattern (Fig. 58.33) is one of carefully shaped teeth protruding into the transmission region. The radially varying teeth width determines the radially varying transmission function. Although this concept is not new,[1] the fabrication technique used is new. The apodizer is manufactured by depositing a thin, opaque layer of chrome on one side of a plane-parallel BK7 substrate. The plane-parallel substrate minimizes pointing changes when the apodizer is inserted into the beam. Using standard lithographic techniques, the apodizer is etched into the chrome layer. The teeth in the apodizer are at high spatial frequency and are removed by the spatial filter in LARA, leaving behind the low-frequency, radial intensity modulation. Different apodizers can be used to produce different beam profiles after amplification in LARA. Annular, flat-topped, and a variety of other beam profiles have been produced in this fashion. After passing through the apodizer, the pulse is switched into LARA for amplification by reflection off the input polarizer.

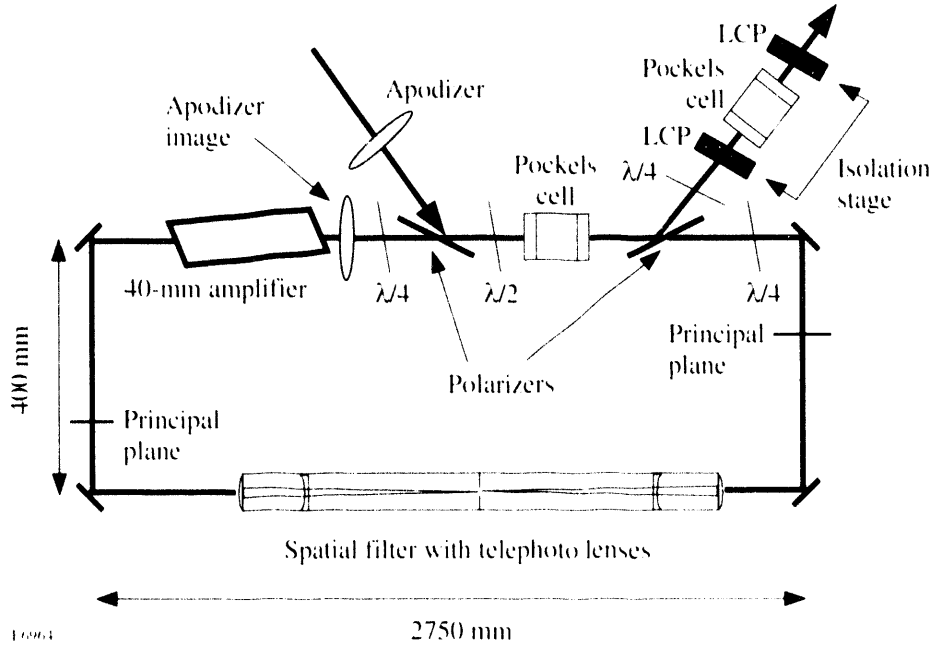

Figure 58.32
Standard LARA design with apodizer image at the output beam inside the cavity

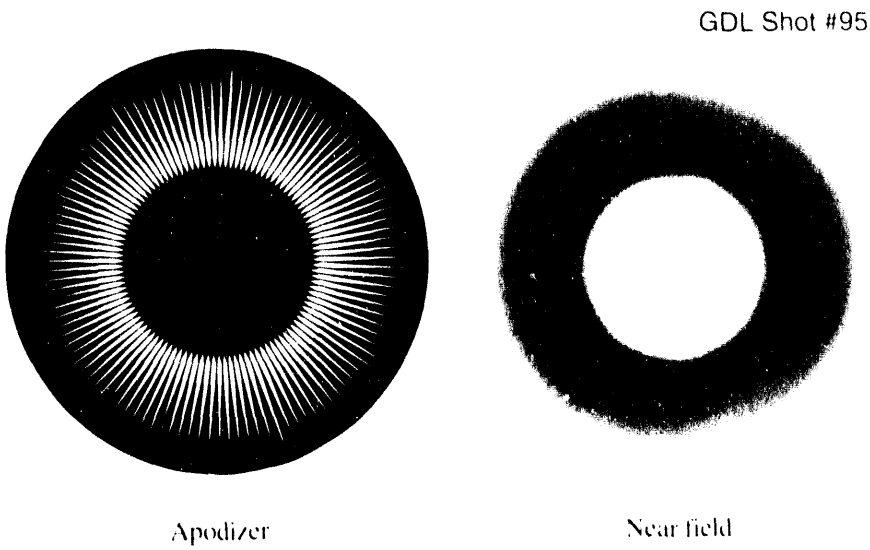

E6972

Figure 58.33
Cerated apodizer used to produce annular beam from LARA (left) with corresponding near field output from LARA (right).

The polarization of a pulse inside LARA is controlled by the combination of two polarizers: a half-wave plate and a Pockels cell as shown in Fig. 58.32. With the Pockels cell off, *s*-polarized light enters LARA by reflection off the input polarizer. The half-wave plate changes the light to *p*-polarization, which is transmitted by the output polarizer. After one round trip, the light is again changed back to *s*-polarization by the half-wave plate and is reflected out of LARA by the output polarizer. Under an ideal situation where the polarizers have infinite contrast between transmitted *p*-polarized and reflected *s*-polarized light, a pulse can travel at most one round trip before being reflected out of LARA by one of the polarizers. This design feature limits the amount of amplified spontaneous emission (ASE) that can build up inside LARA.

If more than one amplification pass is desired, the Pockels cell can be pulsed to its half-wave voltage during the first round trip of an injected pulse. When the pulse passes through the polarizer section again, it experiences a full-wave rotation from the half-wave plate and pulsed Pockels cell and is transmitted by the output polarizer. After the pulse passes the Pockels cell for a final round trip, the Pockels cell is turned off, and the pulse is subsequently reflected out of LARA off the output polarizer. In this fashion, multiple round trips in LARA can be made by turning the Pockels cell on for multiples of the round-trip cavity time (22 ns). For example, four round trips occur when the Pockels cell is turned on for 66 ns.

Polarization control is also used for purposes other than containing the pulse in the LARA cavity. The addition of two quarter-wave plates, as shown in Fig. 58.32, changes *p*-polarized light to circular polarization while passing through the amplifier rod and spatial filter. The effects of radial birefringence are mitigated by passing circularly polarized light through the amplifier rod. Also, backreflected beams from near-normal surfaces in the cavity such as the spatial filter lenses are reflected out of LARA from the polarizers because of a half-wave rotation from double passing the quarter-wave plates. This prevents damage due to ghost reflections by directing the ghost energy out of LARA before it is amplified.

A vacuum spatial filter with telephoto lenses is placed inside LARA to provide 1:1 imaging in the cavity, provide spatial beam cleanup after each amplification pass, increase the threshold for "self-lasing" of the cavity, and cancel odd-order wavefront aberrations for an even number of round trips. A typical ring cavity design with 1:1 imaging would use a two-lens relay, with one lens at each principal plane in Fig. 58.32 and focal lengths equal to one-fourth of the round trip cavity distance. At the high energies of LARA, a vacuum relay is required to eliminate breakdown at the focus of the lenses. For a 1:1 imaged cavity the principal planes must lie in opposing legs of the ring and cause difficulties in the design of a vacuum relay. Therefore a relay with telephoto lenses is placed in one leg of the ring. The effective focal length of the telephoto lenses is equal to one-fourth the cavity round-trip distance, but the principal planes are displaced from the lens positions allowing the relay to lie in one leg of the ring.

Spatial amplitude noise from each amplification pass is filtered by placing a pinhole at the focus of the vacuum relay. The pinhole also reduces ASE in LARA by limiting the range

of pointing angles that can propagate inside LARA. Since the spatial filter causes an image inversion when traversed, odd-order aberrations in LARA, such as coma, will be eliminated provided an even number of round trips are made.

After amplification, the pulse is switched out of LARA by reflection off the output polarizer and passes through a quarter-wave plate and an isolation stage. The isolation stage consists of two liquid crystal polarizers (LCP) of opposite handedness surrounding a Pockels cell. The isolation stage is used to improve the contrast between the amplified pulse out of LARA and any pre- or post-pulses. The isolation stage also protects LARA from light propagating back through the isolation stage.

One of the drawbacks of the present LARA design (Fig. 58.32) is the 1:1 imaging of the cavity that places the image of the input apodizer inside LARA. At times, space constraints do not allow for proper image relaying of the apodizer through the output of LARA. An alternative LARA design that overcomes this difficulty is shown in Fig. 58.34. Here, the image of the apodizer in the output beam falls outside the LARA cavity, which simplifies image relay into the rest of the amplifier chain.

System Characterization

Several features of the LARA amplifier are investigated: holdoff, gain versus bank energy, near field, interferometry, and prepulse contrast. Unless otherwise stated, the results presented are for a four-pass LARA in the configuration shown in Fig. 58.32. Since the amplifying medium in the LARA cavity is a flash-lamp-pumped, 40-mm-diam Nd:glass amplifier rod, a maximum repetition rate of one shot per 5 min is used for system characterization.

The holdoff voltage of the ring amplifier cavity is defined as the voltage to which the amplifier can be fired before self-lasing of the ring occurs. Self-lasing of the ring occurs when the round trip gain for ASE exceeds the round-trip losses with the Pockels cell in the "off" state. Below the self-lasing threshold, any ASE traveling around the ring can accumulate only over one round trip before being reflected from the cavity. The self-lasing threshold is primarily determined by the practical limitations set by the finite contrast of the polarizers and the Pockels cell, as well as nonideal wave plates, the size of the spatial filter pinhole, and the birefringence of optical components between the input and output polarizers. Since there are more optical components between the polarizers in the cavity configuration in Fig. 58.34, a lower self-lasing

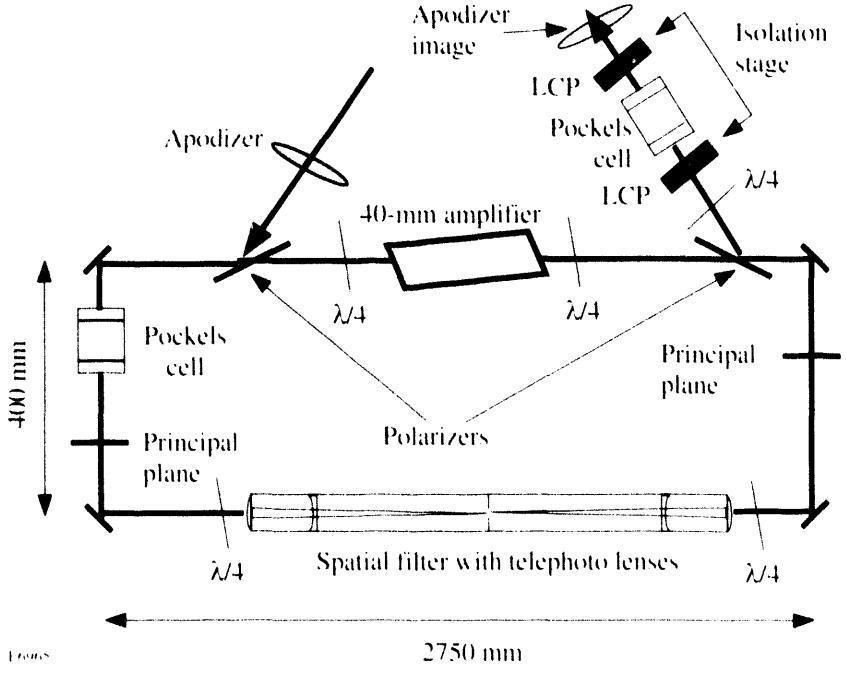

Figure 58.34
Alternative LARA design with apodizer image of the output beam outside the cavity

threshold or holdoff voltage is both expected and observed. Holdoff voltages as high as 6.4 kV, with a corresponding single-pass, small-signal gain of $G_{ss} \sim 19$, have been measured for the cavity in Fig. 58.32, while holdoff voltages for Fig. 58.34 are around 6.0 kV ($G_{ss} \sim 16$). Since the gain bandwidth of Nd:glass[2] is ~200 Å, the optical elements of the LARA cavity must not provide only for high contrast at the 1.053-μm amplification wavelength, but also for wavelengths to either side. Thus, we observed a higher self-lasing threshold for zero-order wave plates than for multiple-order wave plates. It should also be kept in mind that incorrectly set wave plates in the cavity can result in catastrophic self-lasing with resulting damage to optical components.

The onset of self-lasing is easily diagnosed with the fluorescence traces from the amplifier rod. Figure 58.35 shows photodiode-recorded fluorescence traces of a LARA under normal operating and under self-lasing conditions without pulse injection. Self-lasing manifests itself in the familiar spikes superimposed on a usually smooth fluorescence trace. More dramatic self-lasing can be detected by placing burn paper outside of LARA facing the input and output polarizers.

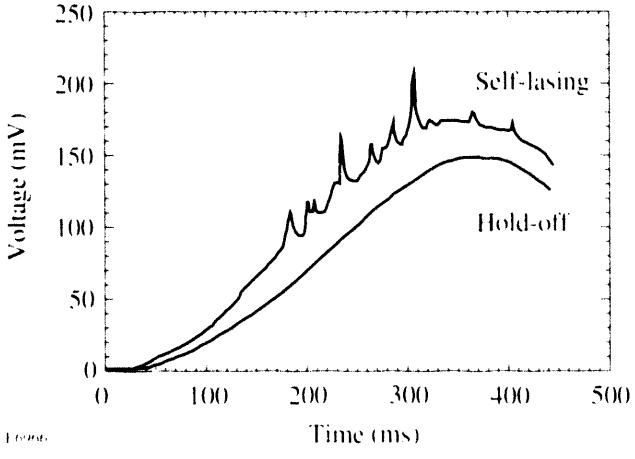

Figure 58.35
The fluorescence traces from a LARA amplifier exhibiting self-lasing (top trace) and under normal hold-off conditions (bottom trace).

The total small-signal gain of the LARA system as a function of flash-lamp bank energy for three and four round trips is shown in Fig. 58.36. With four round trips, total gains of $\geq 10^5$ have been achieved at bank energies of 6 kV without noticeable degradation in beam quality. Figure 58.37 shows the output beam profile for a full-aperture, 13.7-J LARA shot with 140-μJ input energy. The azimuthally averaged lineout shows the 37-mm beam diameter with an intensity distribution

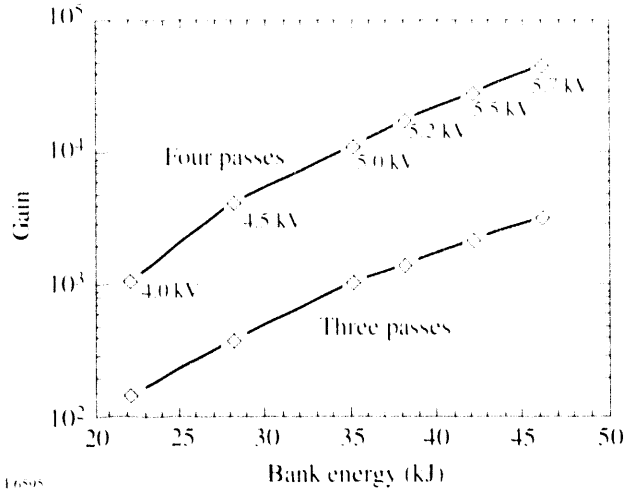

Figure 58.36
Total gain of LARA as a function of flash-lamp bank energy for three- and four-pass configurations.

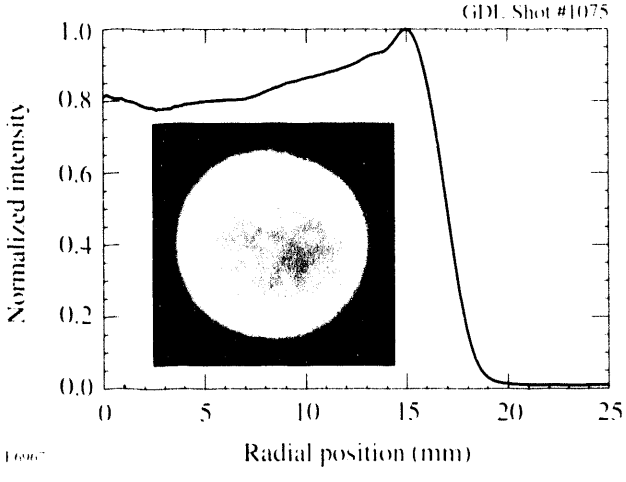

Figure 58.37
Near field of 13.7-J shot from LARA with azimuthally averaged lineout.

peaked at the edges of the beam due to the radial gain in the 40-mm amplifier rod. The peaked edges were expected because the apodizer used with this test was not designed to produce a flattop beam at total small-signal gains of $\geq 10^5$. An appropriately designed apodizer can easily produce a flattop profile at this energy.

The wavefront quality of LARA at full aperture and high energy has been investigated with a self-referencing Mach-Zehnder interferometer.[3] Figure 58.38 shows a reduced interferogram of the LARA output at 17.8 J. The background phase error of the interferometer error is removed from the

measurement using a separately recorded wavefront of the input beam without passing through LARA. The peak-to-valley wavefront distortion of an amplified full-aperture beam after four round trips is approximately 1 wave (see Fig. 58.37). Half of this wavefront distortion is directly attributable to the LARA Pockels cell. In the OMEGA Upgrade driver-line application, the aperture diameter is 20 mm and the corresponding peak-to-valley wavefront distortion is a very satisfactory ~0.25 waves.

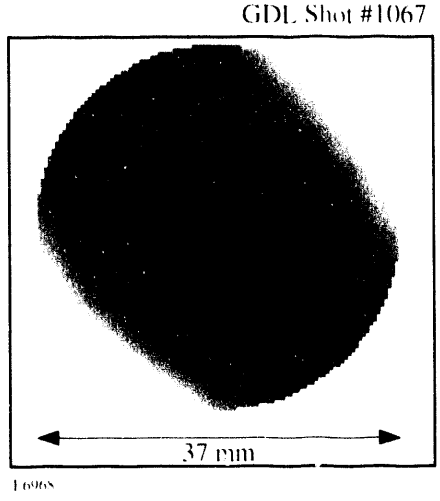

Figure 58.38
Interferogram of 17.8-J shot from LARA (interferometer error subtracted); peak-to-valley wavefront error = 0.970±0.138 waves, rms error = 0.255±0.307 waves.

One interesting characteristic of LARA is its 'first-shot syndrome,' which manifests itself as a degradation of wavefront quality for the first shot of the day. Figure 58.39 shows the peak-to-valley wavefront error over a 37-mm aperture obtained for a series of shots on a typical day. The peak-to-valley wavefront quality of the first shot of the day with a "cold" amplifier rod is shown by the circle in Fig. 58.39. The series of data points below this circle shows a reduced peak-to-valley distortion for all subsequent shots taken at various intervals between 7 and 20 min. There is a ≥0.5-wave peak-to-valley reduction from the first shot of the day to all subsequent shots. The 'first-shot syndrome' is not well understood, but similar observations have been made previously on the 24-beam OMEGA system. As a practical precaution, the first shot of the day for LARA will not be allowed to propagate down the main amplifier chains of the OMEGA Upgrade.

For the OMEGA Upgrade, the required prepulse energy contrast on target is $>10^9$, which translates to a prepulse contrast for LARA of $>10^4$. Prepulses on the LARA output are due to leakage of a small percentage of the circulating pulse within LARA during each round trip. Without firing the LARA amplifier, the measured prepulse contrast is $\sim 4 \times 10^5$. Under amplified conditions the prepulse contrast is enhanced (multiplied) by the single-pass small-signal gain of the LARA amplifier (typically $G_{ss} \approx 10$) since the prepulse is due to the circulating main pulse during the next-to-last round trip inside LARA. Thus, the LARA prepulse contrast is $\geq 4 \times 10^4$, which is well within the OMEGA Upgrade requirements.

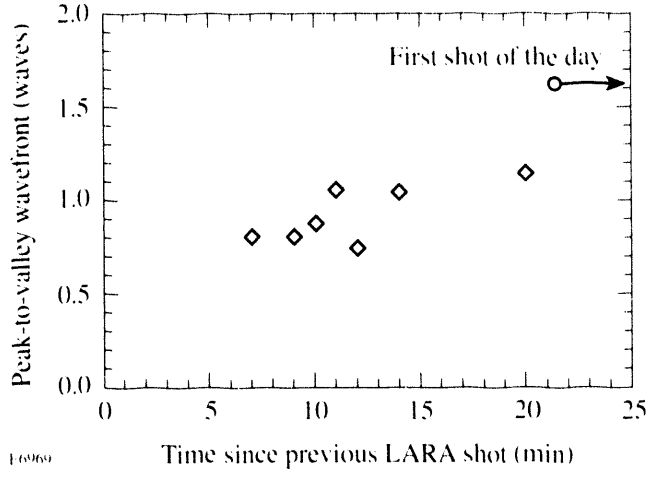

Figure 58.39
The peak-to-valley wavefront quality of LARA output at full aperture for the first shot of the day (circle) and subsequent cycled shots (diamonds).

Conclusions

A high-gain, large-aperture ring amplifier (LARA) has been developed with a 37-mm clear aperture that delivers output energies of >15 J in a 1-ns pulse at a wavelength of 1.053 μm. The compact ring amplifier fits entirely on a 4′ × 10′ table and is the main component of the OMEGA Upgrade driver. The key elements of the ring cavity are a flash-lamp-pumped, 40-mm Nd:glass amplifier rod, a telephoto lens vacuum spatial filter, and a Pockels cell that injects the input pulse and ejects the output pulse from the ring cavity. LARA produces a high-energy output beam with excellent wave-front quality and near-field beam profile. LARA output beam profiles can be tailored by an input apodizer. At full aperture (37 mm), a four-pass LARA introduces ~1-wave peak-to-valley distortion on the wavefront quality of the beam. At the 20-mm aperture used by the OMEGA Upgrade, the peak-to-valley distortion is only ~0.25 waves. Excluding the first LARA shot of each day, a consistent wavefront quality is maintained for all shots. The prepulse contrast of LARA output is typically $>10^4$, which meets the OMEGA Upgrade specifications.

ACKNOWLEDGMENT

We would like to acknowledge the invaluable contributions of many LLE co-workers: D. Bancroft, W. Beich, D. Brown, C. Cotton, J. H. Kelly, C. K. Merle, R. G. Roides, W. Seka, M. D. Skeldon, M. Tedrow, K. Thorp, M. D. Tracy, and I. Will. Their efforts are greatly appreciated. This work was supported by the U.S. Department of Energy Office of Inertial Confinement Fusion under Cooperative Agreement No. DE-FC03-92SF19460, the University of Rochester, and the New York State Energy Research and Development Authority. The support of DOE does not constitute an endorsement by DOE of the views expressed in this article.

REFERENCES

1. J. Auerbach and J. Lawson, Lawrence Livermore National Laboratory (private communication).

2. S. E. Stokowski, R. A. Saroyan, and M. J. Weber, Lawrence Livermore National Laboratory Report, M-95, Rev. 2, Vol. I (1981).

3. Laboratory for Laser Energetics LLE Review **31**, NTIS document No. DOE/DP/40200-47, 1987 (unpublished), p. 114.

PUBLICATIONS AND CONFERENCE PRESENTATIONS

Publications

X. D. Cao and D. D. Meyerhofer, "Soliton Collisions in Optical Birefringent Fibers," J. Opt. Soc. Am. B **11**, 380 (1994.)

H. E. Elsayed-Ali, J. W. Herman, and E. A. Murphy, "Ultrafast Laser Superheating of Metal Surfaces," in *Beam Solid Interactions: Fundamentals and Applications*, edited by M. Natasi *et al.* (Materials Research Society, Pittsburgh, PA, 1993), Vol. 279, pp. 685–690.

H. E. Elsayed-Ali and T. Juhasz, "Femtosecond Time-Resolved Thermomodulation of Thin Gold Films with Different Crystal Structures," Phys. Rev. B **47**, 13599 (1993).

E. M. Epperlein, "Effect of Electron Collisions on Ion-Acoustic Waves and Heat Flow," Phys. Plasmas **1**, 109 (1994).

E. M. Epperlein, R. W. Short, and A. Simon, "Transport and Sound Waves in Plasmas with Light and Heavy Ions," Phys. Rev. E **49**, 2480 (1994).

S. D. Jacobs, "Progress at the Center for Optics Manufacturing," in *Optical Fabrication, Testing, and Surface Evaluation*, edited by J. Tsujiuchi (SPIE, Bellingham, WA, 1992), Vol. 1720, pp. 169–174.

H. Kim and M. D. Wittman, "Interferometric Microscopy—An Overview of the Optical Characterization of Inertial-Fusion Targets," in *Multidimensional Microscopy*, edited by P. C. Cheng, T. H. Lin, W. L. Wu, and J. L. Wu (Springer-Verlag, New York, 1994), pp. 103–121.

W. Kula and R. Sobolewski, "Charging Effect in Partially Oxygen-Depleted, Superconducting Y-Ba-Cu-O Thin Films," Phys. Rev. B **49**, 6428 (1994).

W. N. Maung, D. P. Butler, W. Xiong, W. Kula, and R. Sobolewski, "Microwave Properties of Monolithic Y-Ba-Cu-O Transmission Line Devices Fabricated by the Laser-Writing Patterning Technique," in *High-T_c Microwave Superconductors and Applications* (SPIE, Bellingham, WA, 1994), Vol. 2156, pp. 174–180.

R. L. McCrory, "Direct-Drive Implosion Experiments for Laser Fusion on OMEGA and the OMEGA Upgrade," in *Proceedings of the 21st ECLIM*, edited by H. Fiedorowicz, J. Wolowski, M. Mroczkowski, M. Szczurek, and A. Ulinowicz (ECLIM, Warsaw, Poland, 1992), pp. 197–200.

D. D. Meyerhofer and J. Peatross, "Angular Distributions of High-Order Harmonics," in *Super-Intense Laser-Atom Physics*, edited by B. Piraux, A. L'Huillier, and K. Rzazewski, NATO ASI Series B, Physics, Vol. 316 (Plenum Press, New York, 1993), pp. 19–29.

J. Peatross and D. D. Meyerhofer, "Measurement of the Angular Distribution of High-Order Harmonics Emitted from Rare Gases," in *OSA Proceedings on Shortwavelength V: Physics with Intense Laser Pulses*, edited by P. B. Corkum and M. D. Perry (Optical Society of America, Washington, DC, 1993), Vol. 17, pp. 122–126.

L. Shi, T. Gong, X. Xiong, X. Weng, Y. Kostoulas, R. Sobolewski, and P. M. Fauchet, "Femtosecond Reflectivity of 60-K Y-Ba-Cu-O Thin Films," Appl. Phys. Lett. **64**, 1150 (1994).

S. Skupsky and T. J. Kessler, "Speckle-Free Phase Plate (Diffuser) for Far-Field Applications," J. Appl. Phys. 74, 4310 (1993).

R. Sobolewski, W. Xiong, W. Kula, and J. R. Gavaler, "Laser Patterning of Y-Ba-Cu-O Thin-Film Devices and Circuits," Appl. Phys. Lett. **64**, 643 (1994).

B. Soom, H. Chen, Y. Fisher, and D. D. Meyerhofer, "Strong K_α Emission in Picosecond Laser-Plasma Interactions," in

OSA's Proceedings on Shortwavelength V: Physics with Intense Laser Pulses, edited by P. B. Corkum and M. D. Perry (Optical Society of America, Washington, DC, 1993), Vol. 17, pp. 192–195.

J. M. Soures, "High-Technology Advances from LLE Research," Rochester Business Profiles Journal, August 1991, 40–41.

J. M. Soures, "Solid State Lasers for ICF," in *Nuclear Fusion by Inertial Confinement*, edited by G. Velarde, Y. Ronen, and J. M. Martinez-Val (CRC Press, 1993), Chap. 14, pp. 351–370.

J. M. Soures, "The OMEGA Upgrade Laser Facility for Direct-Drive Experiments," J. Fusion Energy **10**, 295 (1991).

J. Sweetser, T. J. Dunn, I. A. Walmsley, C. Radzewicz, S. Palese, and R. J. D.Miller, "Characterization of an FM Mode-Locked Nd:YLF Laser Synchronized with a Passively Mode-Locked Dye Laser," Opt. Commun. **97**, 379 (1993).

C. J. Twomey, S.-H. Chen, T. Blanton, A. W. Schmid, and K. L. Marshall, "Solid Polymers Doped with Rare Earth Metal Compounds. III. Formation and Stability of Macromolecular Complexes Comprising Neodymium Nitrate and Dipivaloylmethane in Poly(Ethylene Oxide)," J. Polym. Sci. B, Polym. Phys. **32**, 551 (1994).

Forthcoming Publications

S. Alexandrou, C.-C. Wang, R. Sobolewski, and T. Y. Hsiang, "Generation of Subpicosecond Electrical Pulses by Nonuniform Illumination of GaAs Transmission Line Gaps," to be published in the *IEEE Journal of Quantum Electronics*.

S. Alexandrou, C.-C. Wang, M. Currie, R. Sobolewski, and T. Y. Hsiang, "Loss and Dispersion at Subterahertz Frequencies in Coplanar Waveguides and Varying Ground-Plane Widths," to be published in *SPIE Vol. 2149: Technologies for Optical Fiber Communications*.

R. Betti, V. Goncharov, R. L. McCrory, E. Turano, and C. P. Verdon, "Multiple Cutoff Wave Numbers of the Ablative Rayleigh-Taylor Instability," to be published in *Physical Review Letters*.

X. D. Cao, G. P. Agrawal, and C. J. McKinstrie, "Self-Focusing of Chirped Optical Pulses in Nonlinear Dispersive Media," to be published in *Physical Review A*.

X. D. Cao and D. D. Meyerhofer, "Nonlinear Birefringence of Optical Fibers," to be published in *Optics Communications*.

M. J. Cumbo and S. D. Jacobs, "Determination of Near-Surface Forces in Optical Polishing Using Atomic Force Microscopy," to be published in *Nanotechnology*.

J. A. Delettrez, D. K. Bradley, and C. P. Verdon, "The Role of the Rayleigh-Taylor Instability in Laser-Driven Burnthrough Experiments," to be published in *Physics of Fluids B*.

W. R. Donaldson and L. Mu, "Effect of Illumination Uniformity on GaAs Photoconductive Switches," to be published in the *IEEE Journal of Quantum Electronics*.

E. M. Epperlein, "Fokker-Planck Modeling of Electron Transport in Laser-Produced Plasmas," to be published in *Laser & Particle Beams*.

E. M. Epperlein, "Implicit and Conservative Difference Scheme for the Fokker-Planck Equation," to be published in the *Journal of Computational Physics*.

E. M. Epperlein and R. W. Short, "Comments on 'Theory and Three-Dimensional Simulation of Light Filamentation in Laser-Produced Plasmas' [Phys. Fluids B 5, 2243 (1993)]," to be published in *Physics of Fluids B*.

E. M. Epperlein and R. W. Short, "Generalized Electron Fluid Equations in the Presence of Laser Irradiation," to be published in *Physics of Plasmas*.

E. M. Epperlein and R. W. Short, "Nonlocal Electron Transport in the Presence of High-Intensity Laser Irradiation," to be published in *Physical Review E*.

D. Fried, R. E. Glena, J. D. B. Featherstone, and W. Seka, "The Nature of Light Scattering in Dental Enamel and Dentin at Visible and Near Infrared Wavelengths," to be published in *Applied Optics*.

T. Gong, J. F. Young, G. W. Wicks, P. J. Kelly, and P. M. Fauchet, "Hot-Carrier Dynamics Near the Fermi Edge of N-Doped GaAs," to be published in *Semiconductor Science and Technology*.

T. Gong and P. M. Fauchet, "Carrier-Carrier Interactions in GaAs Investigated by Femtosecond Spectroscopy," to be published in the *Proceedings of SPIE's OE/LASE '93*, Los Angeles, CA, 16–23 January 1993 (invited).

D. Gupta, W. R. Donaldson, and A. M. Kadin, "Fast Inductively Coupled Superconducting Opening Switch Triggered by Short Laser Pulses," to be published in the *Proceedings of the 9th International Pulsed Power Conference*, Albuquerque, NM, 21–23 June 1993.

D. Gupta, W. R. Donaldson, and A. M. Kadin, "A Laser-Triggered, Inductive Opening Switch Using High-Temperature Superconducting Thin Films," to be published in *Advances in Cryogenic Engineering*.

D. Gupta, "A New Optically Triggered Superconducting Opening Switch for High-Power Applications," to be published in *Research Reports of the Link Energy Fellows*.

J. W. Herman, H. E. Elsayed-Ali, and E. A. Murphy, "Time-Resolved Structural Studies of the Low-Index Faces of Lead," to be published in *Physical Review B*.

S. D. Jacobs, K. L. Marshall, and A. Schmid, "Liquid Crystals for Laser Applications," to be published in the *CRC Handbook of Laser Science and Technology, Supplement 2: Optical Materials*.

A. M. Kadin, D. Gupta, D. D. Mallory, M. Takahashi, W. R. Donaldson, and J. K. Truman, "Fabrication, Properties, and Applications of In-Situ Sputtered YBCO Films," to be published in the *Proceedings of the 6th Annual Conference on Superconductivity and Applications*, Buffalo, NY, 15–17 September 1992.

H. Kim, J. M. Soures, and P.-C. Cheng, "Confocal Microscopic Characterization of Laser-Fusion Target," to be published in the *Proceedings of the 39th AVS National Symposium and Topical Conferences*, Chicago, IL, 9–13 November 1992.

E. M. Korenic, S. D. Jacobs, J. K. Houghton, F. Kreuzer, and A. Schmid, "Nematic Polymer Liquid-Crystal Waveplate for High-Power Lasers at 1054 nm," to be published in *Applied Optics*.

E. M. Korenic, K. L. Marshall, and J. A. Maiolo, "Blending Polysiloxane 'Glass Resins' to Produce Optical Films with a Specific Refractive Index," to be published in *Optics and Photonics News*.

Y. Kostoulas, P. M. Fauchet, T. Gong, B. C. Tousley, G. W. Wicks, and P. Cooke, "Femtosecond Carrier Dynamics in Low-Temperature-Grown III - V Semiconductors," to be published in the *Proceedings of SPIE's OE/LASE '94*, Los Angeles, CA, 22–28 January 1994.

Y. Kostoulas, T. Gong, A. I. Lobad, and P. M. Fauchet, "Investigation of Carrier-Carrier Scattering by Three-Pulse Probe Spectroscopy," to be published in *Semiconductor Science and Technology*.

Y. Kostoulas, T. Gong, G. W. Wicks, and P. M. Fauchet, "Femtosecond Carrier Dynamics in Low-Temperature-Grown InP," to be published in *Applied Physics Letters*.

W. Kula and R. Sobolewski, "Electric-Field-Effect Devices Based on Partially Oxygen-Depleted, Superconducting Y-Ba-Cu-O Thin Films," to be published in *Advances in Cryogenic Engineering*, Volume 40.

W. Kula and R. Sobolewski, "Electric-Field Effect in Partially Deoxygenated YBCO Thin Films," to be published in *Physica B*.

B. S. W. Kuo and A. W. Schmid, "Effects of Thin-Film Thermal Conductivity on the Optical Damage Threshold of a-Si Film on c-Si Substrate at 1064 nm," to be published in the *Journal of Applied Physics*.

Y. Lin and T. J. Kessler, "Raman Scattering: A Four-Dimensional System," to be published in *Applied Optics*.

A. I. Lobad, S. M. Mehta, B. C. Tousley, P. J. Rodney, and P. M. Fauchet, "The Starting Mechanism in Coupled-Cavity Mode-Locked Laser Systems," to be published in the *IEEE Journal of Quantum Electronics*.

A. I. Lobad, P. J. Rodney, B. C. Tousley, S. M. Mehta, and P. M. Fauchet, "The Starting Mechanism in Coupled-Cavity,

Mode-Locked Laser Systems," to be published in the *Proceedings of SPIE's OE/LASE '94*, Los Angeles, CA, 22–29 January 1994.

R. S. Marjoribanks, F. W. Budnik, H. Chen, and D. D. Meyerhofer, "Plasma Electron Temperature in Picosecond Laser Plasmas from Quasi-Steady Ratio of Isoelectronic Lines," to be published in *Physical Review Letters*.

F. J. Marshall, J. A. Delettrez, R. Epstein, and B. Yaakobi, "Diagnosis of Laser-Target Implosions by Space-Resolved Continuum Absorption X-Ray Spectroscopy," to be published in *Physical Review E*.

R. L. McCrory, "Progress Toward Ignition with Direct Drive," to be published in *Concerning Major Systems in Science and Technology*.

L. Mu and W. R. Donaldson, "Simulating Photoconductive Switches in a Microwave Transmission Line," to be published in the *Proceedings of the 9th IEEE International Pulsed Power Conference*, Albuquerque, NM, 21–23 June 1993.

S. Papernov and A. W. Schmid, "Atomic Force Microscopy Studies of Laser-Triggered Morphology Changes in Y_2O_3 Monolayer Coatings," to be published in *SPIE's Proceedings of the Annual Symposium on Optical Materials for High Power Lasers*.

S. Papernov and A. W. Schmid, "Atomic Force Microscopy Observations of Water-Induced Morphological Changes in Y_2O_3 Monolayer Coatings," to be published in *SPIE's Proceedings of the Annual Symposium on Optical Materials for High Power Lasers*.

J. Peatross, J. L. Chaloupka, and D. D. Meyerhofer, "High-Order Harmonic Generation with an Annular Laser Beam," to be published in *Optics Letters*.

J. Z. Roach, A. Ninkov, S. W. Swales, and T. Morris, "Design and Evaluation of a Screen CCD Imaging System," to be published in *Optical Engineering*.

J. K. Samarabandu, R. Acharya, C. D. Edirisinghe, P. C. Cheng, H. Kim, T. H. Lin, R. G. Summers, and C. E. Musial, "Analysis of Multi-Dimensional Confocal Images," to be published in the *Proceedings of the SPIE Symposium "Biomedical Imaging,"* San Diego, CA, 24 February 1991.

A. W. Schmid, K. L. Marshall, and S. D. Jacobs, "Comment to 'Ultraviolet Filters Using Liquid Crystal Molecules' [J. Appl. Phys. 74, 4867 (1993)]," to be published in the *Journal of Applied Physics*.

H. Shi and S. H. Chen, "Novel Glassy Nematic and Chiral Nematic Oligomers Derived from 1,3,5-Cyclohexanetricarboxylic and (1R,3S)-(+)-Camphoric Acids," to be published in *Liquid Crystals*.

R. Sobolewski, W. Xiong, W. Kula, and B. McIntyre, "Electrical and Structural Properties of the YBCO Superconducting-Semiconducting Interface," to be published in *Physica B*.

R. Sobolewski, L. Shi, W. Xiong, X. Weng, Y. Kostoulas, and P. M. Fauchet, "Femtosecond Optical Response of Y-Ba-Cu-O Films and Their Applications in Optoelectronics," to be published in the *Proceedings of SPIE's OE/LASE '94* (invited).

C. J. Twomey, S.-H. Chen, T. Blanton, A. W. Schmid, and K. L. Marshall, "Solid Polymers Doped with Rare Earth Metal Salts. II. Thermal Behavior and Morphology of the Neodymium Acetate-Poly(Ethylene Oxide) System," to be published in the *Journal of Polymer Science, Polymer Physics Edition*.

C. J. Twomey, S.-H. Chen, T. N. Blanton, A. W. Schmid, and K. L. Marshall, "Stoichiometry and Morphology in Terbium Nitrate-Poly(Ethylene Oxide) Macromolecular Complex," to be published in the *Journal of Polymer Science, Polymer Physics Edition*.

C. J. Twomey, S.-H. Chen, T. N. Blanton, A. W. Schmid, and K. L. Marshall, "Poly[(Methylene Oxide)Oligo(Ethylene Oxide)]vs Poly(Ethylene Oxide) as Hosts for Neodymium Compounds," to be published in the *Journal of Polymer Science, Polymer Physics Edition*.

C.-C. Wang, S. Alexandrou, D. Jacobs-Perkins, and T.Y. Hsiang, "Comparison of the Picosecond Characteristics of Silicon and Silicon-on-Sapphire Metal-Semiconductor-Metal Photodiodes," to be published in *Applied Physics Letters*.

C.-C. Wang, M. Currie, S. Alexandrou, and T. Y. Hsiang, "Ultrafast, All-Silicon Light Modulator," to be published in *Optics Letters*.

C.-C. Wang, S. Alexandrou, D. Jacobs-Perkins, and T. Y. Hsiang, "Picosecond Characteristics of Silicon-on-Insulator Metal-Semiconductor-Metal Photodiodes," to be published in *SPIE's Proceedings of the Conference on Technologies for Optical Fiber Communications/High-Speed Optical Detectors*.

M. D. Wittman, R. Q. Gram, H. Kim, C. K. Immesoete, S. G. Noyes, and S. Scarantino, "Increased Retention Time for Hydrogen and Other Gases by Polymer Shells Using Optically Transparent Aluminum Layers," to be published in the *Journal of Vacuum Science and Technology*.

W. Xiong, W. Kula, and R. Sobolewski, "Fabrication of High-T_c Superconducting Electronic Devices Using the Laser-Writing Patterning Technique," to be published in *Advances in Cryogenic Engineering*.

W. Xiong, W. Kula, R. Sobolewski, W. N. Maung, and D. P. Butler, "Monolithic Y-Ba-Cu-O Electronic Devices Fabricated Using the Laser-Writing Patterning Technique," to be published in *Superconductor Science and Technology*.

W. Xiong, W. Kula, R. Sobolewski, and J. R. Gavaler, "Laser Writing: A New Technique for Fabrication of Electronic and Optoelectronic Y-Ba-Cu-O Devices and Circuits," to be published in *SPIE Vol. 2160: Superconductive Devices and Circuits*.

B. Yaakobi, Q. Su, and F. J. Marshall, "Monochromatic Backlighting in Laser-Fusion Experiments," to be published in the *Journal of X-Ray Science Technology*.

B. Yaakobi, F. J. Marshall, R. Epstein, and Q. Su, "New Diagnostic Features in the Laser Implosions of Argon-Filled Targets," to be published in *Optics Communications*.

X. Zhou, S. Alexandrou, and T. Y. Hsiang, "Monte Carlo Investigation of the Mechanism of Subpicosecond Pulse Generation by Nonuniform Gap Illumination," to be published in *Applied Physics Letters*.

Conference Presentations

W. Kula and R. Sobolewski "Electric-Field Effect in Partially Oxygen-Depleted, Superconducting Y-Ba-Cu-O Thin Films," 1994 Gordon Research Conference on Superconductivity, Oxnard, CA, 2–7 January 1994.

The following presentations were made at SPIE's OE/LASE '94, Los Angeles, CA, 22–28 January 1994:

S. Alexandrou, C.-C. Wang, M. Currie, R. Sobolewski, and T. Y. Hsiang, "Loss and Dispersion at Subterahertz Frequencies in Coplanar Waveguides and Varying Ground-Plane Widths."

D. P. Butler, W. N. Maung, W. Xiong, W. Kula, and R. Sobolewski, "Microwave Properties of Monolithic Y-Ba-Cu-O Transmission Line Devices Fabricated by the Laser-Writing Patterning Technique."

D. Fried, S. F. Borzillary, S. M. McCormack, R. E. Glena, J. D. B. Featherstone, and W. Seka, "The Thermal Effects on CO_2 Laser-Irradiated Dental Enamel at 9.3, 9.6, 10.3, and 10.6 mm."

Y. Kostoulas, P. M. Fauchet, T. Gong, B. C. Tousley, G. W. Wicks, and P. Cooke, "Femtosecond Carrier Dynamics in Low-Temperature-Grown III–V Semiconductors."

A. I. Lobad, P. J. Rodney, B. C. Tousley, S. M. Mehta, and P. M. Fauchet, "The Starting Mechanism in Coupled-Cavity, Mode-Locked Laser Systems."

R. Sobolewski, L. Shi, W. Xiong, X. Weng, Y. Kostoulas, and P. M. Fauchet, "Femtosecond Optical Response of Y-Ba-Cu-O Films and Their Applications in Optoelectronics."

C.-C. Wang, S. Alexandrou, D. Jacobs-Perkins, and T. Y. Hsiang, "Picosecond Characteristics of Silicon-on-Insulator Metal-Semiconductor-Metal Photodiodes."

W. Xiong, W. Kula, R. Sobolewski, and J. R. Gavaler, "Laser Writing: A New Technique for Fabrication of Electronic and Optoelectronic Y-Ba-Cu-O Devices and Circuits."

W. R. Donaldson, D. Gupta, and A. M. Kadin "High-Temperature, Superconducting Switches for SMES Applications," The Advisory Group on Electron Devices 1994 High-Voltage Workshop, Smyrna, GA, 1–3 March 1994.

DATE
FILMED
8/9/94

END